

Multiwavelength Studies of TeV Blazars

Thesis submitted for the Degree of

Doctor of Philosophy

in

PHYSICS

to

Deen Dayal Upadhyaya Gorakhpur University, Gorakhpur



by

Ashwani Pandey

**Aryabhatta Research Institute of Observational
Sciences (ARIES)**

Manora Peak, Nainital–263001, India

April 2019

CERTIFICATE FROM THE SUPERVISOR

This is to certify that

1. The title of the thesis “**Multiwavelength Studies of TeV Blazars**” for the award of the degree of Doctor of Philosophy was approved by the Vice-Chancellor, D.D.U. Gorakhpur University, Gorakhpur -273 009, vide office order No. F.Sc. 9145 Dept. D/S Dated 08/07/2016.
2. This thesis embodies the work of Mr. Ashwani Pandey himself.
3. Mr. Ashwani Pandey worked under our supervision on this thesis for not less than twenty four months commencing from the date of his registration in D.D.U. Gorakhpur University, Gorakhpur- 273 009 as a candidate for the Ph.D. Degree.
4. This thesis has not been submitted for the award of any degree, diploma, associateship or fellowship of any university or institute.

Dr. Alok Chandra Gupta
(Supervisor)

Prof. Sugriva Nath Tiwari
(Co-supervisor)

Place: Nainital
Date:

Place: Gorakhpur
Date:

**Deen Dayal Upadhyaya Gorakhpur University
Gorakhpur–273009 (U.P.) India**



CERTIFICATE

This is to certify that **Mr. Ashwani Pandey** (Registration No. **F.Sc. No. 9145 dated 08/07/2016**), research scholar of Department of Physics, Deen Dayal Upadhyaya Gorakhpur University pursued and successfully completed the Research Methodology and Computer Application course as per requirement of the Ph.D. ordinances and UGC Regulations—2009.

(Head)

(Supervisor)

(Co-supervisor)

DECLARATION

I hereby declare that the work presented in this thesis is a result of the investigation carried out by me at Aryabhatta Research Institute of Observational Sciences (ARIES), under the supervision of **Dr. Alok Chandra Gupta**, ARIES, Nainital (**Supervisor**) and **Prof. Sugriva Nath Tiwari**, Department of Physics, DDU Gorakhpur University (**Co-supervisor**). This work (in part or in full) has not been submitted for the award of any degree, diploma, associateship or fellowship of any university or institute.

Place : Nainital

Date : (Ashwani Pandey)

*Dedicated to
my brother ...*

Acknowledgements

I would like to thank all who motivated me and helped me in the completion of my Ph.D. thesis work.

First and foremost, I would like to express my sincere gratitude to my supervisor Dr. Alok C. Gupta for his guidance, motivation, patience and continuous support throughout my research work.

I would like to thank my co-supervisor Prof. Sugriva Nath Tiwari for his guidance and support in my Ph.D. thesis. I am profoundly grateful to our research collaborator Prof. Paul J. Wiita for his invaluable suggestions and comments.

I would like to thank ARIES for providing me the hostel, library, workplace and observing facilities. I would like to acknowledge all the Scientists in ARIES for their helpful suggestions. I am grateful to Dr. Jeewan C. Pandey who helped me whenever I approached him with my doubts. I am thankful to all ARIES staff for their timely help whenever required.

I thank all my seniors, juniors and batchmates at ARIES for their support during my stay. I would also like to acknowledge my other friends for constantly encouraging me and making my life enjoyable, comfortable and pleasant.

Most importantly, I would like to express my deepest gratitude to my family for their love, blessings, and support throughout my life. A special thanks to my brother Mr. Tapan Pandey who encouraged me and supported me at every stage of my life.

Finally, I am grateful to God for everything He has given me in my life.

Ashwani Pandey

Abstract

Blazars, comprising BL Lacertae objects (BL Lacs; featureless optical spectra) and flat-spectrum radio quasars (FSRQs; strong broad emission lines in optical spectra), are the active galactic nuclei (AGNs) with strong relativistic jets pointing towards the direction of the observer. Their double humped spectral energy distributions (SEDs) extend from radio to very high energy γ -rays. TeV (Tera-electron Volt) blazars, those significantly observed at TeV energies, are mostly the high-frequency peaked BL Lac objects (HBLs), that is, the first hump of their SED peaks at optical to X-ray energy bands. In this thesis, we performed the hard X-ray (3–79 keV) and optical variability study of TeV HBLs on intraday timescales (occurring over less than a day) to better understand their fine structures and the underlying emission processes at these frequencies.

In the first part of the thesis, we have examined 46 hard X-ray light curves (LCs) of all (11) the TeV HBLs that have been observed with the *NuSTAR* satellite for intraday flux and spectral variability. We detected strong intraday variability (IDV) in the LCs of six TeV HBLs. Using discrete autocorrelation function (ACF) we found evidence for variability timescales ranging from 2.5 to 57.4 ks in the twelve LCs of four TeV HBLs. For these four TeV HBLs, we have constrained the values of magnetic field strength (B), electron Lorentz factor (γ) and the emitting region size (R) using their minimum variability timescales. We observed positive correlations with zero time lag between soft (3–10 keV) and hard (10–79 keV) bands for most of the LCs, indicating that their emissions are produced by same electron population. Using hardness ratio analysis, we noticed that the 3–79 keV spectra of Mrk 421 and Mrk 501 follow a general “harder-when-brighter” behavior. We also found that the hard X-ray spectra of TeV HBLs are usually curved and fitted well by the log-parabola model.

The second part of the thesis consists of the results of optical (*BVRI*) variability study of five TeV HBLs performed during 2016–2018. We have examined 61 optical LCs of five TeV HBLs for IDV using two latest statistical tests: the power-enhanced

F-test and the nested analysis of variance (ANOVA) test. We found evidence of significant IDV with very small variability amplitudes only in six LCs. No temporal variation was seen in the $V - R$ color on IDV timescale. We did not find any strong correlation between the $V - R$ color and the R band magnitude. On STV/LTV timescales, flux variations were seen at all the observed optical wavelengths, while temporal variations were also seen in the color indices. We generated the optical SEDs of TeV blazars and fitted them with a single power law ($F_\nu \propto \nu^{-\alpha}$) to examine the variations in their optical spectral indices during our monitoring period.

List of Publications

(in Peer Reviewed Journals)

(A) Related to thesis

1. “*X-ray Intra-day Variability of Five TeV Blazars with NuSTAR*”,
Ashwani Pandey, Alok C. Gupta, & Paul J. Wiita,
Astrophysical Journal, **841**, 123 (17pp), 2017.
2. “*X-ray Flux and Spectral Variability of Six TeV Blazars with NuSTAR*”,
Ashwani Pandey, Alok C. Gupta, & Paul J. Wiita,
Astrophysical Journal, **859**, 49 (11pp), 2018.
3. “*Optical Flux and Spectral Variability of the TeV Blazar PG 1553+113*”,
Ashwani Pandey, Alok C. Gupta, Paul J. Wiita, & S. N. Tiwari,
Astrophysical Journal, **871**, 192 (8pp), 2019.

(B) Not related to thesis

1. “*Multiband Optical Variability of the Blazar OJ 287 During Its Outbursts in 2015-2016*”,
Alok C. Gupta, Aditi Agarwal, Alka Mishra, H. Gaur, P. J. Wiita, M. F. Gu, O. M. Kurtanidze, G. Damljanovic, M. Uemura, E. Semkov, A. Strigachev, R. Bachev, O. Vince, Z. Zhang, B. Villarroel, P. Kushwaha, **Ashwani Pandey**, T. Abe, R. Chanishvili, R. A. Chigladze, J. H. Fan, J. Hirochi, R. Itoh, Y. Kanda, M. Kawabata, G. N. Kimeridze, S. O. Kurtanidze,

G. Latev, R. V. Muñoz Dimitrova, T. Nakaoka, M. G. Nikolashvili, K. Shiki, L. A. Sigua, & B. Spassov,
Monthly Notices of the Royal Astronomical Society, **465**, 4423–4433, 2017.

2. “*X-ray Intraday Variability of the TeV Blazar Mrk 421 with Chandra*”, Vishi Aggrawal, **Ashwani Pandey**, Alok C. Gupta, Paul J. Wiita, K. K. Yadav, & S. N. Tiwari, **Monthly Notices of the Royal Astronomical Society**, **480**, 4873–4883, 2018.
3. “*Characterizing Optical Variability of OJ 287 in 2016–2017*”, Alok C. Gupta, Haritma Gaur, Paul J. Wiita, **Ashwani Pandey**, P. Kushwaha, S. M. Hu, O. M. Kurtanidze, E. Semkov, G. Damljanovic, A. Goyal, M. Uemura, A. Darriba, Xu Chen, O. Vince, M. F. Gu, Z. Zhang, R. Bachev, R. Chanishvili, R. Itoh, M. Kawabata, S. O. Kurtanidze, T. Nakaoka, M. G. Nikolashvili, L. Stawarz, & A. Strigachev, **Astronomical Journal**, **157**, 95 (12pp), 2019.

Abbreviations and Acronyms

ACF	Auto Correlation Function
AD	Accretion Disk
AGN	Active Galactic Nucleus
ANOVA	Analysis of Variance
ARF	Ancillary Response File
BL Lacs	BL Lacertae objects
BLR	Broad Line Region
BLRG	Broad Line Radio Galaxy
BWB	Bluer-When-Brighter
CCD	Charge Coupled Device
CI	Color Index
DAOPHOT	Dominion Astronomical Observatory Photometry
DCF	Discrete Correlation Function
Dec	Declination
DFOT	Devasthal Fast Optical Telescope
DLC	Differential Light Curve
EC	External Compton
EM	Electromagnetic
EW	Equivalent Width
FITS	Flexible Image Transport System
FoV	Field of View
FPMA	Focal Plane Module A
FPMB	Focal Plane Module B
FR I	Fanaroff–Riley type I
FR II	Fanaroff–Riley type II
FSRQ	Flat Spectrum Radio Quasar
FWHM	Full Width at Half Maximum

GeV	Giga-electron Volt
HAGAR	High Altitude Gamma Ray
HAWC	High Altitude Water Cherenkov Observatory
HBL	High energy peaked BL Lacs
HEAO	High Energy Astronomy Observatory
HEASARC	High Energy Astrophysics Science Archive Research Center
HESS	High Energy Stereoscopic System
HR	Hardness Ratio
HSP	High Synchrotron Peaked blazar
IBL	Intermediate energy peaked BL Lacs
IC	Inverse Compton
IDV	Intra Day Variability
IPC	Imaging Proportional Counter
IRAF	Image Reduction and Analysis Facility
IR	Infrared
ISP	Intermediate Synchrotron Peaked blazar
kpc	Kilo-parsec
LBL	Low energy peaked BL Lacs
LC	Light Curve
LP	Log-Parabola
LSP	Low Synchrotron Peaked Blazar
LTV	Long Term Variability
MAGIC	Major Atmospheric Gamma-ray Imaging Cherenkov Telescopes
Mpc	Mega-parsec
NLRG	Narrow Line Radio Galaxy
NLR	Narrow Line Region
NuSTAR	Nuclear Spectroscopic Telescope Array
PL	Power-Law
QSO	Quasi-Stellar Object
RA	Right Ascension
RC	Ritchey-Chretien
RL	Radio Loud
RMF	Redistribution Matrix File
RQ	Radio Quiet
RWB	Redder-When-Brighter
SAA	South Atlantic Anomaly
SED	Spectral Energy Distribution
SMBH	Super Massive Black Hole

SSC	Synchrotron Self Compton
ST	Sampurnanand Telescope
STV	Short Term Variability
TeV	Tera-electron Volt
UV	Ultraviolet
VERITAS	Very Energetic Radiation Imaging Telescope Array System
VHE	Very High Energy

Contents

List of Figures	xxiii
List of Tables	xxv
1 Introduction	1
1.1 Active Galactic Nuclei (AGNs)	1
1.1.1 A Brief History of AGN	1
1.1.2 Basic Components of AGN	2
1.1.3 AGN Taxonomy and Unification Model	4
1.2 Blazar: an extreme subclass of AGN	6
1.2.1 Classification of Blazars	8
1.2.2 TeV Blazars	8
1.3 Emission Processes in Blazars	10
1.3.1 Thermal Emission	10
1.3.1.1 Black Body Radiation	10
1.3.2 Non-Thermal Emission	11
1.3.2.1 Synchrotron Emission	12
1.3.2.2 Inverse-Compton Emission	13
1.3.2.3 Hadronic Processes	15
1.4 Blazar Variability	16
1.5 Variability Models	16
1.5.1 Shock-in-jet Models	16
1.5.2 Turbulent Jet Models	17
1.5.3 Geometric Models	18
1.5.4 Models for Rapid Variability	19
1.5.4.1 Needle Model	19
1.5.4.2 Jets-in-a-Jet Model	19
1.6 Thesis Motivation	20
1.7 Thesis Structure	21
2 Multiwavelength Observations and Data Reduction	23
2.1 X-ray Observations	23
2.1.1 The Nuclear Spectroscopic Telescope Array (<i>NuSTAR</i>)	24
2.1.1.1 <i>NuSTAR</i> Optics	24
2.1.1.2 <i>NuSTAR</i> Detectors	24

CONTENTS

2.1.2	<i>NuSTAR</i> Data Analysis	25
2.2	Optical Observations	28
2.2.1	Telescopes	28
2.2.1.1	1.3 meter Devasthal Fast Optical Telescope	28
2.2.1.2	1.04 meter Sampurnanand Telescope	29
2.2.2	Optical Photometric Data Analysis	30
2.2.2.1	Pre-Processing	30
2.2.2.2	Processing	32
2.2.2.3	Post-Processing	35
3	X-ray Flux and Spectral Variability of TeV Blazars with <i>NuSTAR</i>	39
3.1	Introduction	39
3.2	<i>NuSTAR</i> Data Selection and Processing	40
3.2.1	Data Selection Criteria	40
3.2.2	Data Reduction	41
3.3	Analysis Techniques	43
3.3.1	Excess Variance	43
3.3.2	Discrete Correlation Function	44
3.3.3	Hardness Ratio	48
3.3.4	Spectral Fitting	49
3.4	Results	49
3.4.1	1ES 0229+200	49
3.4.2	1ES 0347–121	63
3.4.3	1ES 0414+009	63
3.4.4	RGB J0710+591	64
3.4.5	1ES 1101–232	64
3.4.6	Mrk 421	65
3.4.7	1ES 1218+304	67
3.4.8	Mrk 501	68
3.4.9	1ES 1959+650	69
3.4.10	PKS 2155–304	69
3.4.11	H 2356–309	70
3.5	Discussion	71
3.5.1	X-ray Flux Variability	71
3.5.2	Constraints on Physical Parameters using X-ray Variability Timescale	72
3.5.3	Correlation Between X-ray Emissions in Soft and Hard Energy Bands	73
3.5.4	X-ray Spectra	75
3.6	Conclusions	76
4	Optical Flux and Spectral Variability of TeV Blazars	79
4.1	Introduction	79
4.2	Observations and Data Reduction	80
4.3	Analysis Techniques	85

4.3.1	Power-enhanced <i>F</i> -test	85
4.3.2	Nested ANOVA	86
4.3.3	Intraday Variability Amplitude	87
4.4	Results	88
4.4.1	Flux Variability	88
4.4.1.1	1ES 0229+200	88
4.4.1.2	1ES 0414+009	88
4.4.1.3	1ES 0806+524	89
4.4.1.4	PG 1553+113	90
4.4.1.5	1ES 2344+514	91
4.4.2	Spectral Variability	93
4.4.2.1	1ES 0806+524	96
4.4.2.2	PG 1553+113	98
4.4.3	Spectral Energy Distributions (SEDs)	99
4.4.3.1	1ES 0414+009	101
4.4.3.2	1ES 0806+524	102
4.4.3.3	PG 1553+113	102
4.4.3.4	1ES 2344+514	103
4.5	Discussion and Conlcusions	106
5	Summary, Conclusions and Future Plans	111
5.1	Summary	111
5.1.1	Hard X-ray Studies of TeV Blazars	111
5.1.2	Optical Studies of TeV Blazars	112
5.2	Conclusions	113
5.3	Future Plans	114
References		125
Appendix: Finding Charts and Comparison Stars		127
A.1	1ES 0229+200	127
A.2	1ES 0414+009	128
A.3	1ES 0806+524	129
A.4	1ES 1553+113	130
A.5	1ES 2344+514	131

List of Figures

1.1	Schematic representation of the basic AGN components and the unification scheme of AGNs	3
1.2	A color composite image of Centaurus A	6
1.3	Schematic representation of the broadband SED of blazar	9
1.4	Map of TeV sources	9
1.5	Black body spectrum at different temperatures	11
1.6	Total synchrotron power F of a single electron as a function of frequency ν	13
1.7	The spectrum of synchrotron radiation from a homogenous electron plasma as a function of frequency ν	14
1.8	Sketch of the shock-in-jet model	17
1.9	Sketch of physical features of a blazar	18
1.10	Sketch of the geometry of ‘jets-in-a-jet’ model	20
2.1	Diagram of the <i>NuSTAR</i> observatory.	25
2.2	Comparison of effective area of <i>NuSTAR</i> with that of other focusing telescopes.	26
2.3	Photograph of the <i>NuSTAR</i> focal plane module (FPM).	26
2.4	<i>NuSTARDAS</i> data processing stages.	27
2.5	The telescopes used for observations	29
2.6	Stages of optical photometric data analysis	31
2.7	Steps of image pre-processing	33
3.1a	<i>NuSTAR</i> LCs of the TeV HBLs 1ES 0229+200, 1ES 0347–121, 1ES 0414+009, RGB J0710+591, 1ES 1101–232 and Mrk 421.	45
3.1b	<i>NuSTAR</i> LCs of the TeV HBLs Mrk 421 and 1ES 1218+304.	46
3.1c	<i>NuSTAR</i> LCs of the TeV HBLs Mrk 501, 1ES 1959+650, PKS 2155–304 and H 2356–309.	47
3.2a	ACFs for LCs of the blazars 1ES 0229+200, 1ES 0347–121, 1ES 0414+009, RGB J0710+591, 1ES 1101–232 and Mrk 421.	50
3.2b	ACFs for LCs of the blazars Mrk 421 and 1ES 1218+304.	51
3.2c	ACFs for LCs of the blazars Mrk 501, 1ES 1959+650, PKS 2155–304 and H 2356–309.	52
3.3a	Soft and hard band LCs, HR plots, and the DCF plots of the blazars 1ES 0229+200, 1ES 0347–121, 1ES 0414+009, and RGB J0710+591	53
3.3b	As in Figure 3.3a, but for 1ES 1101–232 and Mrk 421.	54

LIST OF FIGURES

3.3c As in Figure 3.3a, but for Mrk 421.	55
3.3d As in Figure 3.3a, but for Mrk 421.	56
3.3e As in Figure 3.3a, but for Mrk 421, and 1ES 1218+304.	57
3.3f As in Figure 3.3a, but for Mrk 501, and 1ES 1959+650.	58
3.3g As in Figure 3.3a, but for PKS 2155–304.	59
3.3h As in Figure 3.3a, but for PKS 2155–304 and H 2356–309.	62
3.4 Short term variability of Mrk 421	67
3.5a Model-fitted <i>NuSTAR</i> spectra of TeV Blazars 1ES 0347–121, 1ES 0414+009, RGB J0710+591, and 1ES 1101–232	74
3.5b As in Figure 3.5a, but for 1ES 1218+304 and H 2356–309.	75
4.1a Optical LCs of TeV HBLs 1ES 0229+200, 1ES 0414+009 and 1ES 0806+524	82
4.1b Optical LCs of TeV HBLs 1ES 0806+524 and 1ES 1553+113	83
4.1c Optical LCs of TeV HBLs 1ES 1553+113 and 1ES 2344+514	84
4.2a LTV optical LCs of 1ES 0229+200	93
4.2b LTV optical LCs of 1ES 0414+009	94
4.2c LTV optical LCs of 1ES 0806+524	95
4.2d STV optical LCs of PG 1553+113	96
4.2e LTV optical LCs of 1ES 2344+514	97
4.3a IDV color-time plots for 1ES 0806+524	99
4.3b IDV color-time plots for PG 1553+113	100
4.4a IDV color-magnitude plots for 1ES 0806+524	101
4.4b IDV color-magnitude plots for PG 1553+113	102
4.5a SED of 1ES 0414+009 in V, R, and I bands	104
4.5b SED of 1ES 0806+524 in V, R, and I bands	104
4.5c SED of PG 1553+113 in V, R, and I bands	106
4.5d SED of 1ES 2344+514 in V, R, and I bands	107
4.6 Variation in mean optical spectral index with time for TeV blazars	108

List of Tables

2.1	Details of telescopes and instruments used.	29
2.2	The broadband filters used for observations	30
3.1	RA, Dec and Redshift of the TeV Blazars.	41
3.2	Observation log of <i>NuSTAR</i> data for TeV HBLs.	42
3.3	Source and background region sizes	43
3.4	X-ray variability parameters.	60
3.5	Model fits to the NuSTAR spectra	61
3.6	Different model parameters for <i>NuSTAR</i> TeV HBLs	73
4.1	Right Ascension, Declination and Redshift of the observed TeV Blazars.	80
4.2	Observation log of optical photometric observations of TeV Blazars.	81
4.3	Results of IDV analyses of TeV Blazars	92
4.4	Linear fits to color-magnitude plots	103
4.5	Galactic extinction coefficients for the TeV blazars.	103
4.6	Straight line fits to optical SEDs of TeV blazars	105

Chapter 1

Introduction

1.1 Active Galactic Nuclei (AGNs)

A small fraction ($\sim 10\%$) of galaxies in our universe has a compact, highly luminous ($L \sim 10^{44-48}$ ergs/s) central region that emits radiation comparable to or sometimes even higher than the radiation emitted by the rest of the galaxy. Such galaxies often show strong broad emission line spectra and produce variable emissions that extend from radio to X-rays or in some cases up to very high energy γ -rays. These galaxies are called ‘active galaxies’ and their nuclei are termed as ‘Active Galactic Nuclei’ (AGNs). Some AGNs are known to host relativistic bipolar outflows or jets that emit non-thermal continuum emission from radio to γ -rays. Because of these extraordinary features, AGNs have been attracting researchers for a long time.

1.1.1 A Brief History of AGN

In 1908, E.A. Fath at Lick Observatory detected strong emission lines in the optical spectra of nebula NGC 1068 which was different from the usually seen absorption spectra of normal galaxies. Later, Carl Seyfert, in 1943, also observed strong broad emission lines in the optical spectra of six spiral galaxies having high central surface brightness and hence realized that they form a distinct class ([Seyfert, 1943](#)).

In the late 1950s, the first radio surveys of the sky were performed and several catalogues e.g. the Third Cambridge Catalogue (3C), were published. [Hazard et al.](#)

1. INTRODUCTION

(1963) investigated the spectrum of the radio source 3C 273 by the lunar occultation method and observed broad emission lines in it. Later, Schmidt (1963) studied the optical spectra of 3C 273 and obtained a redshift of $z = 0.158$, identifying it as an extragalactic source. He also realized that the star-like radio source 3C 273 was actually the nuclear region of a galaxy that was about 100 times brighter than the galaxy at optical wavelengths. Such radio sources formed a new class of AGNs and were named quasars (or QSOs; Quasi-Stellar Objects) by Hong-Yee Chiu, in 1964.

The ultimate energy source and the radiation mechanisms of AGNs were a big mystery. The idea of accretion of matter onto a supermassive black hole (SMBH) was proposed in the 1960s to explain this phenomenon by several astrophysicist (e.g. Salpeter, 1964; Lynden-Bell, 1969). The discovery of rapid X-ray flare from Cygnus X-1, a Galactic X-ray source, by Oda et al. (1971) triggered the possibility for the presence of an accreting black hole in AGNs. Later, Rees (1984) suggested that the source of radiation from the AGN was an accreting SMBH lying at the center of the AGN.

1.1.2 Basic Components of AGN

According to the current paradigm, the fundamental components of AGN, Figure 1.1, are followings (Ghisellini, 2013):

- **Supermassive Black Hole (SMBH):** A black hole with mass $M_{BH} \sim 10^6 - 10^9 M_\odot$ at the center, which pulls matter from the surroundings due to its high gravitational field.
- **Accretion Disk (AD):** Matter attracted by the gravity of the central SMBH forms a spiraling disk, known as ‘accretion disk’.
- **X-ray corona:** The AD is sandwiched by a corona of hot plasma which inverse Comptonizes the optical/ultraviolet (UV) disk photons to produce X-rays.
- **Broad Line Region (BLR):** A region of small rapidly (~ 3000 km/s) moving, dense ($\sim 10^{10}$ cm $^{-3}$) gas clouds is located at a distance of $\sim 0.1 - 1.0$ pc from the SMBH. A fraction (10%) of the disk radiation is reprocessed by these clouds to give rise to emission lines in the spectra. These emission lines get broaden due to Doppler shifts and hence this region is known as ‘broad line region’.

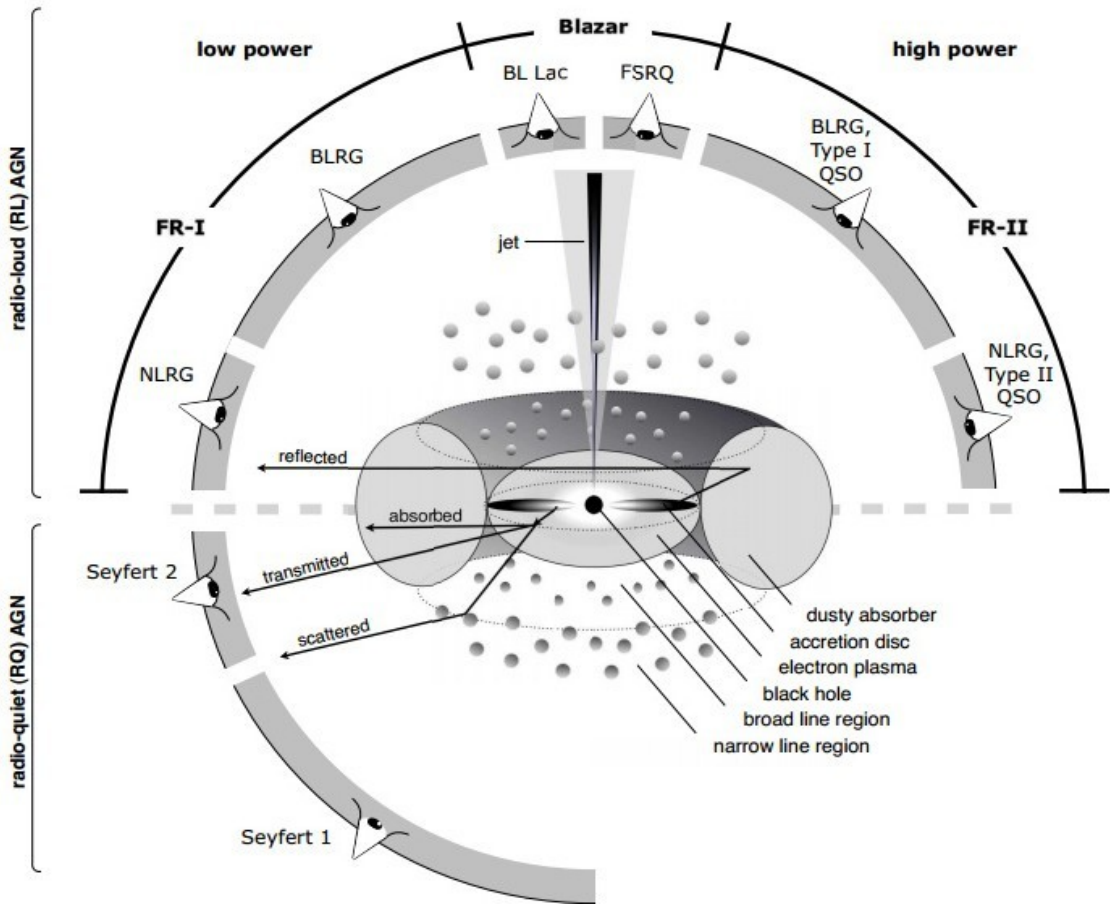


Figure 1.1: Schematic representation of the basic AGN components and the unification scheme of AGNs (adopted from [Beckmann & Shrader \(2012\)](#)).

- **Obscuring Torus:** At a distance of several parsecs ($\sim 1 - 10$ pc) from the SMBH, there exists a dusty torus which obscures the radiations from the central regions (SMBH, AD, and BLR) and re-emits them in the infrared (IR) bands.
- **Narrow Line Region (NLR):** Similar to BLR, there is another region of relatively less dense ($\sim 10^3 \text{ cm}^{-3}$) gas clouds at larger distance (~ 100 pc) from the SMBH. These clouds are moving with lower velocities ($\sim 300 \text{ km/s}$) and are responsible for the narrow lines in the spectra. This region is known as ‘narrow line region’.
- **Relativistic Jets:** Jets are the magnetically collimated bipolar outflows of relativistic plasma and are often observed in certain AGNs. They are thought to originate from the vicinity of SMBH and can extend up to few kpc (or sometimes up to Mpc) distances.

1. INTRODUCTION

1.1.3 AGN Taxonomy and Unification Model

Since various types of AGNs were discovered at different wavelengths with different properties, their taxonomy is very complex and confusing. In general, AGNs are classified in the following ways:

- AGNs are broadly classified as radio-loud (RL; only $\sim 10\%$) AGNs and radio-quiet (RQ; $\sim 90\%$) AGNs, Figure 1.1, on the basis of the radio loudness parameter (R_L), which is defined as

$$R_L = \frac{F_{5GHz}}{F_B} \quad (1.1)$$

where F_{5GHz} is the radio flux density at 5 GHz and F_B is the optical flux density in B band. For RL AGNs, $R_L \geq 10$ and for RQ AGNs $R_L < 10$ (Kellermann et al., 1989). RL AGNs show powerful bipolar relativistic jets, while in RQ AGNs jets are either absent or very weak. RL AGNs often reside in elliptical galaxies, while the host galaxies for the RQ AGNs are either spiral or lenticular galaxies (Antonucci, 1993).

Seyfert galaxies are, in general¹, RQ AGNs having a lower luminosity and hence are generally observed at lower redshift ($z < 0.1$). Their host galaxies are spiral galaxies with high surface brightness central regions. They are mainly classified into Seyfert 1 and Seyfert 2 galaxies on the basis of their optical spectra. Optical spectra of Seyfert 1 galaxies show both broad and narrow emission lines while the optical spectra of Seyfert 2 galaxies consist of only narrow emission lines. Quasars are the most luminous subclass of AGNs and are observed at higher redshifts. They belong to both RL and RQ classes of AGNs. The strong radio emission in $\sim 10\%$ quasars (RL quasars) is produced via the synchrotron radiation from their relativistic jets and radio lobes. The RL quasars are often hosted by elliptical galaxies while the host galaxy for an RQ quasar is generally spiral galaxy. Their optical spectra are similar to Seyfert galaxies but they show relatively strong broad emission lines. Radio galaxies are the RL AGNs that exhibit strong radio emissions from bipolar jets and show bright central region at optical wavelengths. Figure 1.2 shows a color composite, radio, optical and X-ray images, of the nearest active galaxy Centaurus A which is a radio galaxy.

¹A good sample of narrow line Seyfert 1 (NLSy1) galaxies, a subclass of Seyfert galaxies, was also discovered as RL AGNs (Zhou et al., 2006; Rakshit et al., 2017).

In radio band observations relativistic bipolar jets can be clearly seen. Similar to Seyfert galaxies, radio galaxies are subclassified as broad-line radio galaxies (BLRGs; having both broad and narrow emission lines) and narrow line radio galaxies (NLRGs; having only narrow emission lines). They are generally hosted in elliptical galaxies. On the basis of radio morphology they are further divided into Fanaroff-Riley type I (FR I) and Fanaroff-Riley type II (FR II) ([Fanaroff & Riley, 1974](#)). FR I sources have core-brightened radio morphology while FR IIs are edge-brightened.

- On the basis of the strength of emission lines in optical/UV spectra, AGNs are divided into Type 1, Type 2, and Type 0 AGNs ([Urry & Padovani, 1995](#)). The spectra of Type-1 AGNs show both broad and narrow emission lines while only narrow emission lines are present in the spectra of Type-2 AGNs. A small number of AGNs show very unusual spectral features and are classified as Type 0 AGNs because they are related by a small angle (nearly 0 degrees) to the line of sight. These include blazars (BL Lacertae objects and Flat Spectrum Radio Quasars (FSRQs)) and broad absorption line (BAL) quasars.
- Recently, [Padovani \(2016\)](#) proposed that the AGNs should be classified as ‘jetted’ AGNs and ‘non-jetted’ AGNs on the basis of the presence or lack of strong relativistic jets. He pointed out that the ‘radio-loud’ and ‘radio-quiet’ labels are misleading and inappropriate, because the relative strength of radio emission in these two classes is just a consequence of the presence (or lack) of a strong relativistic jet.

The AGN unification model assumes that all AGNs are basically the same, and the observed differences between various classes of AGNs are only due to their orientation with respect observer’s line of sight, Figure 1.1. The AGN unification scheme was first proposed by [Antonucci \(1993\)](#). He pointed out that the presence of an optically thick torus around the central region was responsible for the absence of broad emission lines in the spectra of Seyfert 2 galaxies as they were observed edge-on so the BLR would be hidden. In Seyfert 1 galaxies, which are mostly observed face-on, BLR is not obscured by the torus so both broad and narrow emission lines are seen in their spectra. The unification scheme for RL AGNs was given by [Urry & Padovani \(1995\)](#) which requires both the axis-symmetric torus and the bipolar relativistic jets. In this unification model, blazars are observed along the jet direction, RL quasars and BLRGs are viewed at modest angles while NLRGs are observed edge-on (Figure 1.1).

1. INTRODUCTION

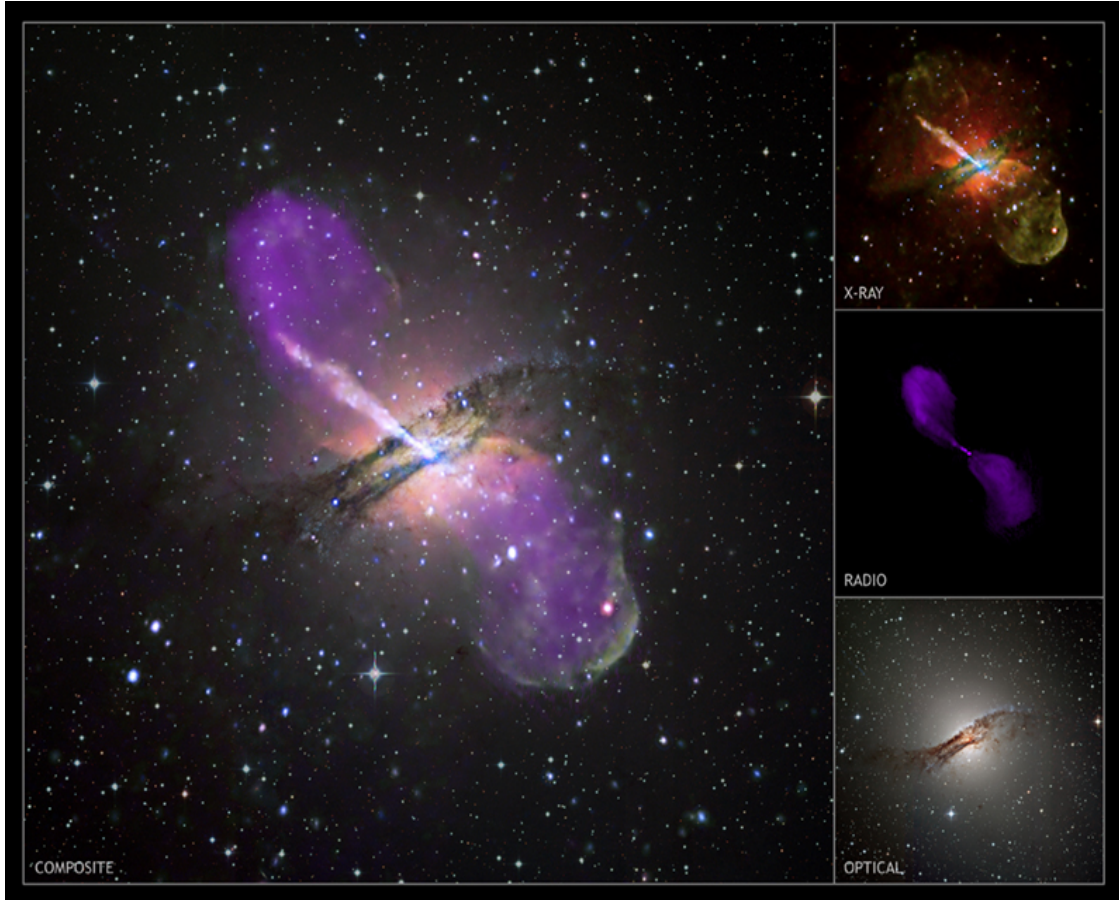


Figure 1.2: A color composite image of Centaurus A: a radio galaxy, which is the closest active galaxy to the Earth. The optical image was taken with very large telescope (VLT), radio image with very large array (VLA) and X-ray image with the *Chandra* satellite. Source: <https://apod.nasa.gov/apod/ap080110.html>.

1.2 Blazar: an extreme subclass of AGN

Blazars are ‘jetted’ AGNs that means they consist of strong relativistic jets. According to the old classification scheme, blazars are the RL AGNs understood to have relativistic jets pointing close ($\leq 10^\circ$; [Urry & Padovani \(1995\)](#)) to the line of sight of the observer, Figure 1.1. Following are the observational properties of blazars:

- Their broadband, radio to $\gamma-$ ray, emission is dominated by non-thermal emission coming from the relativistic jets.
- Their broadband spectral energy distribution (SED) exhibits two broad humps; lower one peaks in IR to X-ray energies while the higher one in the $\gamma-$ ray energies. The lower energy component is well known to be due to synchrotron emission.

- They exhibit rapid and strong flux variations on timescales ranging from few minutes to years over the entire electromagnetic spectrum (EM).
- They show high and variable radio to optical polarization.
- An apparent superluminal ('faster-than-light') motion is often seen in their high-resolution radio maps.

These observed properties of blazars are believed to be the manifestation of relativistic aberration (relativistic beaming) associated with the bulk motion of relativistic plasma along the line of sight of the observer, which results in Doppler boosting of frequency, flux and temporal characteristics (e.g. [Blandford & Rees, 1978](#)).

If a blob of plasma is moving with a velocity β ($=v/c$) at an angle θ to the observer's line of sight, then the observed apparent transverse velocity of the blob is given by ([Peterson, 1997](#))

$$\beta_{app} = \frac{\beta \sin \theta}{1 - \beta \cos \theta} \quad (1.2)$$

It shows that for $\beta \rightarrow 1$ and a small value of θ , $\beta_{app} > 1$, that is, for large jet velocities ($v \approx c$) and sufficiently small viewing angles (θ) the apparent transverse velocity of the blob becomes superluminal. The apparent transverse velocity will be maximum for $\cos \theta = \beta$ and is given by

$$\beta_{app}^{max} = \Gamma \beta \quad (1.3)$$

where Γ is the bulk Lorentz factor of the jet and is defined as

$$\Gamma = \frac{1}{\sqrt{1 - \beta^2}} \quad (1.4)$$

The Doppler factor is defined as

$$\delta = \frac{1}{\Gamma(1 - \beta \cos \theta)} \quad (1.5)$$

The Doppler boosted observed flux is given by ([Marscher, 1996](#))

$$\begin{aligned} F_{obs} &= \delta^{2+\alpha} F_{em} && \text{for steady flow,} \\ &= \delta^{3+\alpha} F_{em} && \text{for evolving blob} \end{aligned} \quad (1.6)$$

where α is the spectral index defined as, $F_\nu \propto \nu^{-\alpha}$ (ν is the frequency).

1. INTRODUCTION

1.2.1 Classification of Blazars

Different classification schemes for blazars are following:

(a) On the basis of the rest frame equivalent width (EW_{rest}) of the emission lines in optical/UV spectra, blazars are divided into two subclasses: BL Lacertae objects (BL Lacs) and FSRQs. BL Lacs have no detectable, or very weak ($\text{EW}_{rest} < 5\text{\AA}$; [Stocke et al. \(1991\)](#); [Marcha et al. \(1996\)](#)), emission lines, while FSRQs usually have strong broad emission lines.

(b) According to the rest frame synchrotron peak frequency (ν_{peak}^S), [Abdo et al. \(2010\)](#) classified blazars into low synchrotron peaked blazars (LSPs), intermediate synchrotron peaked blazars (ISPs), and high synchrotron peaked blazars (HSPs) as:

- LSPs : $\nu_{peak}^S \leq 10^{14} \text{ Hz}$
- ISPs : $10^{14} \text{ Hz} < \nu_{peak}^S < 10^{15} \text{ Hz}$
- HSPs : $\nu_{peak}^S \geq 10^{15} \text{ Hz}$

This is similar to the classification scheme given by [Padovani & Giommi \(1995\)](#) to further categorized BL Lacs into low-frequency peaked BL Lacs (LBLs) and high-frequency peaked BL Lacs (HBLs). The synchrotron component peaks in the IR/optical band in LBLs (and FSRQs), while it peaks in the UV/X-ray band in HBLs, Figure 1.3. The high energy component of the blazar SED goes to the γ -ray energy, peaking at GeV energies in LBLs and FSRQs, and at TeV energies in HBLs. LBLs and FSRQs are LSPs, while HBLs belong to HSPs. ISPs are also termed as intermediate-frequency peaked BL Lacs (IBLs).

1.2.2 TeV Blazars

Blazars significantly detected at TeV γ -ray energies form a new subclass of blazars, termed as TeV blazars. Mrk 421 is the first TeV blazar, detected by the Whipple Observatory γ -ray telescope ([Punch et al., 1992](#)). Until 2004, only eight TeV blazars (Mrk 421, Mrk 501, 3C 66A, 1ES 2344+514, PKS 2155–304, 1ES 1959+650, BL Lacertae and 1ES 1426+428) were known. Thanks to the *Fermi* satellite and the several ground-based TeV γ -ray facilities (e.g. *HESS* (High

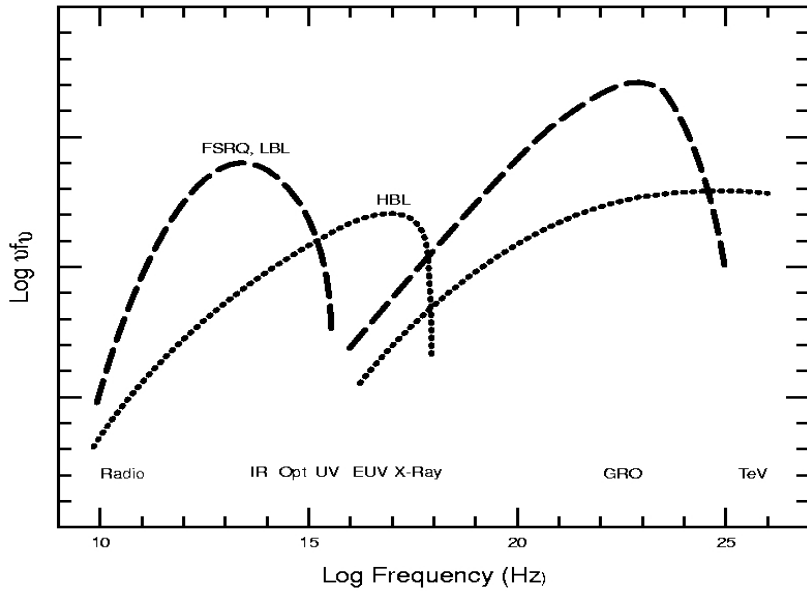


Figure 1.3: Schematic representation of the broadband SED of blazar representing the location of synchrotron peak for its different classes. Figure courtesy: [Urry \(1998\)](#)

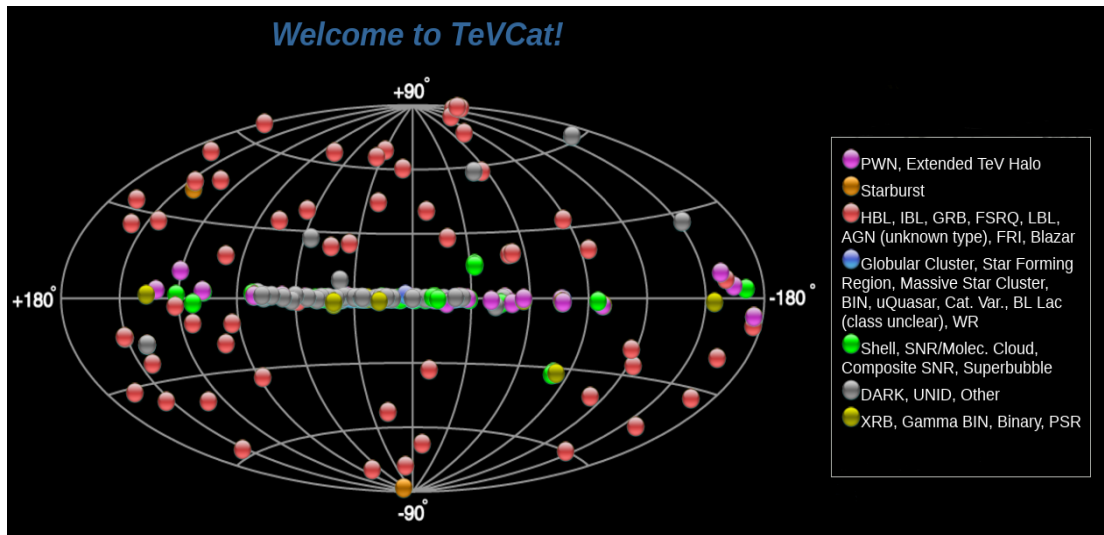


Figure 1.4: Map of TeV sources (taken from: <http://tevcat.uchicago.edu/>).

Energy Stereoscopic System), *MAGIC* (Major Atmospheric Gamma-ray Imaging Cherenkov Telescopes), *VERITAS* (Very Energetic Radiation Imaging Telescope Array System), and *HAWC* (High-Altitude Water Cherenkov Observatory) new TeV blazars have been discovered. Now blazars are the dominant extragalactic sources at TeV energies, Figure 1.4. In the TeV source catalogue (TeVCat²) the total number of blazars, till date, is 64. Most (48) of them are the HBLs. There are 8 IBLs, 2 LBLs, and 6 FSRQs.

²<http://tevcat.uchicago.edu>

1. INTRODUCTION

1.3 Emission Processes in Blazars

In this section, we briefly discuss the physical processes and mechanisms that give rise to the continuum emissions in blazars. A detailed description of these processes can be found in a number of texts e.g. [Rybicki & Lightman \(1986\)](#); [Longair \(2011\)](#). The broadband continuum emission of blazars mainly consists of non-thermal emission from the relativistic jets, however, the thermal emission from the accretion disks also contribute to the total emission.

1.3.1 Thermal Emission

Radiation emitted by matter in thermal equilibrium with its surroundings is known as thermal radiation. For an optically thick medium, it becomes black body radiation.

1.3.1.1 Black Body Radiation

Black body radiation is homogeneous, isotropic and unpolarized. It has a continuous emission spectrum which depends only on the surface temperature (T) and is given by the Planck law as follows:

$$B_\nu(T) = \frac{2h\nu^3/c^2}{\exp(h\nu/kT) - 1} \quad (1.7)$$

where B_ν is the radiation intensity per unit solid angle per unit frequency (ν), h is Planck constant, k is Boltzmann constant and c is the speed of light in vacuum. The total energy emitted per unit surface area per unit time over all frequencies by a black body is given by

$$J = \sigma T^4 \quad (1.8)$$

where σ is Stefan–Boltzmann constant. Equation 1.8 is known as Stefan-Boltzmann law. The black body spectrum, also known as Planck spectrum, peaks at the wavelength λ_{max} given by

$$\lambda_{max} = \frac{b}{T} \quad (1.9)$$

where b is Wien’s displacement constant. Equation 1.9 is known as Wien’s displacement law. Figure 1.5 illustrates the black body spectrum at different temperatures.

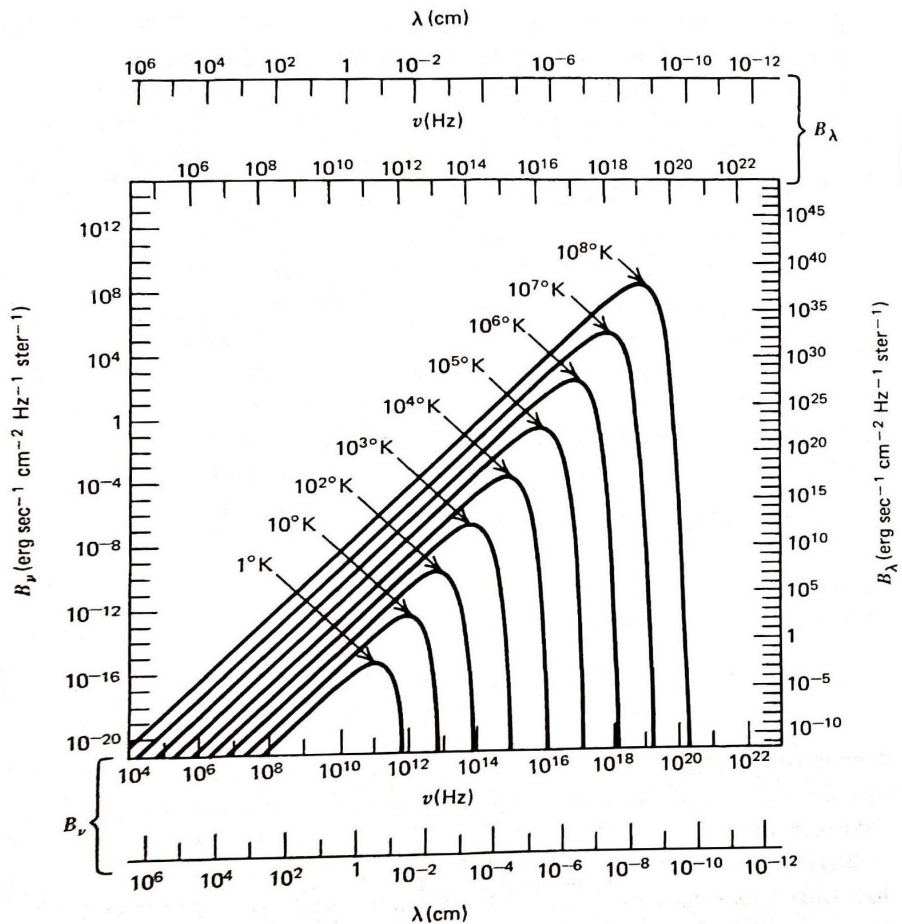


Figure 1.5: Black body spectrum at different temperatures (adapted from Rybicki & Lightman (1986)).

1.3.2 Non-Thermal Emission

Radiation that doesn't depend on the thermal energy (temperature) of the source is known as non-thermal emission. The broadband emission of blazars is dominated by non-thermal emission. The low energy component of the blazar SED is well understood to be due to synchrotron emission, while the high energy component is attributed to either the inverse-Compton (IC) scattering (leptonic models) or the hadronic processes (hadronic models).

1. INTRODUCTION

1.3.2.1 Synchrotron Emission

A charged particle gyrating around the magnetic field lines emits radiation. At non-relativistic velocities, this radiation is called cyclotron radiation while at relativistic velocities it is known as synchrotron radiation. The power emitted by an electron of energy $\gamma m_e c^2$, moving with a velocity $\beta (= v/c)$ in a magnetic field B is given by

$$P = \frac{2}{3} r_0^2 c \gamma^2 B^2 \beta^2 \sin^2 \alpha \quad (1.10)$$

where $r_0^2 = e^2/m_e c^2$ is the classical electron radius and α , known as pitch angle, is the angle between the electron velocity and magnetic field line. For an isotropic distribution of particles, the average synchrotron power can be obtained as

$$\begin{aligned} \langle P_{syn} \rangle &= \frac{1}{4\pi} \frac{2}{3} r_0^2 c \gamma^2 B^2 \beta^2 \int \sin^2 \alpha d\Omega \\ &= \frac{4}{3} \sigma_T c \beta^2 \gamma^2 U_B \end{aligned} \quad (1.11)$$

where Ω is the solid angle, $\sigma_T = 8\pi r_0^2/3$ is the Thomson cross-section, and $U_B = B^2/8\pi$ is the magnetic energy density.

After emitting synchrotron radiation the electrons in plasma cool down and the timescale for this to occur, **synchrotron cooling timescale**, is given by

$$t_{cool} = \frac{\gamma m_e c^2}{\langle P_{syn} \rangle} = \frac{\gamma m_e c^2}{(4/3) \sigma_T c \beta^2 \gamma^2 U_B} \sim \frac{7.74 \times 10^8}{B^2 \gamma} \quad (1.12)$$

The synchrotron spectrum of a single electron peaks at a frequency $\nu = 0.29\nu_c$, Figure 1.6, where ν_c is the critical frequency given by

$$\nu = \frac{3\gamma^2 e B \sin \alpha}{2m_e c} \quad (1.13)$$

For a power-law electron energy distribution given by

$$N(\gamma) = C \gamma^{-p} \quad (1.14)$$

the resulting synchrotron spectrum will be a power law of the form

$$P(\nu) \propto \nu^{-\alpha}, \alpha = \frac{p-1}{2} \quad (1.15)$$

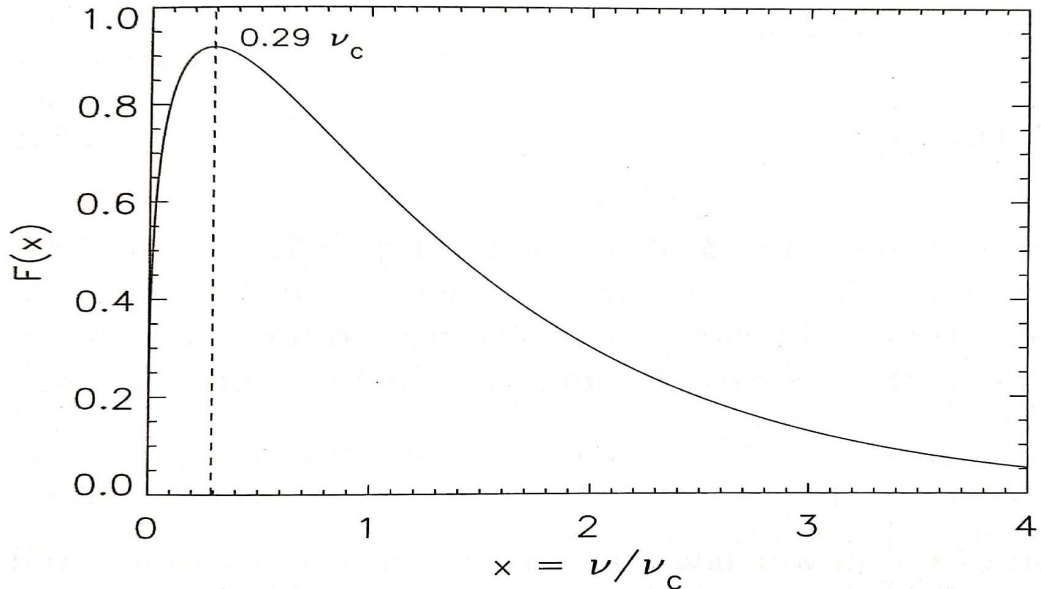


Figure 1.6: Total synchrotron power F of a single electron as a function of frequency ν (in units of ν_c). Picture taken from Beckmann & Shrader (2012).

At low frequencies the emitting plasma is optically thick, causing the absorption of emitted synchrotron photons by the emitting particles itself, a process known as **synchrotron-self absorption (SSA)**. The observed spectrum is independent of the energy distribution of particles at low frequencies and varies as $\nu^{-5/2}$ while at high frequencies the plasma is optically thin, hence the spectrum falls with $\nu^{(1-p)/2}$, Figure 1.7. The frequency at which the spectrum attains its maximum value is called the synchrotron self-absorption frequency, ν_{sa} .

1.3.2.2 Inverse-Compton Emission

When the low energy photons interact with the highly relativistic particles they get scattered to high energies. This process is known as inverse-Compton scattering. Inverse-Compton is believed to be an important mechanism for the production of X-ray/γ-ray emissions by the scattering of low energy emissions (IR/optical) in blazars. When the energy of incoming photon in electron's rest frame is very much smaller than the rest mass energy of electron the scattering is considered as elastic and is characterized by Thomson cross section. On the other hand, when the energy of the incident photon is much higher than the electron's rest mass energy the scattering is inelastic and is described by the Klein-Nishina (KN) cross section. Thus,

1. INTRODUCTION

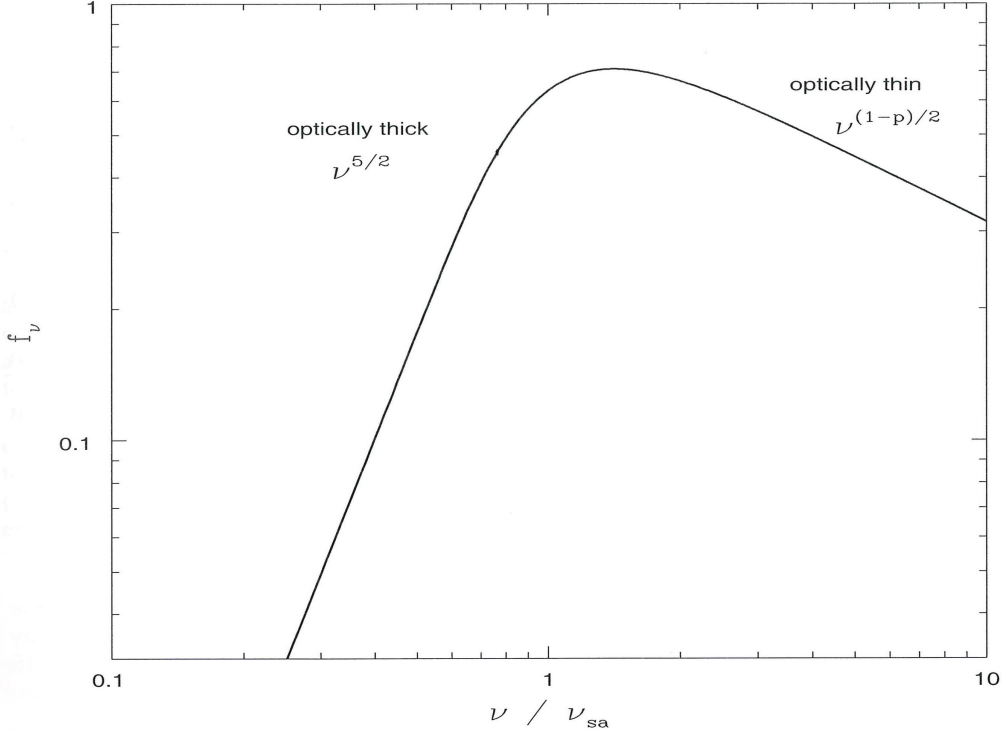


Figure 1.7: The spectrum of synchrotron radiation from a homogenous electron plasma as a function of frequency ν (in units of ν_c). Picture taken from [Beckmann & Shrader \(2012\)](#).

in Thomson regime,

$$\gamma\epsilon \ll m_e c^2 \quad (1.16)$$

and the differential cross section is given by

$$\frac{d\sigma_T}{d\Omega} = \frac{1}{2} r_0^2 (1 + \cos^2 \theta) \quad (1.17)$$

where θ is the scattering angle.

In KN regime,

$$\gamma\epsilon \gg m_e c^2 \quad (1.18)$$

and the differential cross section is given by

$$\frac{d\sigma_{KN}}{d\Omega} = \frac{r_0^2 \epsilon_s^2}{2\epsilon^2} \left(\frac{\epsilon_s}{\epsilon} + \frac{\epsilon}{\epsilon_s} - \sin^2 \theta \right) \quad (1.19)$$

where ϵ and ϵ_s are the energies of incoming and scattered photons, respectively.

In blazars, the low energy photons (or seed photons) for IC scattering are either the synchrotron photons generated by the same electron populations in the jet or the photons originated from the regions external to jet, e.g. accretion disk,

BLR or dusty torus. When the relativistic electrons scatter their own low energy synchrotron photons to high energy, the process is known as **synchrotron-self Compton (SSC)**. While the process of scattering of external low energy photons to high energy by the highly relativistic electrons is known as **external Compton (EC)**.

1.3.2.3 Hadronic Processes

When protons are accelerated along with electrons in the blazar jet to sufficiently high energies, the hadronic processes play significant role in blazar emissions. The acceleration of protons to the necessary high energies requires strong magnetic fields of ~ 10 Gauss (G) ([Mücke et al., 2003](#)). In such a high magnetic field, the following processes dominate:

- Proton (p)–Photon (γ) Interactions (known as Bethe-Heitler Process):

$$p + \gamma \rightarrow p + e^\pm \quad (1.20)$$

- Photo–Meson Production:

$$p + \gamma \rightarrow p + \pi^0 \quad (1.21)$$

$$p + \gamma \rightarrow n + \pi^+(\pi^-) \quad (1.22)$$

- Meson and Muon Decays:

$$\pi^0 \rightarrow 2\gamma \quad \text{or} \quad \pi^0 \rightarrow e^+ + e^- + \gamma \quad (1.23)$$

$$\pi^+(\pi^-) \rightarrow \mu^+(\mu^-) + \nu_\mu(\bar{\nu}_\mu) \quad (1.24)$$

$$\mu^+(\mu^-) \rightarrow e^+(e^-) + \nu_{e^-}(\bar{\nu}_{e^-}) \quad (1.25)$$

The synchrotron photons radiated by the co-accelerated relativistic electrons serve as the target radiation field for these processes ([Mücke et al., 2003](#)). The high energy photons are produced from photomeson production, and from synchrotron radiation of proton and muon in the strong magnetic field.

The “ π^0 cascades” and “ π^\pm cascades” produce featureless γ -ray spectra while the “ p –synchrotron cascades” and “ μ^\pm –synchrotron cascades” generate a typical

1. INTRODUCTION

double-humped SED observed in TeV blazars ([Mücke & Protheroe, 2001](#); [Mücke et al., 2003](#)).

1.4 Blazar Variability

One of the important characteristics of blazars is that their brightness varies over the entire EM spectrum on a wide range of time-scales. The variability timescale (t_{var}) can be used to constrain the size (R) of the emitting regions using the light-crossing arguments as

$$R \leq \frac{ct_{var}\delta}{(1+z)} \quad (1.26)$$

where δ is the Doppler factor and z is the redshift of the blazar. Blazar variability is often classified as: intra-day variability (IDV), also called microvariability or intra-night variability for detectable variations seen to occur over less than a day ([Wagner & Witzel, 1995](#)); short term variability (STV) for fluctuations over a few days to a few months; and long term variability (LTV) for changes seen over longer periods ([Gupta et al., 2004](#))).

1.5 Variability Models

Since in blazars the Doppler boosted non-thermal continuum emission from the relativistic jet completely overshines the AD emission, the variability on any measurable timescale is most likely explained by the relativistic jet based models. However, in very low flux states, the instabilities or hot spots on the accretion disk can also produce variations on IDV and STV timescales ([Mangalam & Wiita, 1993](#); [Chakrabarti & Wiita, 1993](#)). Different jet based models proposed to explain the variability on different timescales are briefly discussed in the following sections.

1.5.1 Shock-in-jet Models

Much of the long term (months to years) blazar variability can reasonably be explained by the shock-in-jet models ([Marscher & Gear, 1985](#)). Major increases in the bulk speed or the internal energy of the jet flow results in the formation of shock waves which propagate down the jet ([Marscher, 1996](#)). These shock waves decelerate supersonic jet flows to subsonic speeds. A shock front compresses

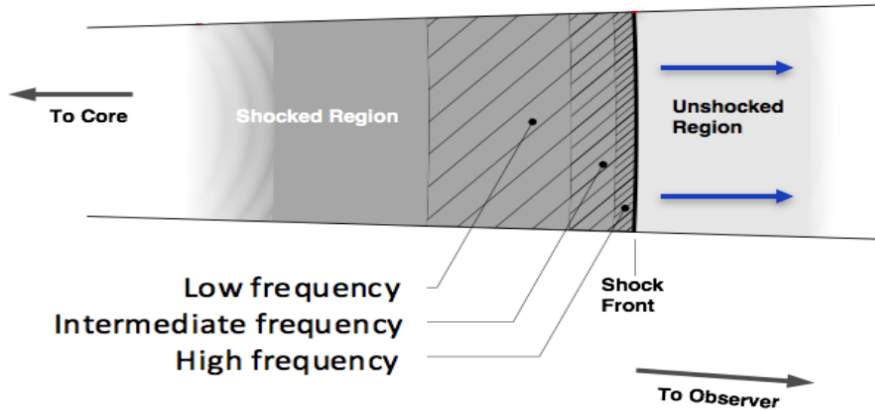


Figure 1.8: Sketch of the shock-in-jet model ([Marscher & Gear, 1985](#)). The volume of the emitting region increases with decreasing frequency. Picture taken from [Marscher \(2016\)](#).

the plasma which increases its density together with an adiabatic increase in its internal energy. It also enhances the component of the magnetic field parallel to the shock front. In addition, the shock may accelerate relativistic particles to high energies through the diffusive shock acceleration mechanism ([Blandford & Eichler, 1987](#)) which involves successive crossing of the shock front by the particles. This acceleration is most efficient if the direction of the magnetic field is perpendicular to the shock front.

The particles accelerated at the shock front suffer energy losses in the form of synchrotron and IC radiations. The highest energy particles emit radiation within a thin region behind the shock front. The thickness of the emitting region increases with the decrease in the frequency ([Marscher & Gear, 1985](#)). This frequency stratification, Figure 1.8, explains very nicely the observational features of the multiwavelength light curves of blazars. Since the high energy emission is emitted from a thin region the timescale of variability is much shorter and the variability amplitude is much larger at higher frequencies.

1.5.2 Turbulent Jet Models

Smaller amplitude and shorter timescale variations in blazar light curves can be explained by the turbulent jet models. It has been observed that the linear polarisation in blazars is significantly lesser than that expected from the typical synchrotron emission. This indicates that the magnetic field within the relativistic jet consists of randomly oriented components. It provides evidence for the

1. INTRODUCTION

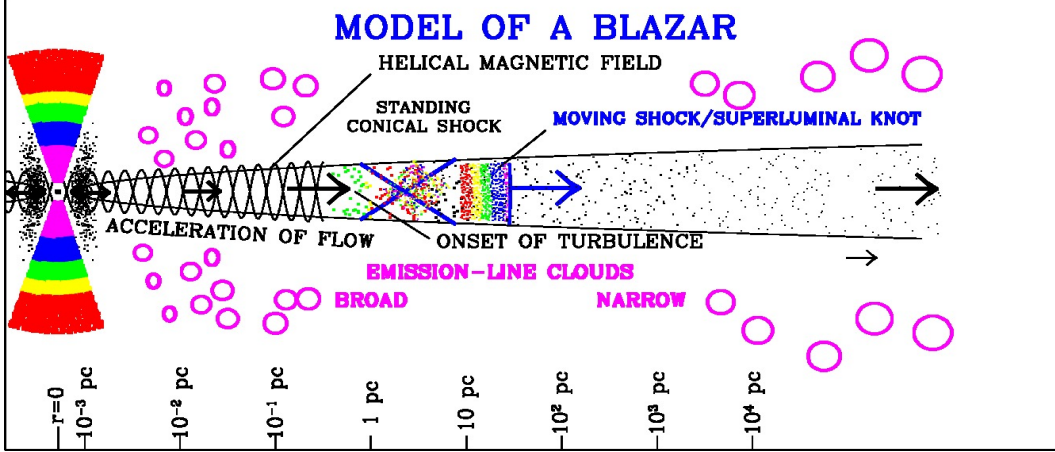


Figure 1.9: Sketch of physical features of a blazar. Taken from <https://www.bu.edu/blazars/VLBaproject.html>

fact that the plasma inside relativistic jets is hydro-magnetically turbulent. When the relativistic turbulence in plasma crosses a standing shock within the jet, Figure 1.9, the shock compresses the plasma and accelerates the particles to high energies (Marscher, 2014). These high energy particles cool down by emitting radiations and hence produce smaller amplitude variations. In another scenario, the turbulence in plasma moving at relativistic speed produce fluctuations that are responsible for the shorter timescale variability (e.g. Calafut & Wiita, 2015; Pollack et al., 2016).

1.5.3 Geometric Models

Blazar variability can also be explained by the models that assume bending or helical jets geometry. Variations in the viewing angle of the emitting regions within jets produce flux variations, quasi-periodic variations, or flares, in the blazar LCs due to changes in the Doppler beaming factor, Equations 1.5 and 1.6 (e.g., Camenzind & Krockenberger, 1992; Villata & Raiteri, 1999; Raiteri et al., 2017). Such helical jet morphologies or bendings are often seen in radio VLBI observations (e.g. Lister et al., 2013) and are thought to be due to the presence of binary black hole systems (BBHSs) at the center (Begelman et al., 1980). A very good example of blazars having BBHS at its center is OJ 287, whose well observed optical quasi-periodicities were explained using the helical jet model by Valtonen & Pihajoki (2013).

1.5.4 Models for Rapid Variability

The TeV fluxes of blazars PKS 2155–304 and Mrk 501 were found to be variable on timescales of 3–5 min ([Aharonian et al., 2007c](#); [Albert et al., 2007](#)). Such rapid variations imply that the γ –ray emitting region is very compact. The fact that the TeV photons will escape out such a compact region without being absorbed through the pair creation process indicates that the emitting region must have the bulk Lorentz factor $\Gamma \gtrsim 50$ (e.g. [Gopal-Krishna et al., 2006](#); [Begelman et al., 2008](#)). But, the jets of these blazars have been studied on sub-pc scales and found to move with $\Gamma \lesssim 10$ (e.g. [Piner & Edwards, 2004](#); [Giroletti et al., 2004](#)). This apparent contradiction suggests that there are small emitting regions within the larger jet that are moving much faster than the jet. Based on this fact two models, ‘needle’ model and ‘jets-in-a-jet’ model, have been proposed to explain such rapid variations in blazars. These two models are discussed below:

1.5.4.1 Needle Model

The ‘needle’ model, proposed by [Ghisellini & Tavecchio \(2008\)](#), assumes that the variable TeV flux is produced by a small region within the jet (a ‘needle’) that is moving with a much larger bulk Lorentz factor ($\Gamma = 50$) than that of the surrounding plasma ($\Gamma_j = 15$). The ‘needle’ moves in a dense radiation field of the rest of the jet due to which its inverse Compton flux is strongly enhanced. The episodes of rapid TeV variability are produced by ‘needles’ that are oriented at different angles and occasionally pointing towards the observer. If there is no evidence of simultaneous UV – X-ray fast flux variability then the ‘needle’ model is preferred for explaining the rapid TeV flux variations (“orphan TeV flares”).

1.5.4.2 Jets-in-a-Jet Model

The ‘jets-in-a-jet’ model, given by [Giannios et al. \(2009\)](#), proposed that the TeV emission is produced from the compact regions moving relativistically within a jet of bulk Lorentz factor $\Gamma_j \sim 10$. The model postulated that if a fraction of the jet luminosity is dissipated through magnetic reconnection, then the plasma blob relativistically leaving the reconnection sites emits the TeV flares through the synchrotron-self-Compton emission, Figure 1.10. The magnetic reconnection is triggered either due to current-driven instabilities in the jet or due to polarity

1. INTRODUCTION

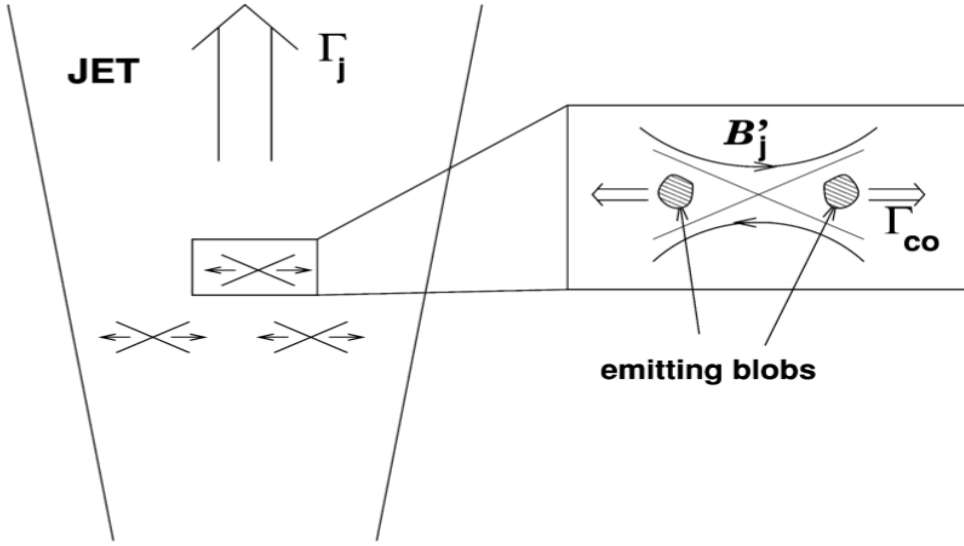


Figure 1.10: Sketch of the geometry of ‘jets-in-a-jet’ model. Figure courtesy: [Giannios et al. \(2009\)](#).

inversions of the magnetic field that threads the black hole. The model predicts simultaneous soft X-ray flares.

1.6 Thesis Motivation

TeV blazars are a growing subclass of blazars. Since the first detection of TeV γ -rays, in 1992, from Mrk 421 by the Whipple Observatory ([Punch et al., 1992](#)), a number of investigations are carried out to explain the extreme nature of these blazars. During last decades the development of several γ -ray facilities and theoretical models allowed researchers to detect more TeV blazars and to explain many of their observational properties.

Despite great progress in our understanding of blazar physics, many problems still remain unsolved about their structure and emission processes. We still have very little information about their underlying physical process and their origin.

Using the present observing facilities it is very difficult to resolve the inner structure of the blazars as they are at very large distances. The flux variability studies play an important role in understanding their geometry and radiation mechanisms. The observed variability timescale provides an estimate of the size and other properties of the emitting region. At high energies (X-ray/ γ -ray), flux varies at very short timescales that implies that emission at these energies are coming from very

compact regions, close to the central engine. Thus variability timescales provide a hint of the size and mass of the central engine. Optical observations are important in understanding the blazar physics at sub-pc level.

The 3–79 keV energy band is relatively less explored part of EM spectrum for blazar study. This energy range is important for understanding the blazar physics as the low energy and high energy components of TeV HBLs intersect in this band. The *NuSTAR* satellite, due to its unprecedented sensitivity in hard X-ray (3–79 keV) band, provides us the opportunity to study the nature and emission processes of TeV blazars at this energy range. We studied the hard X-ray IDV properties of TeV blazars observed with the *NuSTAR*. We also searched for the spectral changes in these blazars. The detection of TeV γ -rays from these blazars suggests that the electrons are accelerated to ultra-relativistic energies. To understand the acceleration mechanism and the particle distribution in TeV blazars we investigated the nature of their hard X-ray spectra.

The TeV blazars are less investigated at optical wavelengths. We performed their optical IDV and STV/LTV study to understand their behavior at optical frequencies. This allows us to compare the nature of TeV blazars at hard X-ray and optical frequencies.

1.7 Thesis Structure

The thesis is organized as follows:

- **Chapter 1** includes a brief description of blazars, their classifications, emission mechanisms, and several variability models.
- **Chapter 2** gives an overview of the multiwavelength observations and their data analysis processes.
- **Chapter 3** consists of the results of hard X-ray flux and spectral variability study of TeV blazars using the *NuSTAR* satellite.
- **Chapter 4** reports the results of optical flux and spectral variability study of TeV blazars.
- **Chapter 5** presents the summary, conclusions and future plans.

Chapter 2

Multiwavelength Observations and Data Reduction

In this thesis, we have performed multiwavelength studies of TeV (Tera-electron Volt) blazars to better understand their geometry and the emission mechanisms. For this, we have used X-ray observations, obtained from the *Nuclear Spectroscopic Telescope Array (NuSTAR)* satellite, and the optical photometric observations, obtained from the two ground-based telescopes. This chapter is mainly divided into two parts. Section 2.1 gives an overview of the *NuSTAR* observatory, its optics and instruments, and also describes *NuSTAR* data analysis process. Section 2.2 consists of the details of the observing sites, telescopes, detectors and filters used for optical observations. The steps of optical photometric data processing are also described in section 2.2.

2.1 X-ray Observations

The Earth's atmosphere is opaque to X-rays, so the X-ray observations must be carried out using balloons, rockets, and satellites above the atmosphere. In this thesis, we have used X-ray data which were taken with the *NuSTAR* satellite. *NuSTAR* provides an unprecedented sensitivity in the less explored energy range 3–79 keV. The *NuSTAR* satellite and its data reduction process are discussed in the following subsections.

2. MULTIWAVELENGTH OBSERVATIONS AND DATA REDUCTION

2.1.1 The Nuclear Spectroscopic Telescope Array (*NuSTAR*)

NuSTAR, a NASA's Small Explorer mission, is the first astronomical telescope in space that focuses hard X-rays (3–79 keV). *NuSTAR* was launched on June 13, 2012 into a near-circular orbit at an altitude of ~ 600 km and 6° of inclination. The *NuSTAR* observatory, shown in Figure 2.1, consists of two co-aligned hard X-ray telescopes that focus onto two independent focal plane detectors. The optics and focal plane benches are separated by a deployable mast to achieve a 10.14-meter focal length. The stiffness of the mast is not sufficient to maintain the required relative alignment of the two benches, hence *NuSTAR* uses an aspect/metrology system consisting of a star camera mounted on the optics bench and two laser metrology units. The translation, tip, tilt, and clocking between the benches, measured by the metrology system, is used to reconstruct an accurate image of the celestial X-ray sources. A detailed description of the *NuSTAR* mission can be found in [Harrison et al. \(2013\)](#).

2.1.1.1 *NuSTAR* Optics

NuSTAR has two optics modules, optics module A (OMA) and optics module B (OMB), each containing 133 nested grazing incidence mirror shells in a conical approximation to a Wolter-I geometry. The shells are coated with depth-graded multilayer structures which increase the grazing angle, resulting in higher reflectivity and larger effective collecting area at energies above ~ 15 keV, Figure 2.2. The coating material for inner 89 shells is Pt/C while the outer 44 shells are coated with W/Si. The optics dominates the angular resolution of the *NuSTAR* observatory, which is $18''$ FWHM, with a half power diameter (HPD) of $58''$.

2.1.1.2 *NuSTAR* Detectors

The two *NuSTAR* optics modules have their own focal plane modules, known as focal plane module A (FPMA) and focal plane module B (FPMB). Each FPM, see Figure 2.3, is composed of four 2 mm thick CdZnTe (CZT) pixel detectors, each having 32×32 pixels of 0.6 mm pixel size and is surrounded by a CsI anti-coincidence shield which reduces the background above 10 keV. The field of view (FoV) of each FPM is $12' \times 12'$ and it provides a good energy resolution of 400 eV at 10 keV and 900 eV at 60 keV. No pile-up occurs in the detectors for the source flux upto $\sim 10^5$ counts s^{-1} pixel $^{-1}$.

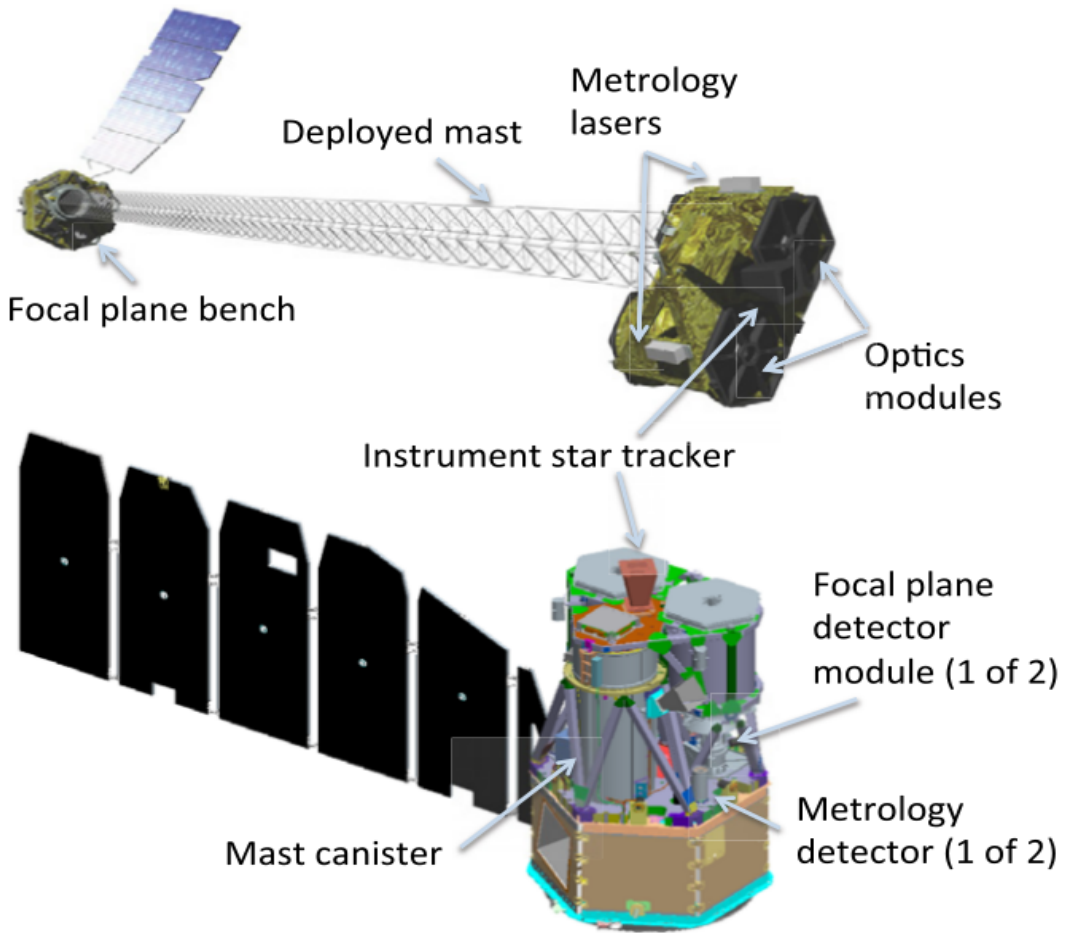


Figure 2.1: The *NuSTAR* observatory in the deployed (top) and stowed (bottom) configurations. Figure courtesy: [Harrison et al. \(2013\)](#).

2.1.2 *NuSTAR* Data Analysis

The primary archive for *NuSTAR* data, data analysis software and calibration files is the High Energy Astrophysics Science Archive Research Center (HEASARC)¹. All the *NuSTAR* observations of TeV blazars can be downloaded from the publicly available HEASARC Data Archive².

The *NuSTAR* data analysis is performed with the latest version of the *NuSTAR* Data Analysis Software (NuSTARDAS) which is officially integrated in the HEA-Soft software package, using the latest calibration files. The input data to the NuSTARDAS software package is the level 1 telemetry data in the Flexible Image Transport System (FITS) format and the output are the high-level scientific

¹<https://heasarc.gsfc.nasa.gov/>

²<https://heasarc.gsfc.nasa.gov/cgi-bin/W3Browse/w3browse.pl>

2. MULTIWAVELENGTH OBSERVATIONS AND DATA REDUCTION

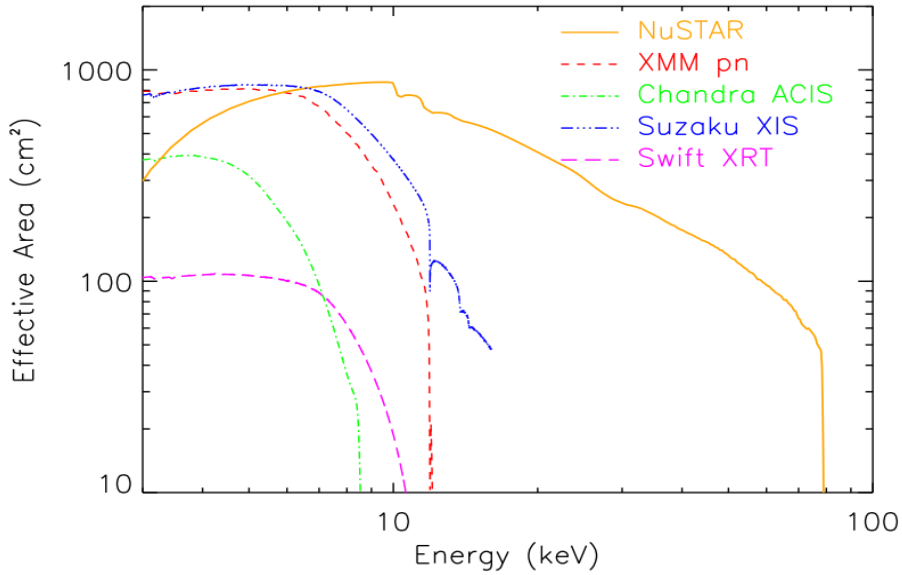


Figure 2.2: Comparison of effective area of *NuSTAR* with that of other focusing telescopes (Figure taken from [Harrison et al., 2013](#)). *NuSTAR* extends energy coverage upto 79 keV.

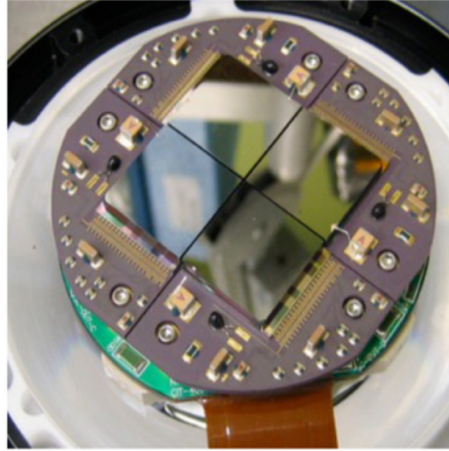


Figure 2.3: A photograph of the *NuSTAR* FPM. Picture courtesy: [Harrison et al. \(2013\)](#).

products. The NuSTARDAS data processing is performed in three distinct stages, which are

1. **Data Calibration** : processing of level 1 telemetry data to produce level 1a calibrated event files.
2. **Data Screening** : filtering the calibrated event files by applying screening criteria on specified orbital/instrumental parameters to produce level 2 calibrated and cleaned event files.

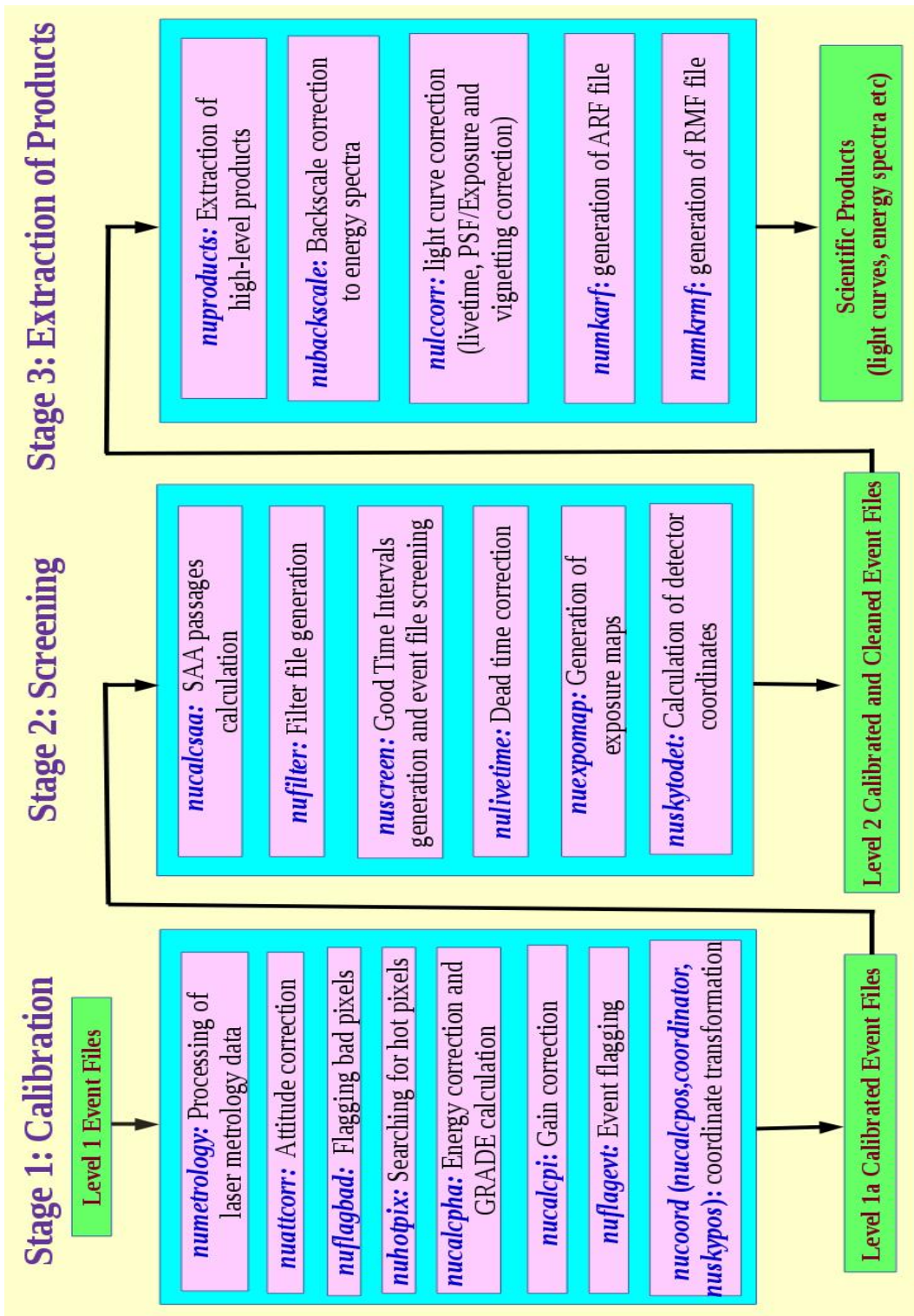


Figure 2.4: The three stages of *NuSTAR* data processing. The software modules used in each stage are also listed.

2. MULTIWAVELENGTH OBSERVATIONS AND DATA REDUCTION

3. **Extraction of Products:** high-level scientific products (light curves, energy spectra, Ancillary Response Files (ARFs), Redistribution Matrix Files (RMFs)) are extracted from the calibrated and cleaned event files.

Figure 2.4 illustrates these three processing stages with the software modules used in each stage. The NuSTAR-DAS package includes two pipeline scripts, *nupipeline* and *nuproducts*, to automatically process the data. The *nupipeline* script can be used to automatically run all the three stages, but it is recommended to use it to run stage 1 & 2 only. Stage 3 should be run separately using the *nuproducts* script to extract scientific products.

2.2 Optical Observations

The optical photometric observations of the TeV blazars were carried out during 2016–2018 in Johnson-Cousins *BVRI* filters using two optical telescopes at ARIES in India. Since the response of the instrument is maximum in *R* band filter, we continuously monitored TeV HBLs in *R* filter for a duration of 4 hours or more to search for intraday variability. We also performed quasi-simultaneous observations of a couple of TeV HBLs alternatively in *V* and *R* filters to get their color information. In addition, we took one set of data points in *BVRI* filters for all TeV HBLs to study day-to-day variations in their brightness.

The basic parameters of the telescopes and the instruments used for observations are given in Table 2.1. The effective wavelength and the bandwidth of the filters are given in Table 2.2. The telescopes, instruments and the optical photometric data analysis process are discussed in details in the following subsections.

2.2.1 Telescopes

2.2.1.1 1.3 meter Devasthal Fast Optical Telescope

The 1.3 m Devasthal Fast Optical Telescope (DFOT), shown in Figure 2.5a, was fabricated in 2010 by DFM Engineering Inc. USA at Devasthal, Nainital (longitude: $79^{\circ}41'04''$ E; latitude: $29^{\circ}21'40''$ N; altitude: 2420 m) and is operated by ARIES, Nainital. The telescope is a modern Ritchey-Chretien (RC) reflecting telescope which delivers a fast beam ($f/4$) at the Cassegrain focus. The instruments

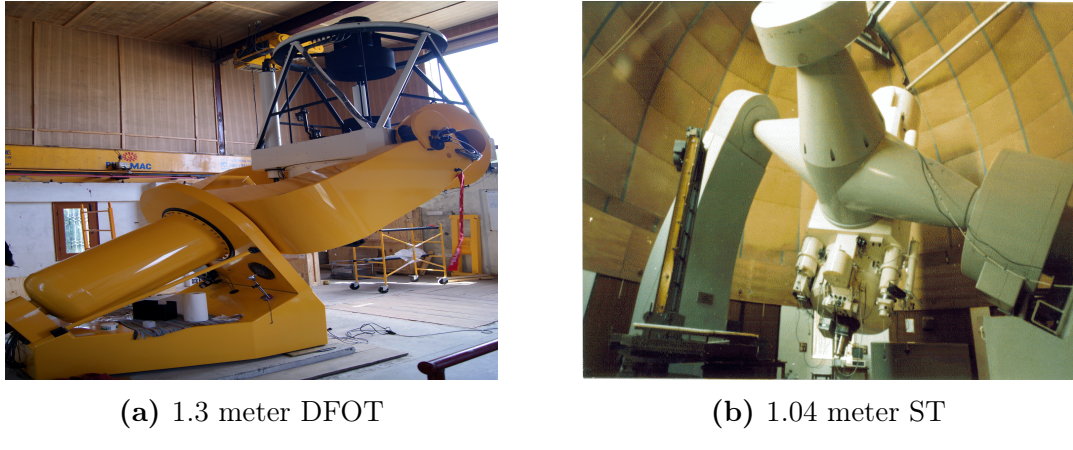


Figure 2.5: The telescopes used for observations.

used for monitoring of TeV blazars with 1.3 m DFOT telescope are $2\text{K} \times 2\text{K}$ Andor CCD and 512×512 Andor CCD. Both the instruments were thermoelectrically cooled down to -90°C for observations.

2.2.1.2 1.04 meter Sampurnanand Telescope

1.04 meter ($f/13$) Sampurnanand Telescope (ST), installed in 1972 by Carl Zeiss, Germany, is located at ARIES, Manora Peak, Nainital, India (longitude: $79^\circ 27' 26''$ E; latitude: $29^\circ 21' 39''$ N; altitude: 1920 m). It is a RC Cassegrain reflecting telescope having an equatorial mount, see Figure 2.5b. The instruments available at present for use with the telescope are $1\text{K} \times 1\text{K}$ Tek CCD, 1340×1300 PyLoN CCD and the imaging polarimeter. The cooling of the CCD cameras is done using the liquid nitrogen, LN2. Our photometric observations were carried out using the $1\text{K} \times 1\text{K}$ Tek CCD and 1340×1300 PyLoN CCD.

Table 2.1: Details of telescopes and instruments used.

Telescope	1.3 m DFOT: ($f/4$) RC Cassegrain		1.04 m ST: ($f/13$) RC Cassegrain	
CCD Model	Andor 2K CCD	Andor 512 CCD	Tektronics 1K CCD	PyLoN CCD
Chip Size (pixels)	2048×2048	512×512	1024×1024	1340×1300
Pixel Size (μm)	13.5×13.5	16×16	24×24	20×20
Scale (arcsec/pixel)	0.535	0.64	0.37	0.305
Field (arcmin^2)	18×18	5.5×5.5	6×6	6.8×6.6
Gain (e^-/ADU)	2.0	1.4	11.98	4.0
Read-out Noise ($e^- \text{ rms}$)	7.0	6.1	6.9	6.4
Typical Seeing (arcsec)	1.2–2.0	1.3–3.2	1.4–2.6	1.2–2.1

2. MULTIWAVELENGTH OBSERVATIONS AND DATA REDUCTION

Table 2.2: The broadband filters used for observations. λ_{eff} is the effective wavelength.

Filter	λ_{eff} (Å)	Bandwidth(Å)
B	4400	980
V	5500	890
R	6500	2200
I	8000	2400

2.2.2 Optical Photometric Data Analysis

The quality of the raw CCD images obtained directly from the ground-based optical telescopes is affected by the atmosphere, telescope optics, the detector, and its electronics. So the raw CCD data need to be analyzed properly to extract good quality scientific products. Figure 2.6 illustrates the three basic stages of optical photometric data analysis, which are discussed below:

2.2.2.1 Pre-Processing

The pre-processing or cleaning of raw data involves the removal of effects caused by the detector. The image pre-processing is performed in the following steps, see Figure 2.7, using the standard routines of the Image Reduction and Analysis Facility (IRAF³).

(a) Bias Subtraction

A bias frame, shown in Figure 2.7, is acquired in zero exposure time with closed CCD shutter. It, thus, contains information about the DC offset voltage (bias voltage) added by the CCD amplifier for proper digitization of the data. To remove this effect several bias frames, taken at regular intervals, are median combined to make a master bias, which is subtracted from all the CCD image frames.

(b) Flat-Fielding

The sensitivity of each pixel within the CCD is not constant. There may be two main reasons for this. First, the non-uniform transmission of light by the

³IRAF is distributed by the National Optical Astronomy Observatory, which is operated by the Association of Universities for Research in Astronomy (AURA) under a cooperative agreement with the National Science Foundation.

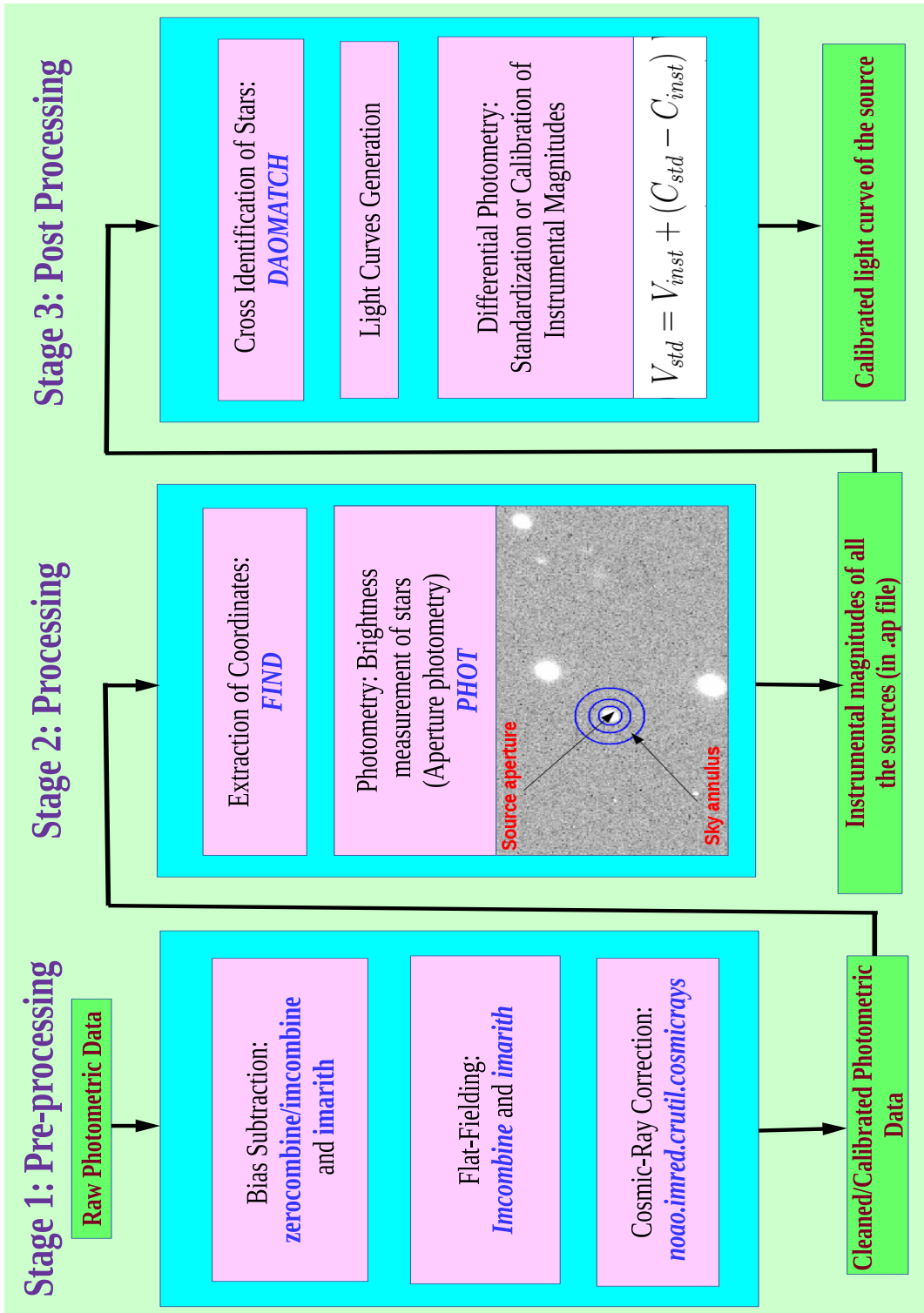


Figure 2.6: Stages of the optical photometric data analysis.

2. MULTIWAVELENGTH OBSERVATIONS AND DATA REDUCTION

telescope optics across the entire field of view, which is either due to vignetting (darkening of the image corners) or due to the presence of dust on the CCD glass cover or on the CCD itself (appears as dark "doughnuts" on the image), see Figure 2.7. Second, the quantum efficiency (QE) of each CCD pixel is different from its neighbors, which also causes variation in sensitivity. To remove the effect of non-uniform sensitivity of the individual CCD pixels, three or more flat field frames are obtained by taking CCD exposures of the twilight sky, known as ‘sky flats’, in each filter. The bias subtracted flat field frames are, then, median combined to make a master flat which is divided by its mean response to generate the normalized master flat in each filter. Finally, the bias subtracted source image frames in each filter are divided by the corresponding normalized master flat to correct for the non-uniform sensitivity of the CCD pixels.

(c) Cosmic-Rays Removal

Cosmic rays are highly energetic particles and are appeared as bright specks in the image frames, in addition to the stars. The effect of cosmic rays is removed using the fact that their intensity profile (sharply rising and falling) is different from those of stars (Gaussian-like profile).

(d) Trimming

The final step of image pre-processing is trimming. The CCD pixels at the edges of the image frame may behave abnormally. Therefore, the frames need to be trimmed off from all edges to remove the effect of those bad pixels.

2.2.2.2 Processing

After cleaning of the raw data, the detector effects have been removed from the CCD images. Now in the second stage, the cleaned images are processed using the Dominion Astronomical Observatory Photometry (DAOPHOT II; [Stetson \(1987, 1992\)](#)) software to get the coordinates and the instrumental magnitudes of the stellar objects in each CCD image frame.

Before running the DAOPHOT II software, a priori knowledge of the following information is required (generally in a file called ‘DAOPHOT.OPT’).

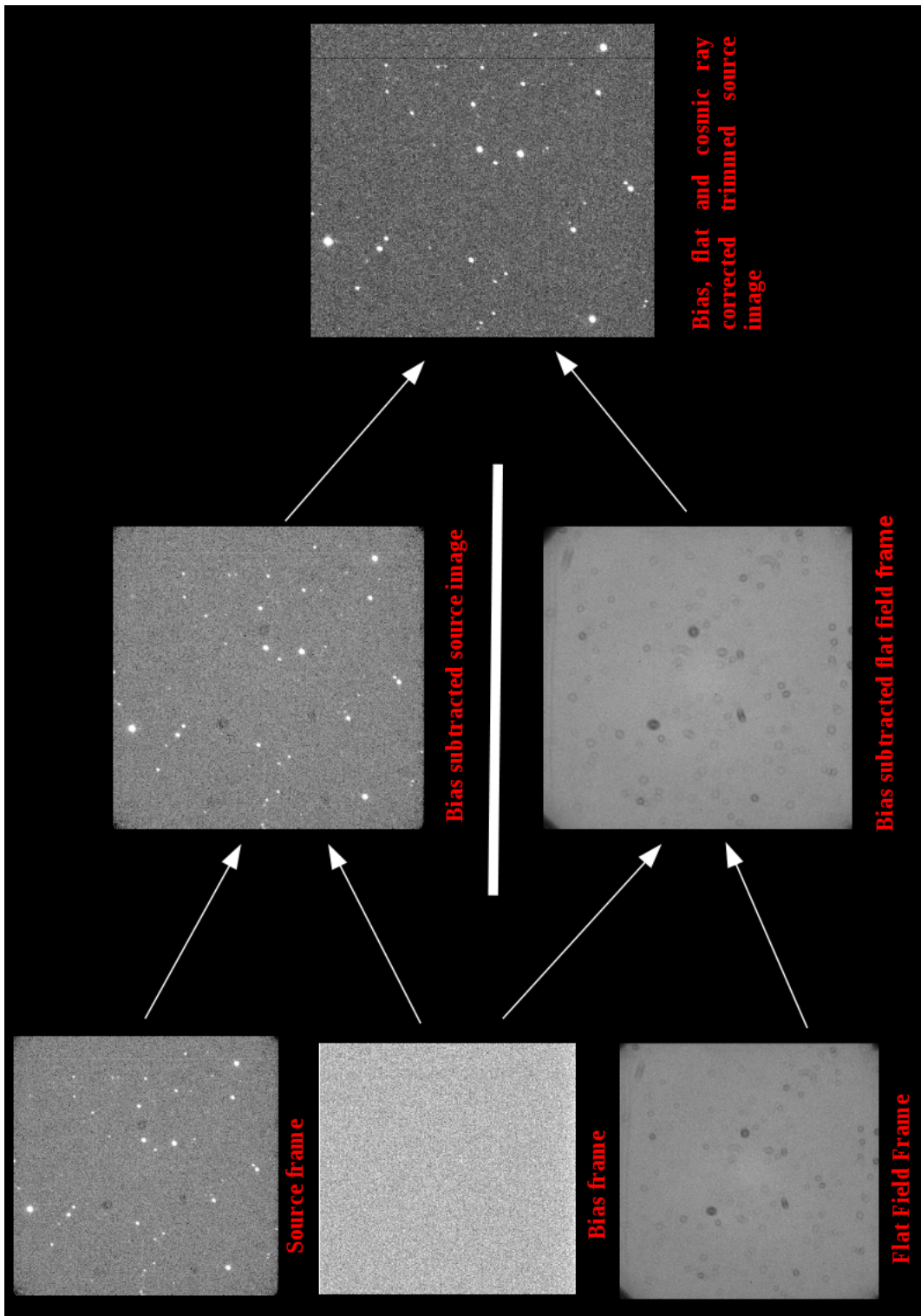


Figure 2.7: Steps of pre-processing or cleaning of raw data.

2. MULTIWAVELENGTH OBSERVATIONS AND DATA REDUCTION

- an average value of the full-width at half-maximum (FWHM) of the stellar objects in the frame.
- the gain (GA) of the CCD (in electrons/ADU).
- the readout noise (RE) in a single exposure (in ADU).
- the maximum brightness level (HI), in pixels, above which the detector becomes non-linear or saturates.
- the threshold (TH), in σ , that is the significance level above which the brightness enhancement is considered as real.
- the fitting radius (FI), in pixels, for photometry.

(a) Extraction of Coordinates

FIND routine of DAOPHOT II is used to determine the positions of the star-like objects above the user-defined detection level (TH), rejecting bad pixels, rows, and columns in each image frame. This routine goes through the image pixel by pixel to locate stars. At each pixel, it fits an analytic Gaussian profile, with user-defined FWHM, to the brightness values in a surrounding subarray of pixels. The center of a star is located where the central height of the best-fitting Gaussian profile attains a large, positive value. The coordinates (X and Y positions) of the stars in each image frame are listed in a ‘.coo’ (coordinate) file.

(b) Photometry: Brightness measurement of stars

Photometry refers to the quantitative measurement of the brightness of the objects located in the image. The two methods of CCD photometry are: ‘Aperture Photometry’ and ‘Profile Fitting Photometry’. Aperture Photometry is preferred for bright sources and less-crowded field, while for faint sources and crowded field Profile Fitting Photometry is performed. Since the blazars studied in this thesis are bright objects and are located in less crowded fields, we have only performed the aperture photometry which is discussed below.

Aperture Photometry

In aperture photometry, the actual apparent brightness of an object in a frame is measured by defining a circular region, known as an aperture (see Figure 2.8),

centered on the object. The aperture photometry is performed using the **PHOT** routine of DAOPHOT II which allows the user to define up to twelve concentric apertures and one sky annulus (in a file named as ‘PHOTO.OPT’) to determine the brightness of the object by removing any possible contamination due to sky, nearby stars and galaxies, or pixel defects. The aperture size should be chosen carefully,

it has to be large enough to include the entire star image. We have used four different concentric aperture radii, i.e., $\sim 1 \times \text{FWHM}$, $2 \times \text{FWHM}$, $3 \times \text{FWHM}$, and $4 \times \text{FWHM}$ to perform the aperture photometry. The total counts (S) in each aperture contain a contribution from the source as well as from the underlying background sources within the aperture. So, the actual source counts are estimated as $I = S - n_{pix}\bar{B}$, where n_{pix} is the total number of pixels within the aperture and \bar{B} is the mean value of background, estimated from the sky annulus. Then, the instrumental magnitude (IM) of the source is calculated using the following equation:

$$IM = -2.5\log_{10}(I/t) + C, \quad (2.1)$$

where t is the exposure time of the image frame and C is an arbitrary zero-point, whose value is 25.0 magnitude (= 1 ADU) in DAOPHOT II.

The output of the **PHOT** routine is a ‘.ap’ (aperture photometry) file which includes the instrumental magnitudes and corresponding uncertainties for each aperture for all the objects in an image.

2.2.2.3 Post-Processing

The last stage of optical photometric data analysis involves the matching of stars between frames and generating the instrumental light curves (LCs) of the source and the comparison stars.

(a) Cross Identification of Stars

A star will not fall on the same pixel over the entire observing night, the shift in the position of the star in different frames with respect to a frame is estimated

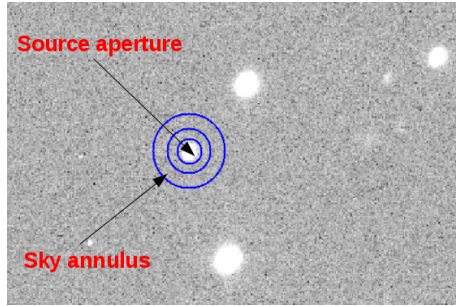


Figure 2.8: The source aperture and the sky annulus.

2. MULTIWAVELENGTH OBSERVATIONS AND DATA REDUCTION

using the **DAOMATCH** program. **DAOMATCH** accepts the ‘.ap’ files created by **PHOT** routine, cross identifies stars in different frames by using the matching triangles method and outputs a ‘.mch’ file for each filter containing the shifts between the frames. The method of matching triangles uses the fact that any translation, rotation, scale change, or flip will not change the basic *shape* (ratios of the sides) of a triangle, although of course, it will change the size and orientation. **DAOMATCH** extracts 30 brightest stars from each input file (frame n) and cross identifies them with the 30 brightest stars from the first ‘best’ frame (frame 1), yielding the coordinate transformation equations which are in the form

$$x(1) = A + C * x(n) + D * y(n) \quad (2.2)$$

$$y(1) = B + E * x(n) + F * y(n) \quad (2.3)$$

If both the frames were observed with the same telescope and the detector was not rotated, then

$C \approx F \approx 1$, and $D \approx E \approx 0$.

If they were observed with the same telescope and the detector was rotated, then $C \approx F$, $D \approx E$, and $C^2 + D^2 \approx 1$.

DAOMATCH fails if the two frames have less than 5 or 6 brightest stars in common.

(b) Light Curves Generation

Taking the shifts in X and Y positions from the ‘.mch’ file, the instrumental magnitudes of the source and the comparison stars in different frames are determined. The aperture size, for which the variance of the differential magnitude (the difference between instrumental magnitudes of two comparison stars) is minimum, is adopted for the instrumental magnitudes. In our case, we used the aperture of $2 \times \text{FWHM}$, as it provides the best S/N ratio. Finally, the instrumental LCs of the source and the comparison stars are generated using their instrumental magnitudes in each frame and the corresponding time of observation, extracted from the header of the frame.

The instrumental magnitudes are specific to the observing conditions (telescopes, instruments, atmosphere, etc.), that means, the instrumental magnitude of a star observed with a telescope at any time from any location will be different from the instrumental magnitude of the same star observed at the same time but with a different telescope from a different location. In order to make our observations

comparable to different telescopes, we need to convert instrumental magnitudes to standard magnitudes. This standardization or calibration is done using the differential photometry technique which is discussed below.

Differential Photometry

Differential photometry is the simplest technique for the measurement of variations in the brightness of the source with very high accuracy. In differential photometry, the brightness of the variable source is compared with the brightness of a non-variable star (comparison star) present in the same CCD frame. The comparison star should have the magnitude and color closer to that of the variable star. One more comparison star (check star), in the same frame, is also used to check the non-variability of the comparison star and to measure the accuracy of the observation. The differential LCs of the source is generated by subtracting the instrumental magnitude of the comparison star from the instrumental magnitude of the source.

The instrumental magnitude (V_{inst}) of the source is converted to its standard magnitude (V_{std}) by using the standard magnitude (C_{std}) of the comparison star taken from the Finding Charts for AGN⁴ by Landessternwarte Heidelberg-Königstuhl as:

$$V_{std} = V_{inst} + (C_{std} - C_{inst}) \quad (2.4)$$

where C_{inst} is the instrumental magnitude of the comparison star.

The uncertainty in V_{std} is estimated as

$$\sigma_{V_{std}} = \sqrt{(\sigma_{V_{inst}}^2 + \sigma_{C_{inst}}^2)} \quad (2.5)$$

⁴<https://www.lsw.uni-heidelberg.de/projects/extragalactic/charts/>

Chapter 3

X-ray Flux and Spectral Variability of TeV Blazars with *NuSTAR*

3.1 Introduction

The X-ray emissions from the TeV blazars correspond to the high energy-tail of their synchrotron component and hence are found to be highly variable (e.g. [Gaur et al., 2010](#), and references therein). The study of X-ray variations on IDV timescales is useful for understanding the underlying emission processes and for constraining different physical properties of the emitting regions. Also, flux variations are often accompanied by spectral changes. The X-ray spectrum of a TeV blazar typically hardens with increasing source brightness (e.g. [Brinkmann et al., 2003](#); [Ravasio et al., 2004](#)). The nature of the X-ray spectra of the TeV blazars has been investigated in several studies. In the *BeppoSAX*, spectral survey of BL Lacs the X-ray spectra of a sample of BL Lac objects were fitted well by either a single power-law (PL) or a broken power-law ([Beckmann et al., 2002](#)). In other recent studies, the X-ray spectra of TeV blazars were found to be curved and were better described by a log-parabola (LP) model (e.g. [Giommi et al., 2002](#); [Donato et al., 2005](#); [Tramacere et al., 2007](#); [Massaro et al., 2008](#)). Recently, [Wierzcholska & Wagner \(2016\)](#) reported that most of the X-ray spectra of TeV blazars are well fitted by the LP model.

¹Work presented in this chapter has been published in
(1) [Pandey et al. \(2017\)](#), ApJ, 841, 123
(2) [Pandey et al. \(2018\)](#), ApJ, 859, 49

3. X-RAY FLUX AND SPECTRAL VARIABILITY OF TEV BLAZARS WITH *NuSTAR*

In this chapter, we present our results of timing and spectral studies of *NuSTAR* observations of TeV blazars. *NuSTAR* is the first astronomical observatory that focuses X-rays in the interesting 3–79 keV energy band. This energy band is interesting because this band is near where the high-energy tail of the synchrotron component and the low-energy tail of the inverse Compton component of TeV HBLs intersect. At the time of writing, the total number of observed TeV blazars is 64² (HBLs=48, IBLs=8, LBLs=2, FSRQs=6). Out of these 64 TeV blazars *NuSTAR* has observed only 15 (HBLs = 11, IBLs = 2, FSRQs = 2). As most of the TeV blazars observed are HBL type, we decided to study the flux and spectral variability of those eleven TeV HBLs observed with *NuSTAR*.

The *NuSTAR* spectra of five TeV HBLs (1ES 0229+200, Mrk 421, Mrk 501, 1ES 1959+650, and PKS 2155–304) have been studied by other authors, and found to be fitted well by either the simple PL or the curved LP model. See [Bhatta et al. \(2018\)](#) for 1ES 0229+200 and 1ES 1959+650, see [Sinha et al. \(2015\)](#) and [Baloković et al. \(2016\)](#) for Mrk 421, [Furniss et al. \(2015\)](#) for Mrk 501, [Madejski et al. \(2016\)](#) for PKS 2155–304. In this work, we investigated the X-ray spectral shape of the remaining 6 TeV HBLs observed by *NuSTAR*: 1ES 0347–121, 1ES 0414+009, RGB J0710+591, 1ES 1101–232, 1ES 1218+304 and H 2356–309.

The structure of the chapter is as follows. The data selection criteria and the data processing are briefly described in Section 3.2. The techniques used to study the flux and spectral variations are discussed in Section 3.3. Section 3.4 presents our results. A detailed discussion and conclusions are given in Sections 3.5 and 3.6, respectively.

3.2 *NuSTAR* Data Selection and Processing

3.2.1 Data Selection Criteria

We have examined the hard X-ray emission of all the eleven TeV HBLs observed by *NuSTAR*, which gave us a new opportunity to study the temporal and spectral variability nature of these blazars in 3–79 keV energy range. The right ascension (RA), declination (Dec), and redshift of the TeV blazars observed with *NuSTAR* are listed in Table 3.1. We downloaded all the *NuSTAR* observations of these 11 TeV HBLs from the publicly available HEASARC Data archive³. To search

²<http://tevcat.uchicago.edu>

³<http://heasarc.gsfc.nasa.gov/docs/archive.html>

Table 3.1: RA, Dec and Redshift of the TeV Blazars.

Blazar Name	RA (α_{2000})	Dec (δ_{2000})	Redshift (z)
1ES 0229+200	02 ^h 32 ^m 53 ^s	+20°16'21"	0.140
1ES 0347–121	03 ^h 49 ^m 23 ^s	-11°58'38"	0.188
1ES 0414+009	04 ^h 16 ^m 53 ^s	+01°05'20"	0.287
RGB J0710+591	07 ^h 10 ^m 26 ^s	+59°09'00"	0.125
1ES 1101–232	11 ^h 03 ^m 36 ^s	-23°29'45"	0.186
Mrk 421	11 ^h 04 ^m 19 ^s	+38°11'41"	0.031
1ES 1218+304	12 ^h 21 ^m 26 ^s	+30°11'29"	0.182
Mrk 501	16 ^h 53 ^m 52 ^s	+39°45'37"	0.034
1ES 1959+650	19 ^h 59 ^m 60 ^s	+65°08'55"	0.480
PKS 2155–304	21 ^h 58 ^m 53 ^s	-30°13'18"	0.116
H 2356–309	23 ^h 56 ^m 09 ^s	-30°37'23"	0.165

for IDV, we only selected observations for which the good exposure times (those unaffected by periods of exceptionally high background, e.g. passage through the South Atlantic Anomaly (SAA), etc.) exceeded 5 ks. This minimum temporal constraint yielded a total of 46 observations for 11 TeV HBLs, which were made between 2012 July 7 and 2016 May 18; the good exposure times ranged from 5.76 to 57.51 ks. The observing log of the *NuSTAR* data for these eleven TeV HBLs is given in Table 3.2.

3.2.2 Data Reduction

The *NuSTAR* data for 11 TeV HBLs were processed using HEASOFT version 6.19 and the updated CALDB version 20161207. The calibrated, cleaned and screened level 2 event files were generated using the standard *nupipeline* script. Each source LC and spectrum were then extracted, from a circular region centered at the source, using the *nuproducts* script. The background data for each source were extracted from another circular region, on the same detector module, that is close to the source but free from contamination by the source. The radii of the source and background regions for eleven TeV HBLs are listed in Table 3.3. Since both the *NuSTAR* detectors, FPMA and FPMB, are nearly identical, we summed their background-subtracted count rates and binned them in a 5-minute interval to extract the final LCs. The *rmf* and *arf* files were generated using the *numkrmf* and *numkarf* modules, respectively, of the *nuproducts* script.

3. X-RAY FLUX AND SPECTRAL VARIABILITY OF TEV BLAZARS WITH *NUSTAR*

Table 3.2: Observation log of *NuSTAR* data for TeV HBLs.

Blazar Name	Obs. Date yyyy-mm-dd	Start Time (UT) hh:mm:ss	Obs. ID	Total Elapsed Time (ks)	Good Exposure Time (ks)
1ES 0229+200	2013-10-02	00:06:07	60002047002	32.43	16.26
	2013-10-05	23:31:07	60002047004	38.24	20.29
	2013-10-10	23:11:07	60002047006	32.35	18.02
1ES 0347–121	2015-09-10	04:51:08	60101036002	61.27	32.93
1ES 0414+009	2015-11-25	17:01:08	60101035002	107.06	34.16
RGB J0710+591	2015-09-01	12:11:08	60101037004	47.84	26.48
1ES 1101–232	2016-01-12	21:01:08	60101033002	101.87	50.79
Mrk 421	2012-07-07	01:56:07	10002015001	78.45	42.03
	2012-07-08	01:46:07	10002016001	44.16	24.89
	2013-01-02	18:41:07	60002023002	14.51	9.15
	2013-01-10	01:16:07	60002023004	43.44	22.63
	2013-01-15	00:56:07	60002023006	44.14	24.18
	2013-01-20	02:21:07	60002023008	44.14	24.97
	2013-02-06	00:16:07	60002023010	42.09	19.31
	2013-02-12	00:16:07	60002023012	35.39	14.78
	2013-02-16	23:36:07	60002023014	37.14	17.36
	2013-03-04	23:06:07	60002023016	34.99	17.25
	2013-03-11	23:01:07	60002023018	31.88	17.47
	2013-03-17	00:11:07	60002023020	35.08	16.56
	2013-04-02	17:16:07	60002023022	54.19	24.77
	2013-04-10	21:26:07	60002023024	12.88	5.76
	2013-04-11	01:01:07	60002023025	117.29	57.51
	2013-04-12	20:36:07	60002023027	18.69	7.63
	2013-04-13	21:36:07	60002023029	32.57	16.51
	2013-04-14	21:41:07	60002023031	32.58	15.61
	2013-04-15	22:01:07	60002023033	32.56	17.28
	2013-04-16	22:21:07	60002023035	38.11	20.28
	2013-04-18	00:16:07	60002023037	31.09	17.80
	2013-04-19	00:31:07	60002023039	26.74	15.96
1ES 1218+304	2015-11-23	01:06:08	60101034002	96.14	49.55
Mrk 501	2013-04-13	02:31:07	60002024002	35.76	18.28
	2013-05-08	20:01:07	60002024004	55.20	26.14
	2013-07-12	21:31:07	60002024006	20.90	10.86
	2013-07-13	20:16:07	60002024008	20.71	10.34
1ES 1959+650	2014-09-17	02:36:07	60002055002	35.04	19.61
	2014-09-22	02:06:07	60002055004	32.80	20.34
PKS 2155–304	2012-07-08	14:36:07	10002010001	71.57	33.84
	2013-04-23	19:46:07	60002022002	90.11	45.06
	2013-07-16	22:51:07	60002022004	26.21	13.86
	2013-08-02	21:51:07	60002022006	29.93	10.97
	2013-08-08	22:01:07	60002022008	36.54	13.50
	2013-08-14	21:51:07	60002022010	31.51	10.53
	2013-08-26	19:51:07	60002022012	24.33	11.36
	2013-09-04	21:56:07	60002022014	30.49	12.28
	2013-09-28	22:56:07	60002022016	25.66	11.53
H 2356–309	2016-05-18	16:31:08	60160840002	38.17	21.90

Table 3.3: Source and background region sizes

Blazar Name	Source radius	Background radius
1ES 0229+200	20"	30"
1ES 0347–121	30"	30"
1ES 0414+009	30"	30"
RGB J0710+591	30"	30"
1ES 1101–232	40"	40"
Mrk 421	30"	70"
1ES 1218+304	30"	30"
Mrk 501	40"	40"
1ES 1959+650	30"	30"
PKS 2155–304	30"	30"
H 2356–309	30"	30"

3.3 Analysis Techniques

3.3.1 Excess Variance

Blazars exhibit rapid and strong flux variations at different timescales over the complete electromagnetic spectrum. To quantify the strength of this variability, excess variance is often used. Excess variance measures the intrinsic variance of the source by subtracting the variance arising from measurement errors from the total variance of the observed LC. If a LC having N measured flux values, x_i , contains corresponding uncertainties $\sigma_{err,i}$ arising from measurement errors, then the excess variance is computed (e.g., [Vaughan et al. \(2003\)](#)) as

$$\sigma_{XS}^2 = S^2 - \overline{\sigma_{err}^2}, \quad (3.1)$$

where $\overline{\sigma_{err}^2}$ is the mean square error, given by,

$$\overline{\sigma_{err}^2} = \frac{1}{N} \sum_{i=1}^N \sigma_{err,i}^2. \quad (3.2)$$

The quantity S^2 , the sample variance of the LC, is given by

$$S^2 = \frac{1}{N-1} \sum_{i=1}^N (x_i - \bar{x})^2, \quad (3.3)$$

3. X-RAY FLUX AND SPECTRAL VARIABILITY OF TEV BLAZARS WITH *NUSTAR*

where \bar{x} is the arithmetic mean of x_i .

The fractional rms variability amplitude, F_{var} , is calculated as

$$F_{var} = \sqrt{\frac{S^2 - \sigma_{err}^2}{\bar{x}^2}}. \quad (3.4)$$

The uncertainty on F_{var} is given by (e.g., [Vaughan et al. \(2003\)](#))

$$\text{err}(F_{var}) = \sqrt{\left(\sqrt{\frac{1}{2N} \frac{\sigma_{err}^2}{\bar{x}^2 F_{var}}}\right)^2 + \left(\sqrt{\frac{\sigma_{err}^2}{N} \frac{1}{\bar{x}}}\right)^2}. \quad (3.5)$$

3.3.2 Discrete Correlation Function

We used the Discrete Correlation Function (DCF) to examine the correlation between the two light curves. DCF was introduced by [Edelson & Krolik \(1988\)](#) and later generalized by [Hufnagel & Bregman \(1992\)](#) to include a better error estimate. The advantage of using a DCF over a classical correlation function (CCF) is that it can also be used for unevenly sampled data sets, which is generally the case in astronomical observations, without interpolating between data. The DCF is calculated in the following steps. First, we compute the set of unbinned discrete correlations (UDCF) for two unevenly sampled data sets x and y (e.g. [Gaur et al. \(2015b\)](#)) as

$$UDCF_{ij} = \frac{(x_i - \bar{x})(y_j - \bar{y})}{\sqrt{\sigma_x^2 \sigma_y^2}}, \quad (3.6)$$

where x_i and y_j are the individual data points, \bar{x} and \bar{y} are their means, and σ_x^2 and σ_y^2 are their variances, respectively. A pairwise lag $\Delta t_{ij} = t_j - t_i$, associated with each UDCF, is also calculated. After calculating the UDCF, time binning is done. The bin size is not automatically defined by the method, so one must try several values for this parameter. If the bin size is too large, information may be lost, while too small bin size may lead to spurious correlations.

After binning, the DCF is calculated by taking the average of the UDCF values (M in number) for which $\tau - \Delta\tau/2 \leq \Delta t_{ij} < \tau + \Delta\tau/2$ as,

$$DCF(\tau) = \frac{1}{M} \sum UDCF_{ij}. \quad (3.7)$$

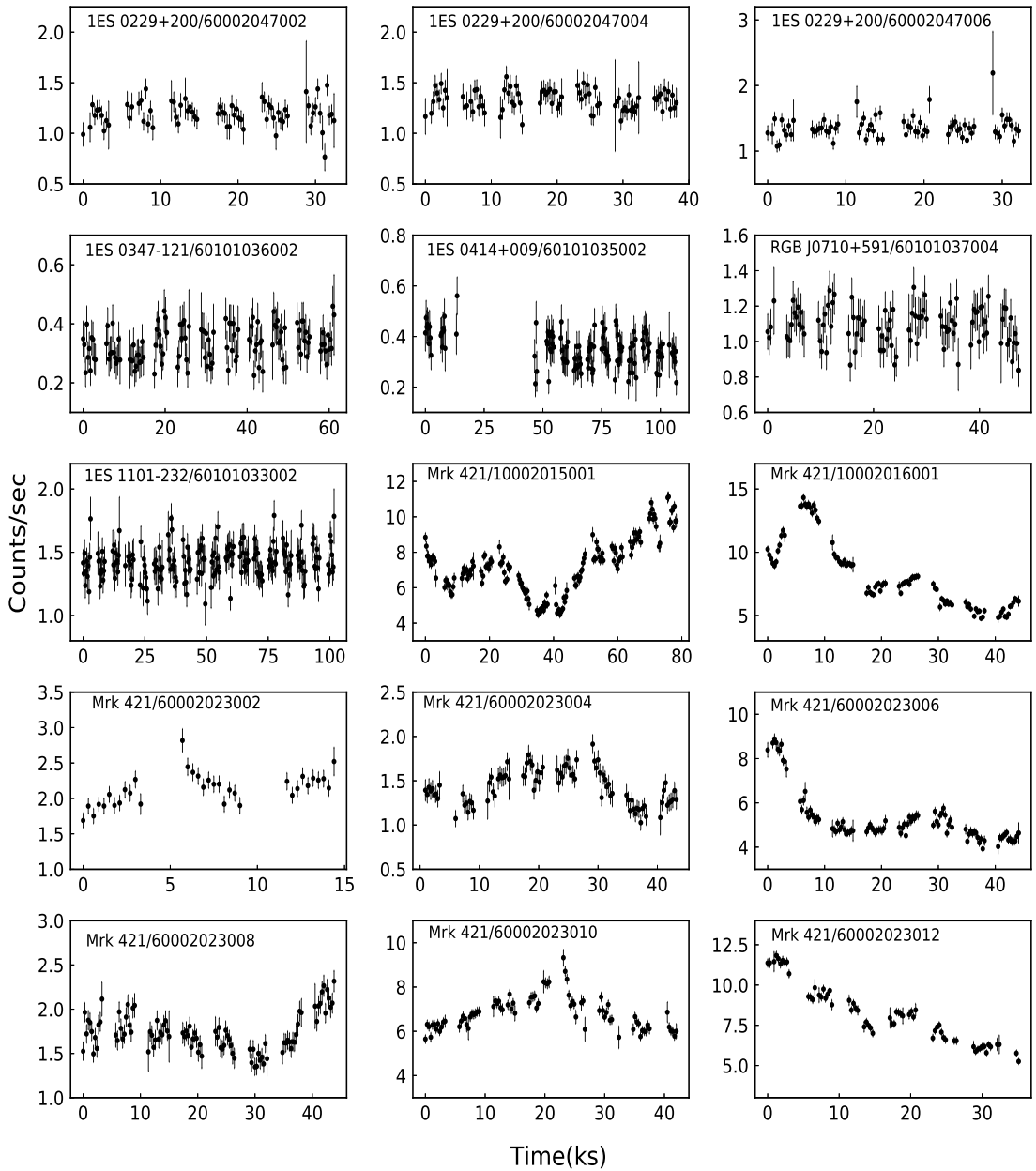


Figure 3.1a: *NuSTAR* light curves of the TeV HBLs 1ES 0229+200, 1ES 0347–121, 1ES 0414+009, RGB J0710+591, 1ES 1101–232 and Mrk 421. The name of the HBL and the observation ID are given in each plot.

3. X-RAY FLUX AND SPECTRAL VARIABILITY OF TEV BLAZARS WITH *NUSTAR*

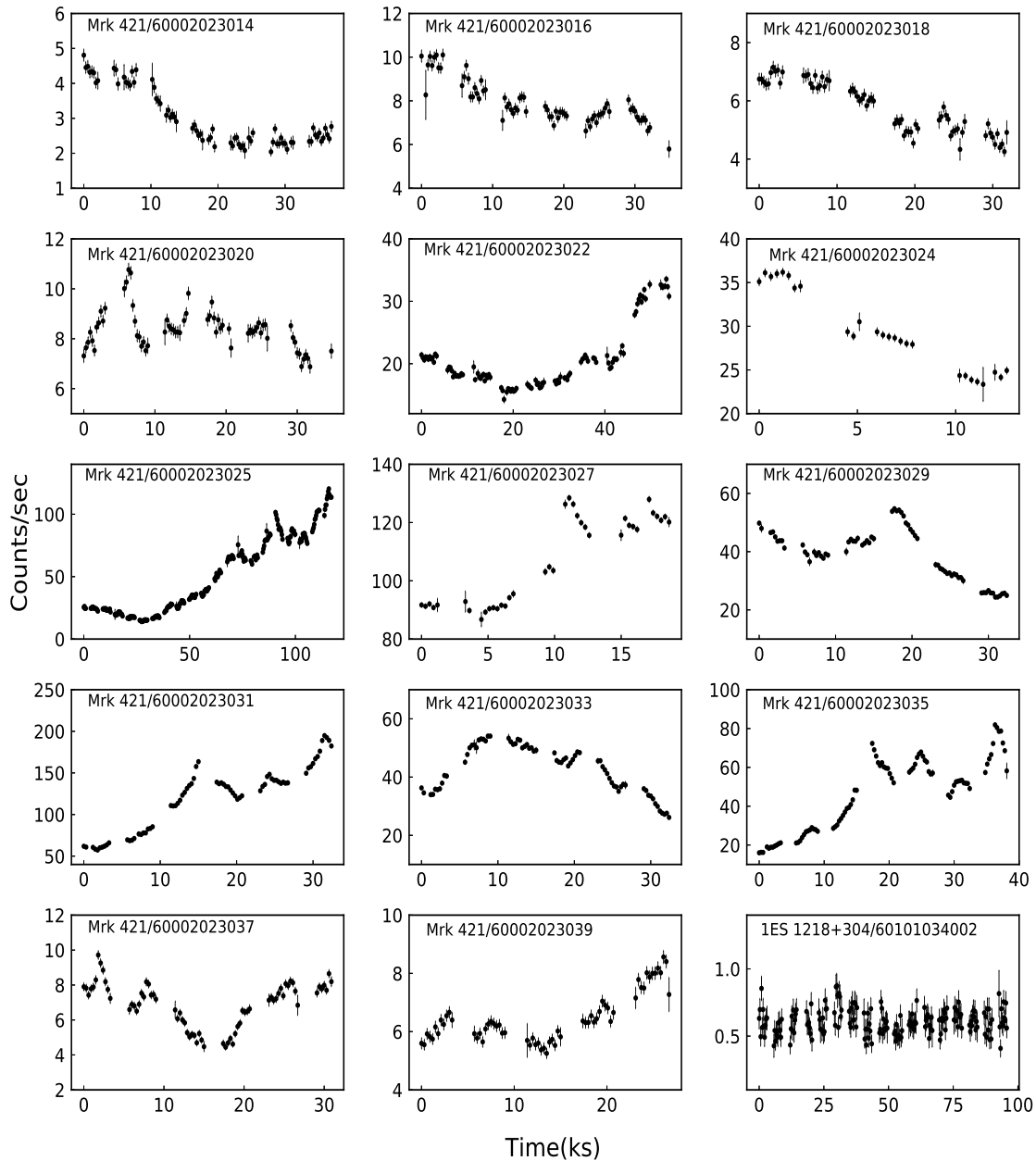


Figure 3.1b: *NuSTAR* light curves of the TeV HBLs Mrk 421 and 1ES 1218+304. The name of the HBL and the observation ID are given in each plot.

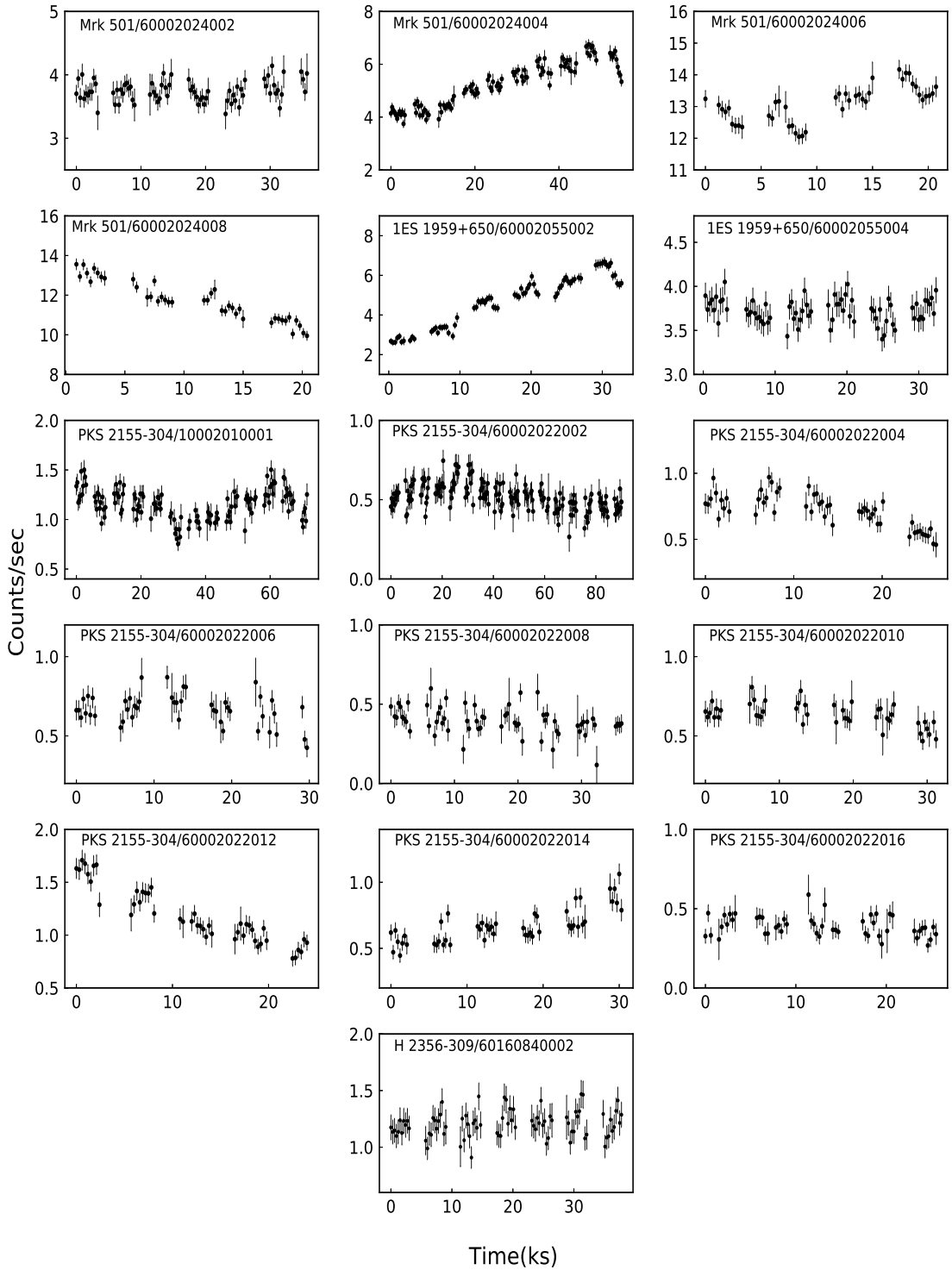


Figure 3.1c: *NuSTAR* light curves of the TeV HBLs Mrk 501, 1ES 1959+650, PKS 2155–304 and H 2356–309. The name of the HBL and the observation ID are given in each plot.

3. X-RAY FLUX AND SPECTRAL VARIABILITY OF TEV BLAZARS WITH *NUSTAR*

The error in DCF for each bin is defined as (e.g. [Edelson & Krolik, 1988](#))

$$\sigma_{DCF}(\tau) = \frac{\sqrt{\sum [UDCF_{ij} - DCF(\tau)]^2}}{M - 1}. \quad (3.8)$$

The DCF values are, then, plotted against the time lag. The following information can be inferred from the DCF plot about the correlation between the two time series.

- a positive DCF peak implies that the two light curves are correlated,
- a negative DCF peak implies that the two data signals are anti-correlated,
- no DCF peak, or $DCF=0$, means that no correlation exists between the two time series.

When a data series is correlated with itself (i.e., $x = y$), we get the auto-correlation function (ACF) that has an automatic peak at $\tau = 0$, indicating no time lag, which is obvious. Any other strong ACF peak can indicate the presence of periodicity, while the strong dips provide evidence of the presence and value of a variability timescale in the data.

3.3.3 Hardness Ratio

The hardness ratio (HR) is a simple, model independent, crude method to study the spectral variations. Since the earlier focusing X-ray telescopes provide energy coverage upto 10 keV, we extracted *NuSTAR* LCs in two energy bands; a soft band (3–10 keV) and a hard band (10–79 keV). We, then, calculated the HR as

$$HR = \frac{(H - S)}{(H + S)}, \quad (3.9)$$

and the error in HR (σ_{HR}) is computed as

$$\sigma_{HR} = \frac{2}{(H + S)^2} \sqrt{(H^2 \sigma_S^2 + S^2 \sigma_H^2)}, \quad (3.10)$$

where S and H are the total count rates, σ_S and σ_H are their errors in the soft (3–10 keV) and hard (10–79 keV) bands, respectively. We investigated the variations of HRs with time to examine spectral changes over the broad (3–79 keV) X-ray energy band.

3.3.4 Spectral Fitting

We used XSPEC⁴ version 12.9.0 to analysis the *NuSTAR* spectra. Before spectral fitting, the *NuSTAR* spectra were grouped using the FTOOL *grppha* to ensure a minimum of 20 counts per bin. We, then, simultaneously fitted the spectra of two *NuSTAR* detectors, FPMA and FPMB, for each observation with two models using the χ^2 –statistics. The first model, used for fitting *NuSTAR* spectra, is a power-law (PL), which is defined as:

$$F(E) = KE^{-\Gamma} \quad (3.11)$$

where Γ is the photon index, $F(E)$ is the flux at energy E , and K is the normalization parameter (photons keV⁻¹ cm⁻² s⁻¹).

The second model, we used, is the log-parabola (LP) model. It is found that the X-ray spectra of TeV HBLs are usually curved and are described well by the log-parabola model (Massaro et al., 2004; Tramacere et al., 2007), which is defined as

$$F(E) = K(E/E_{pivot})^{-(\alpha+\beta \log(E/E_{pivot}))} \quad (3.12)$$

where α is the local photon index at fixed energy $E_{pivot} = 10$ keV, β is the spectral curvature, and K is the normalization parameter.

To account for the effect of galactic absorption, we multiply each model with a *phabs* component taking fixed values of hydrogen column density (n_H), given in Table 3.5. The values of the fitted model parameters for all TeV HBL are listed in Table 3.5, where error in each parameter is estimated to a 90% confidence level ($\chi^2 = 2.706$).

3.4 Results

3.4.1 1ES 0229+200

The blazar 1ES 0229+200 is hosted by an elliptical galaxy at $z = 0.1396$ (Woo et al., 2005), and was classified as a BL Lac object by Schachter et al. (1993) because of its featureless optical spectrum. It was listed as a HBL on the basis of its X-ray to radio flux ratio (Giommi et al., 1995). It was first detected in X-rays

⁴<https://heasarc.gsfc.nasa.gov/docs/xanadu/xspec/XspecManual.pdf>

3. X-RAY FLUX AND SPECTRAL VARIABILITY OF TEV BLAZARS WITH *NUSTAR*

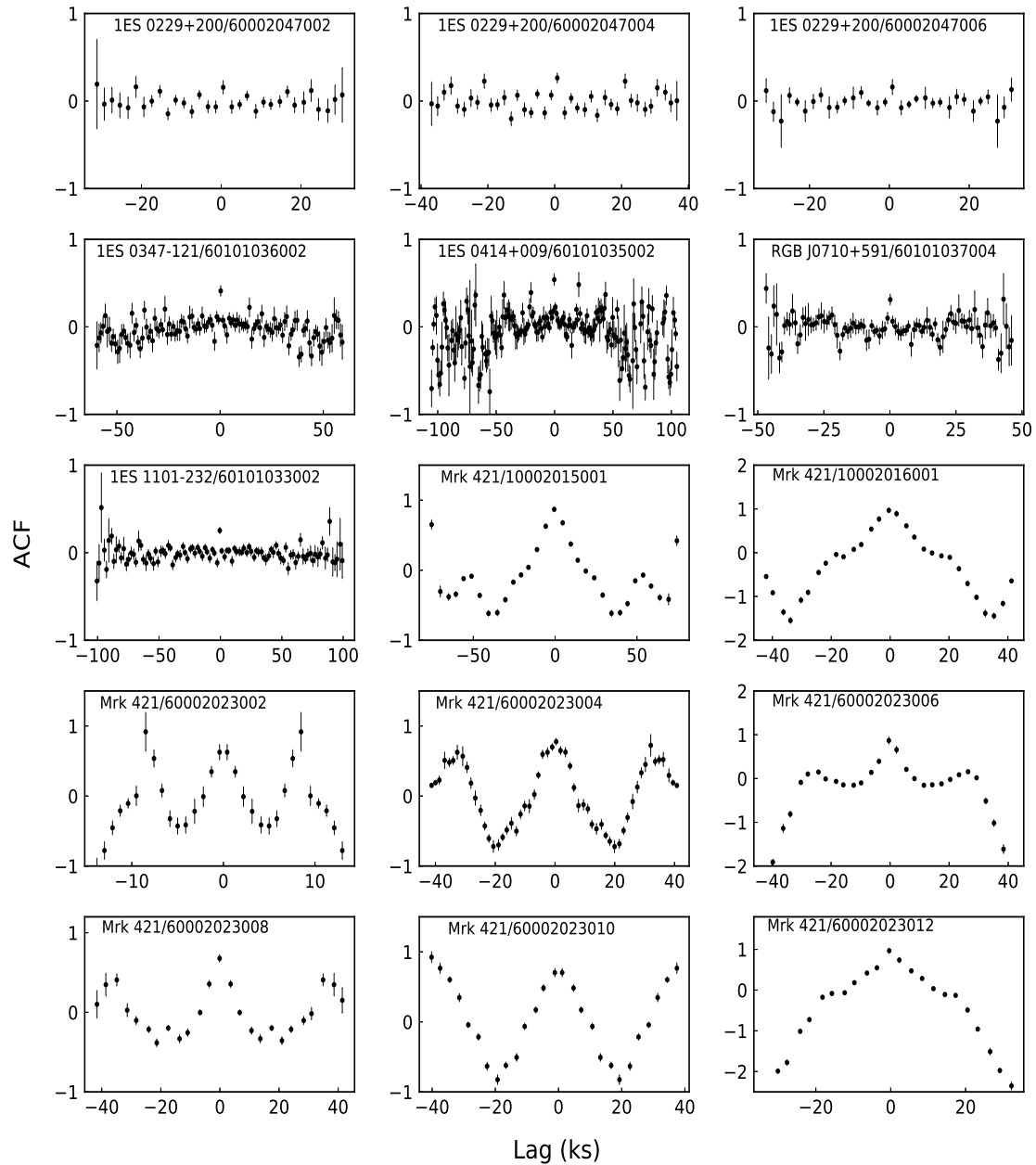


Figure 3.2a: Auto Correlation functions for LCs of the blazars 1ES 0229+200, 1ES 0347–121, 1ES 0414+009, RGB J0710+591, 1ES 1101–232 and Mrk 421.

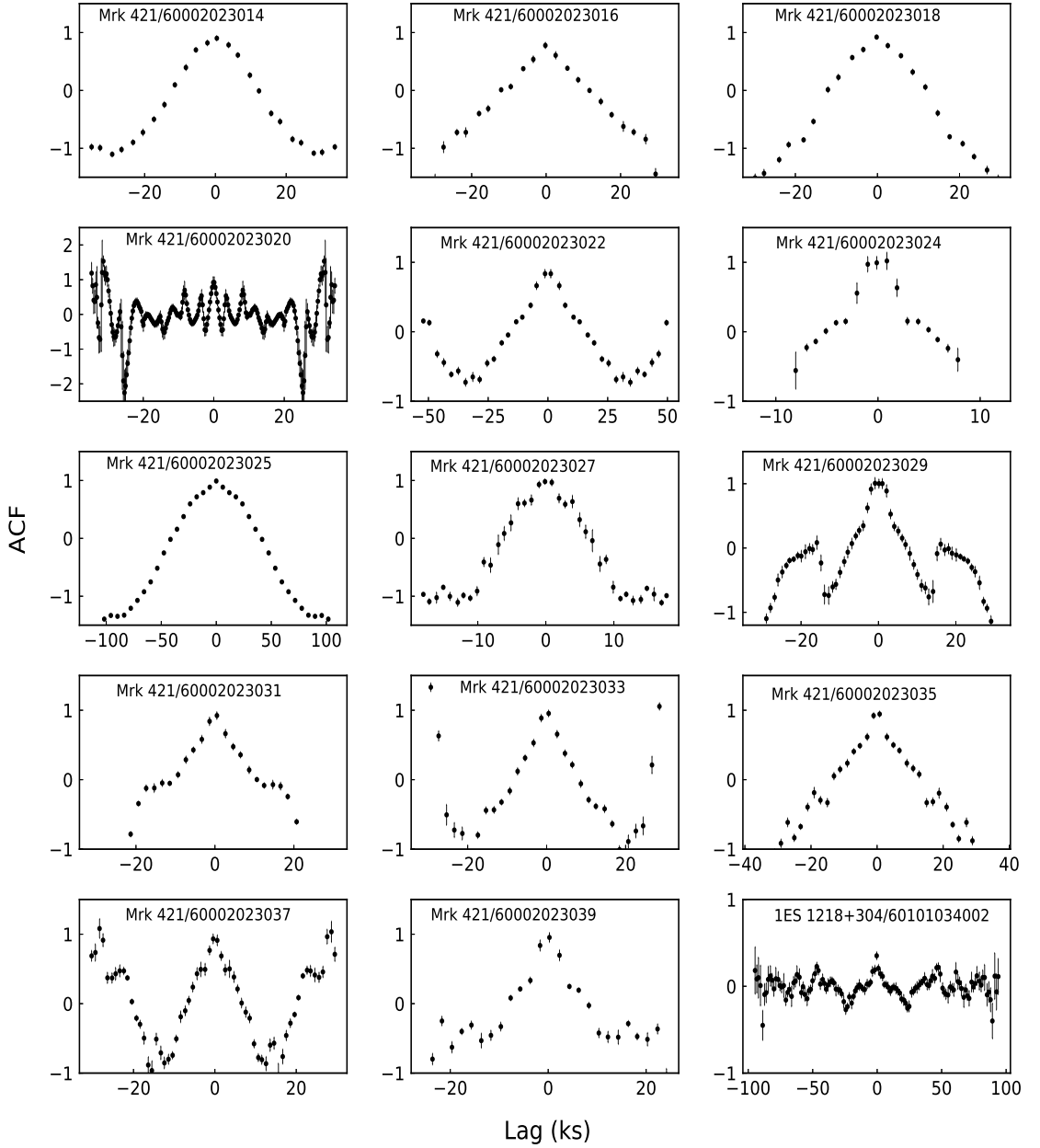


Figure 3.2b: ACFs for LCs of the blazars Mrk 421 and 1ES 1218+304.

in the *Einstein* satellite's Imaging Proportional Counter (IPC) ([Elvis et al., 1992](#)). The High Energy Stereoscopic System (HESS) observed 1ES 0229+200 for the first time at very high energy (VHE) above 580 GeV in 2006, but no evidence for VHE variability on any timescale was found ([Aharonian et al., 2007a](#)). [Aliu et al. \(2014\)](#) presented long-term VHE observations of 1ES 0229+200 from 2010 to 2012 using the Very Energetic Radiation Imaging Telescope Array System (VERITAS) and reported VHE variability on yearly time scales. In 2009, the X-ray flux from 1ES 0229+200 varied by a factor of ≈ 2 . Recently, [Cologna et al. \(2015\)](#) studied flux variability of 1ES 0229+200 at VHE on monthly and yearly timescales (from 2004

3. X-RAY FLUX AND SPECTRAL VARIABILITY OF TEV BLAZARS WITH *NUSTAR*

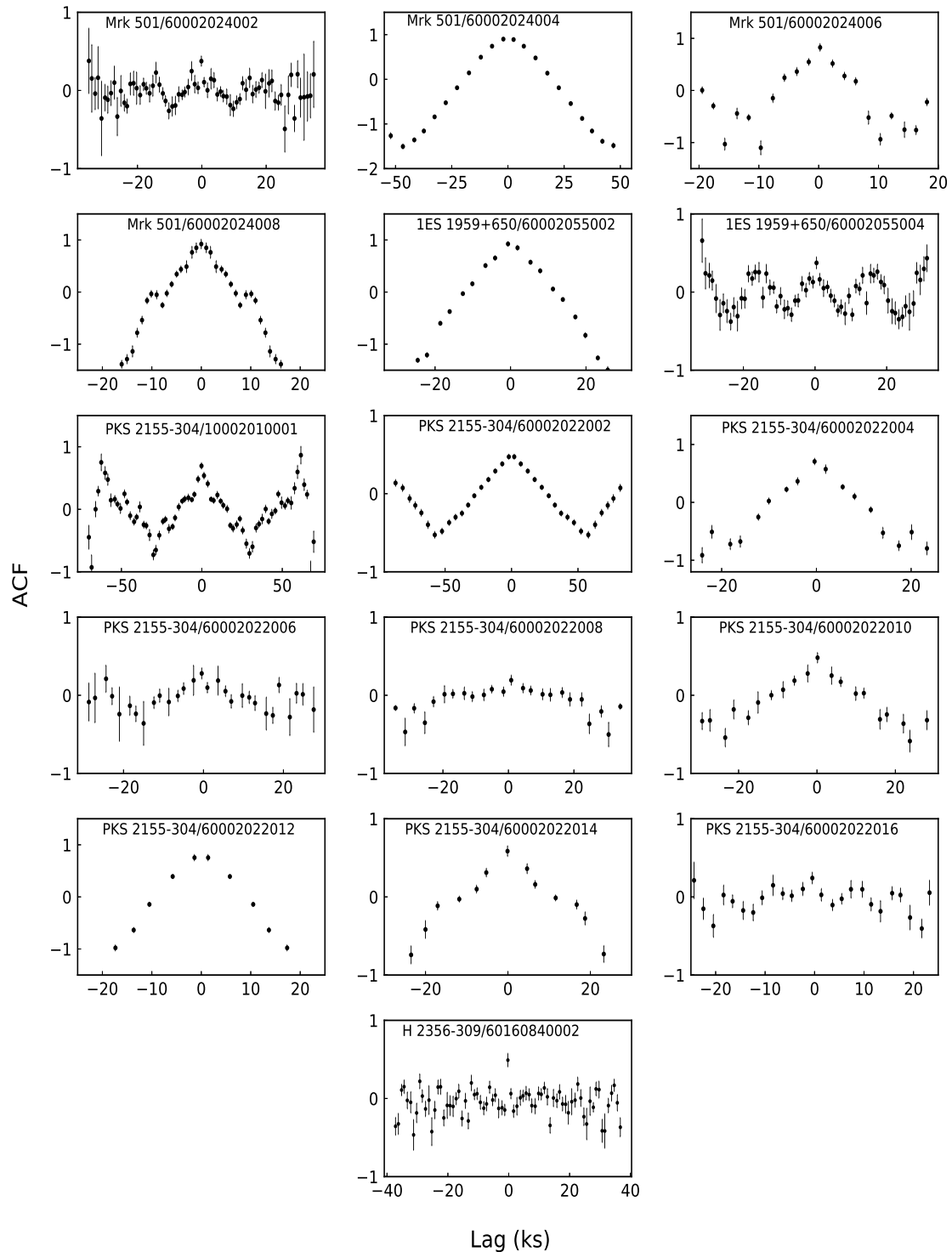


Figure 3.2c: ACFs for LCs of the blazars Mrk 501, 1ES 1959+650, PKS 2155–304 and H 2356–309.

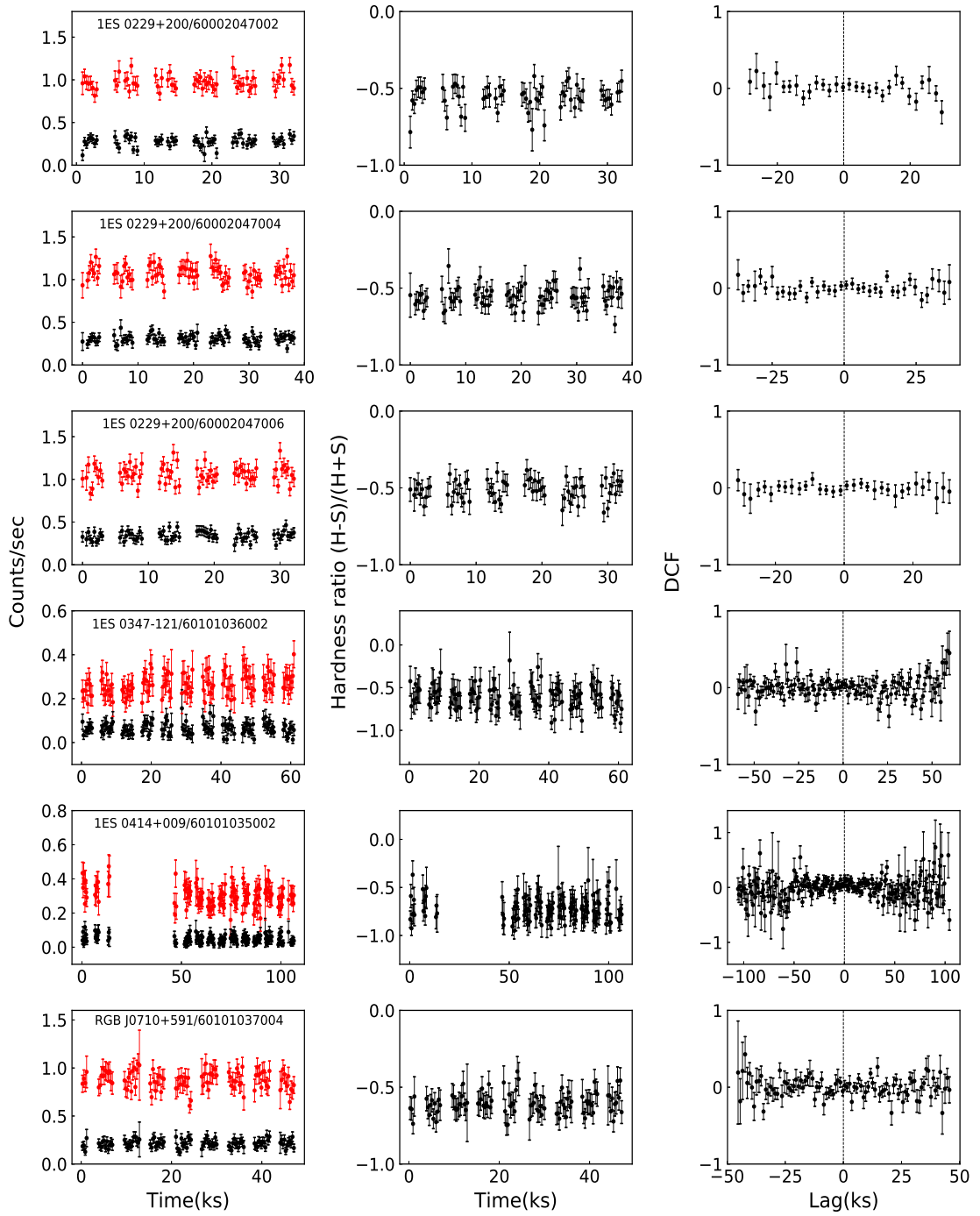


Figure 3.3a: Soft (3-10 keV, denoted by red filled circles) and hard (10-79 keV, denoted by black filled circles) band LCs (left panels), HR plots (middle panels), and the DCF plots between soft and hard band LCs (right panels) of the blazars 1ES 0229+200, 1ES 0347-121, 1ES 0414+009, and RGB J0710+591. The blazar names and observation IDs are given in the left panels.

3. X-RAY FLUX AND SPECTRAL VARIABILITY OF TEV BLAZARS WITH *NUSTAR*

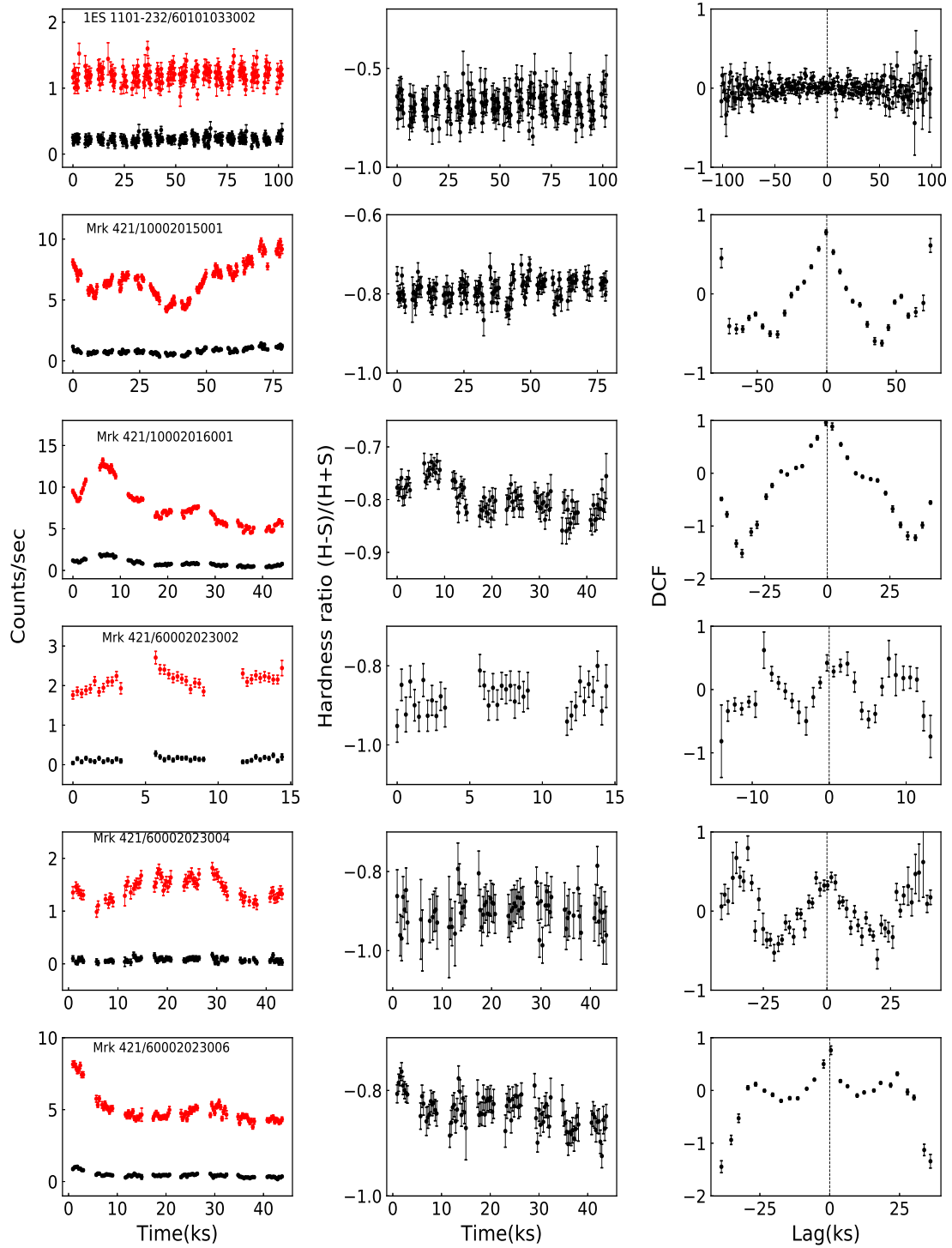


Figure 3.3b: As in Figure 3.3a, but for 1ES 1101–232 and Mrk 421.

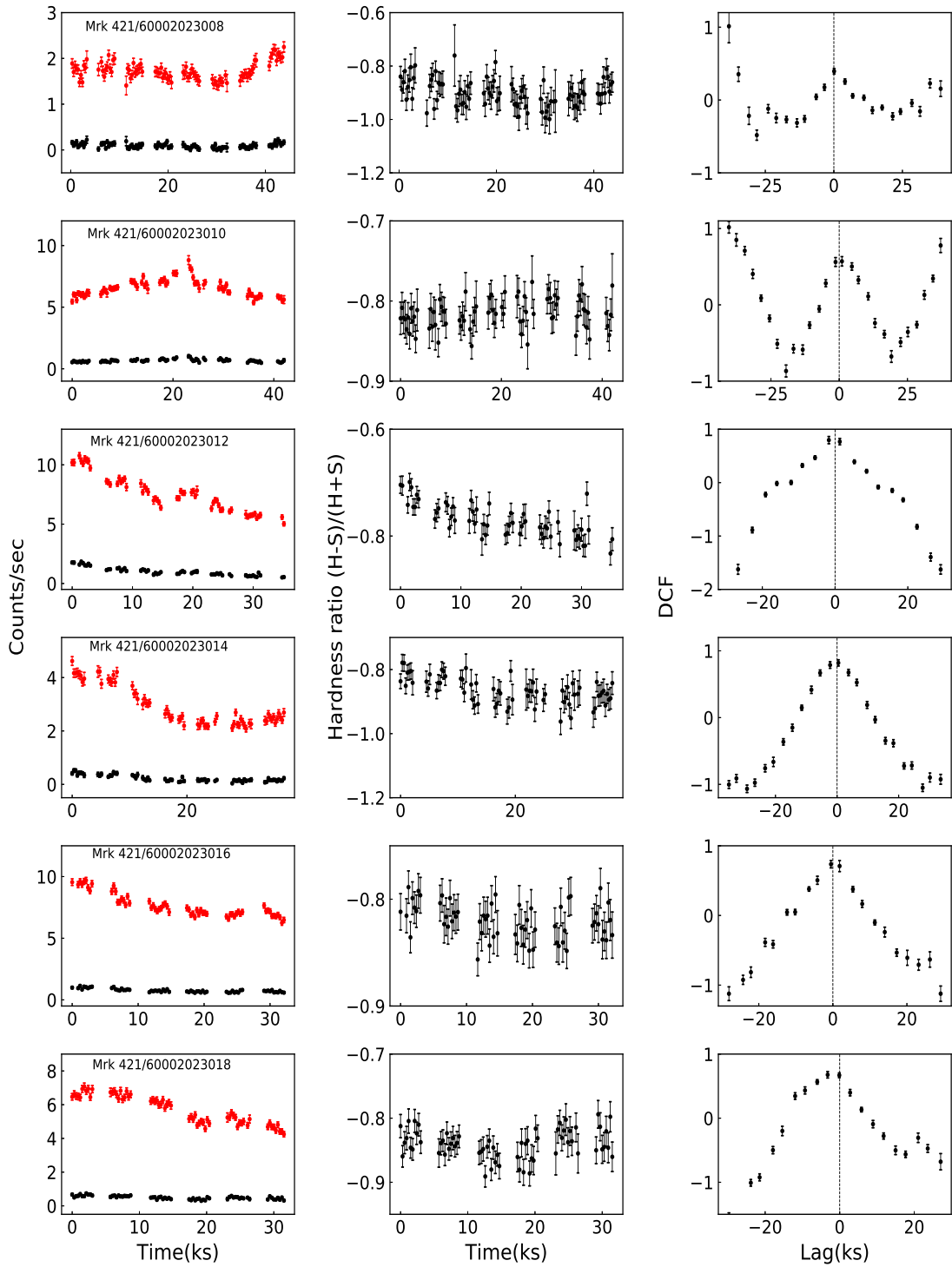


Figure 3.3c: As in Figure 3.3a, but for Mrk 421.

3. X-RAY FLUX AND SPECTRAL VARIABILITY OF TEV BLAZARS WITH *NUSTAR*

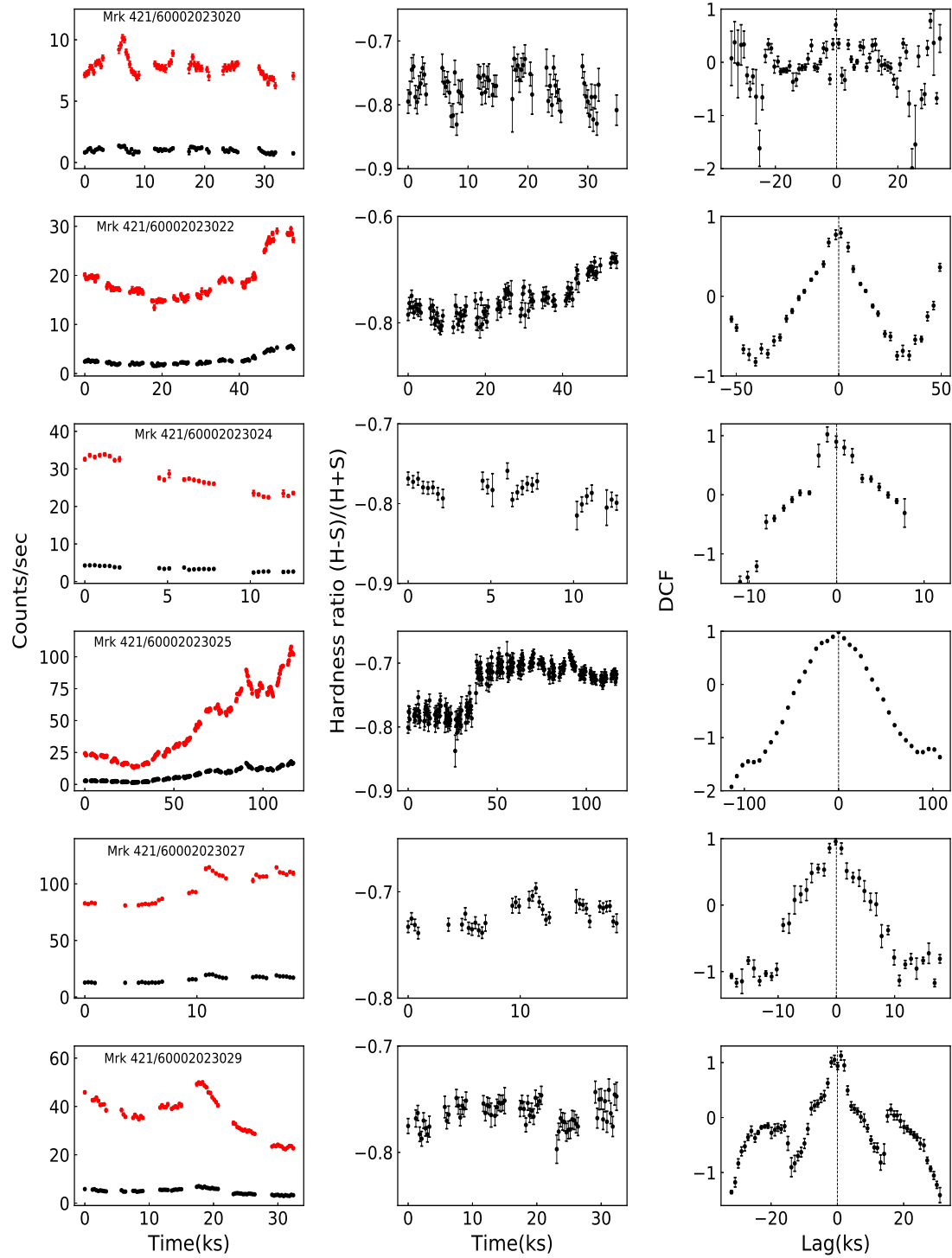


Figure 3.3d: As in Figure 3.3a, but for Mrk 421.

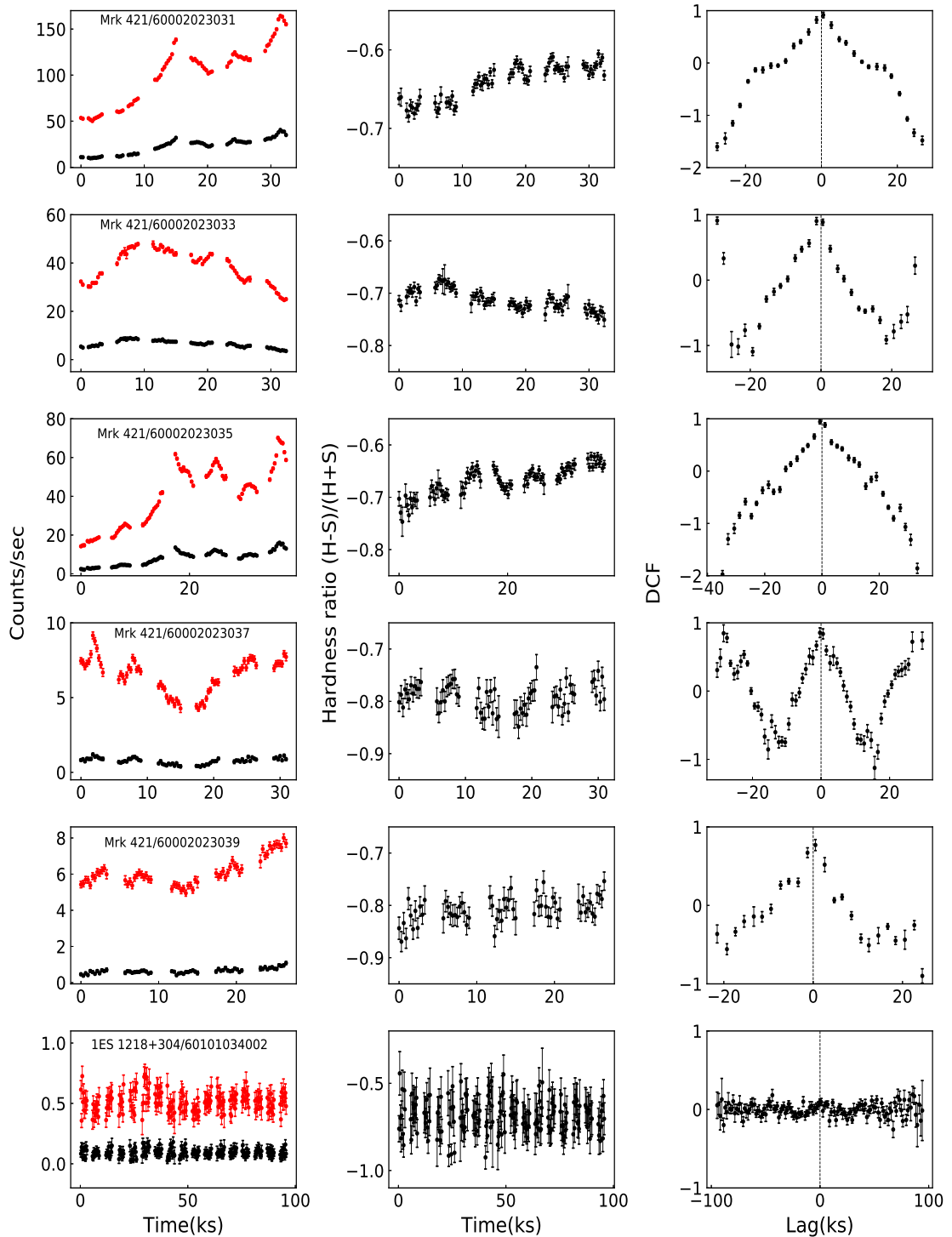


Figure 3.3e: As in Figure 3.3a, but for Mrk 421, and 1ES 1218+304.

3. X-RAY FLUX AND SPECTRAL VARIABILITY OF TEV BLAZARS WITH *NUSTAR*

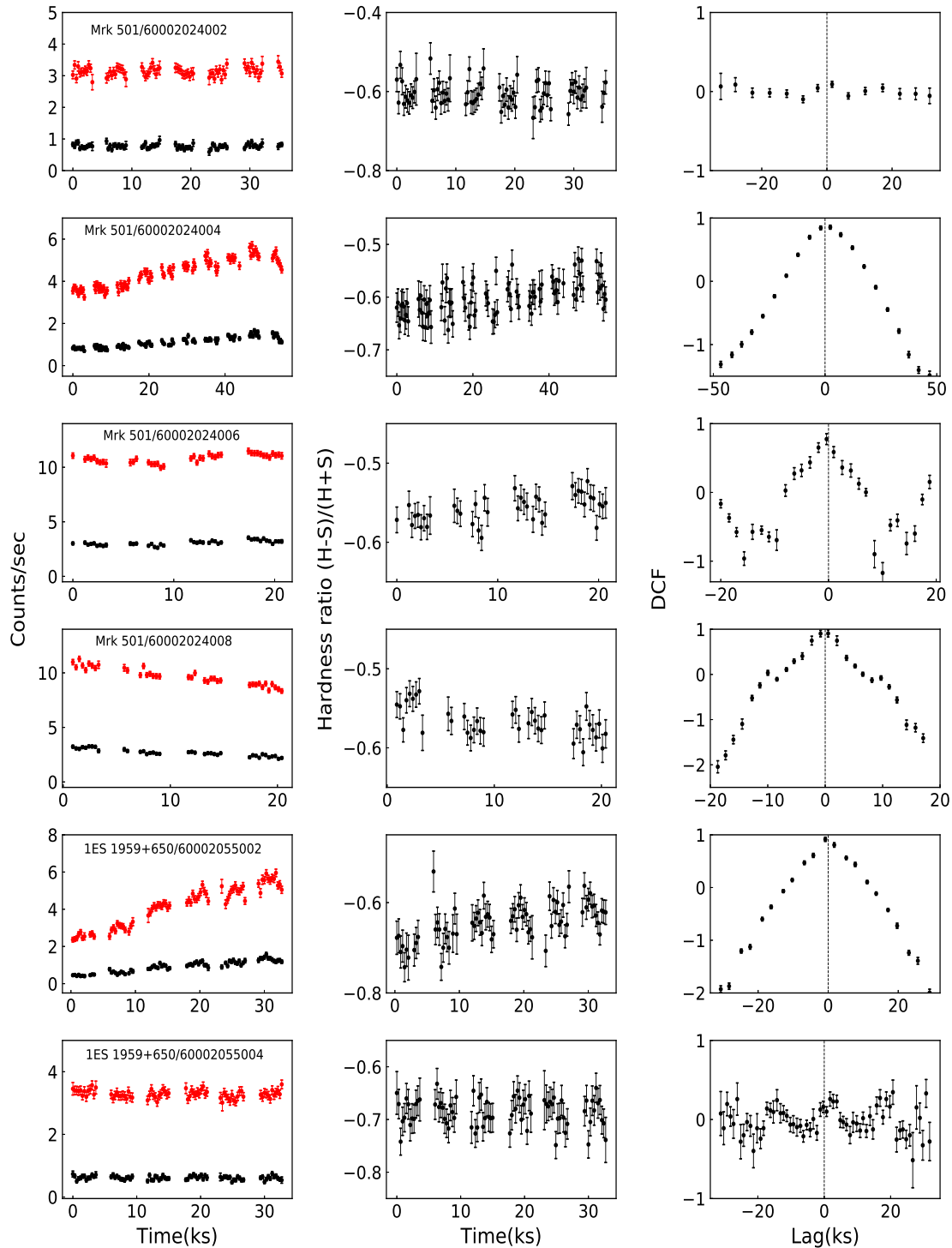


Figure 3.3f: As in Figure 3.3a, but for Mrk 501, and 1ES 1959+650.

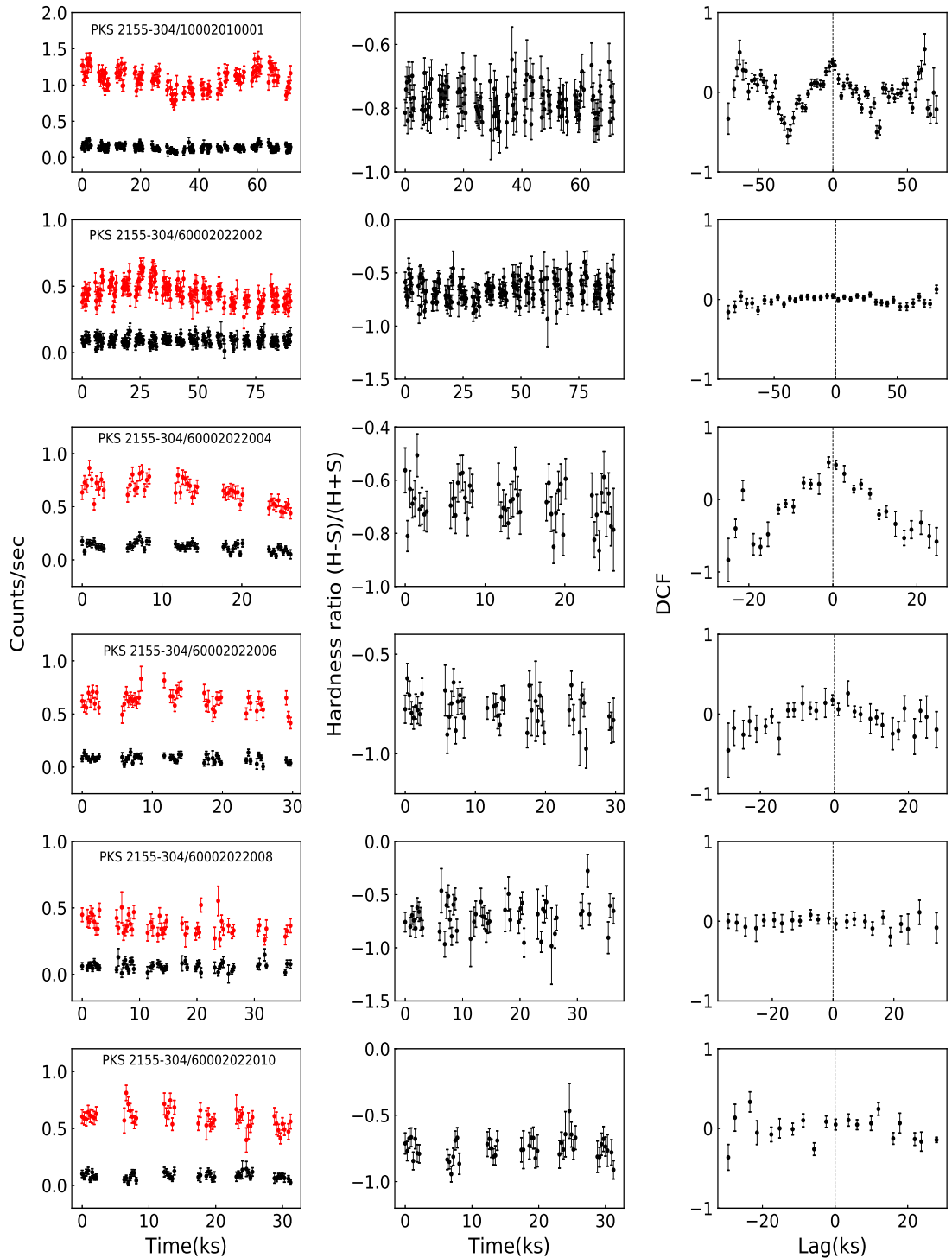


Figure 3.3g: As in Figure 3.3a, but for PKS 2155–304.

3. X-RAY FLUX AND SPECTRAL VARIABILITY OF TEV BLAZARS WITH *NUSTAR*

Table 3.4: X-ray variability parameters.

Blazar Name	Obs. ID	F_{var} (percent)			ACF(ks)	Bin-size(ks)
		Soft (3–10 keV)	Hard (10–79 keV)	Total (3–79 keV)		
1ES 0229+200	60002047002	...	15.632 ± 4.757	2.00
	60002047004	2.00
	60002047006	8.638 ± 2.557	...	4.460 ± 3.411	...	2.00
1ES 0347–121	60101036002	1.00
1ES 0414+009	60101035002	5.72 ± 3.73	...	1.00
RGB J0710+591	60101037004	1.00
1ES 1101–232	60101033002	4.24 ± 1.10	9.08 ± 2.81	3.94 ± 0.99	...	2.00
MRK 421	10002015001	21.105 ± 0.341	26.899 ± 1.179	21.217 ± 0.260	...	5.00
	10002016001	31.225 ± 0.337	48.503 ± 1.227	32.314 ± 0.305	...	3.00
	60002023002	7.531 ± 1.183	68.747 ± 8.125	9.159 ± 1.029	4.9	0.90
	60002023004	12.173 ± 0.874	75.723 ± 13.099	11.485 ± 0.860	19.9	1.50
	60002023006	20.051 ± 0.402	39.626 ± 1.695	21.595 ± 0.392	11.4	3.00
	60002023008	13.566 ± 0.721	31.496 ± 9.967	10.275 ± 0.757	...	3.50
	60002023010	10.371 ± 0.517	8.027 ± 3.382	10.264 ± 0.411	19.5	3.00
	60002023012	20.310 ± 0.463	33.744 ± 1.475	21.556 ± 0.424	...	3.00
	60002023014	25.203 ± 1.219	21.537 ± 11.947	26.702 ± 0.652	...	3.00
	60002023016	12.497 ± 0.550	13.995 ± 2.175	11.815 ± 0.421	...	3.00
	60002023018	14.707 ± 0.453	14.930 ± 2.339	14.583 ± 0.420	...	3.00
	60002023020	10.217 ± 1.284	...	9.164 ± 0.374	2.5	0.30
	60002023022	22.052 ± 0.386	40.386 ± 1.243	24.265 ± 0.193	32.8	3.00
	60002023024	15.181 ± 0.431	17.344 ± 1.401	15.458 ± 0.411	...	1.00
	60002023025	59.837 ± 0.131	64.919 ± 0.351	60.497 ± 0.123	...	6.00
	60002023027	13.406 ± 0.196	17.386 ± 0.486	13.945 ± 0.182	...	1.00
	60002023029	25.285 ± 0.184	26.116 ± 0.517	22.266 ± 0.175	13.1	1.00
	60002023031	31.141 ± 0.108	36.316 ± 0.229	32.073 ± 0.098	...	2.00
	60002023033	19.344 ± 0.540	25.137 ± 0.458	18.747 ± 0.169	...	2.00
	60002023035	39.043 ± 0.178	44.841 ± 0.427	39.943 ± 0.165	...	2.00
	60002023037	17.584 ± 0.404	24.000 ± 1.382	18.268 ± 0.387	12.6	1.00
	60002023039	12.310 ± 0.460	17.255 ± 1.798	12.773 ± 0.443	...	2.00
1ES 1218+304	60101034002	7.30 ± 1.84	7.28 ± 8.70	7.62 ± 1.49	23.51	1.50
MRK 501	60002024002	1.327 ± 1.406	...	1.391 ± 1.121	...	1.00
	60002024004	14.572 ± 0.627	20.901 ± 1.940	15.540 ± 0.354	...	5.00
	60002024006	4.278 ± 0.432	5.138 ± 0.925	3.743 ± 0.351	...	2.00
	60002024008	6.338 ± 0.670	9.067 ± 1.400	8.284 ± 0.358	8.0	1.00
1ES 1959+650	60002055002	26.849 ± 1.192	35.449 ± 2.876	26.629 ± 0.451	...	3.00
	60002055004	...	6.522 ± 2.963	1.00
PKS 2155–304	10002010001	12.901 ± 0.915	33.771 ± 5.960	10.601 ± 0.744	29.6	2.00
	60002022002	...	21.275 ± 5.478	11.020 ± 1.109	57.4	5.00
	60002022004	12.551 ± 2.437	21.333 ± 7.654	14.931 ± 1.400	...	3.00
	60002022006	10.830 ± 4.268	...	9.256 ± 2.162	...	2.00
	60002022008	...	28.233 ± 15.966	13.504 ± 3.000	...	3.00
	60002022010	...	12.931 ± 15.148	3.00
	60002022012	20.963 ± 1.300	24.613 ± 3.958	20.916 ± 1.160	...	4.00
	60002022014	16.726 ± 2.082	...	16.992 ± 1.554	...	4.00
	60002022016	16.810 ± 2.876	...	3.298 ± 8.251	...	2.00
	H 2356–309	60160840002	...	2.10 ± 3.40	...	1.00

to 2013) with H.E.S.S and found a hint of a correlation between VHE emissions and X-ray.

1ES 0229+200 was observed with *NuSTAR* for 16.26 ks, 20.29 ks and 18.02 ks on 2013 October 2, 5, and 10, respectively. The 3–79 keV LCs and their ACFs are plotted in Figures 3.1a, and 3.2a, respectively. The count rates are low and the data are noisy, so all fractional variances (F_{var}) are consistent with no significant variability detection on any of those days in the entire 3–79 keV energy band.

Table 3.5: Model fits to the NuSTAR spectra

Blazar Name	$n_H^{(a)}$	Obs. ID	Power Law		Log-parabola ($E_{pivot} = 10$ keV)		Flux $_{3-79keV}^{(2)}$	F-test	p-value
			Γ	$\chi^2/dof(\chi_r^2)$	α	β			
IES 0347–121	3.05	60101036002	2.37 ± 0.06	154.74/169 (0.92)	2.47 ± 0.10	0.37 ± 0.25	148.37/168 (0.88)	0.68 ± 0.03	7.21×10^{-3}
IES 0414+009	8.51	60101035002	2.77 ± 0.06	164.66/182 (0.90)	2.82 ± 0.10	0.16 ± 0.25	163.59/181 (0.90)	0.71 ± 0.02	1.18×0.27
RGB J0710+591	4.44	60101037004	2.27 ± 0.03	401.23/371 (1.08)	2.34 ± 0.05	0.35 ± 0.13	380.84/370 (1.02)	2.41 ± 0.06	1.13×10^{-5}
IES 1101–232	5.60	60101033002	2.50 ± 0.02	640.45/579 (1.11)	2.59 ± 0.03	0.35 ± 0.08	584.09/578 (1.01)	2.94 ± 0.07	3.02×10^{-13}
IES 1218+304	1.94	60101034002	2.55 ± 0.03	361.34/366 (0.99)	2.67 ± 0.06	0.43 ± 0.15	336.76/365 (0.92)	1.19 ± 0.03	26.64×10^{-7}
H 2356–309	1.44	60160840002	2.18 ± 0.03	349.67/357 (0.98)	2.23 ± 0.04	0.27 ± 0.13	336.91/356 (0.95)	2.81 ± 0.06	$13.48 \times 2.78 \times 10^{-4}$

(1) galactic hydrogen column density in units of 10^{20} cm $^{-2}$ taken from [Kalberla et al. \(2005\)](#),
 (2) 3–79 keV unabsorbed flux for best fitted model in units of 10^{-11} erg cm $^{-2}$ s $^{-1}$

3. X-RAY FLUX AND SPECTRAL VARIABILITY OF TEV BLAZARS WITH *NUSTAR*

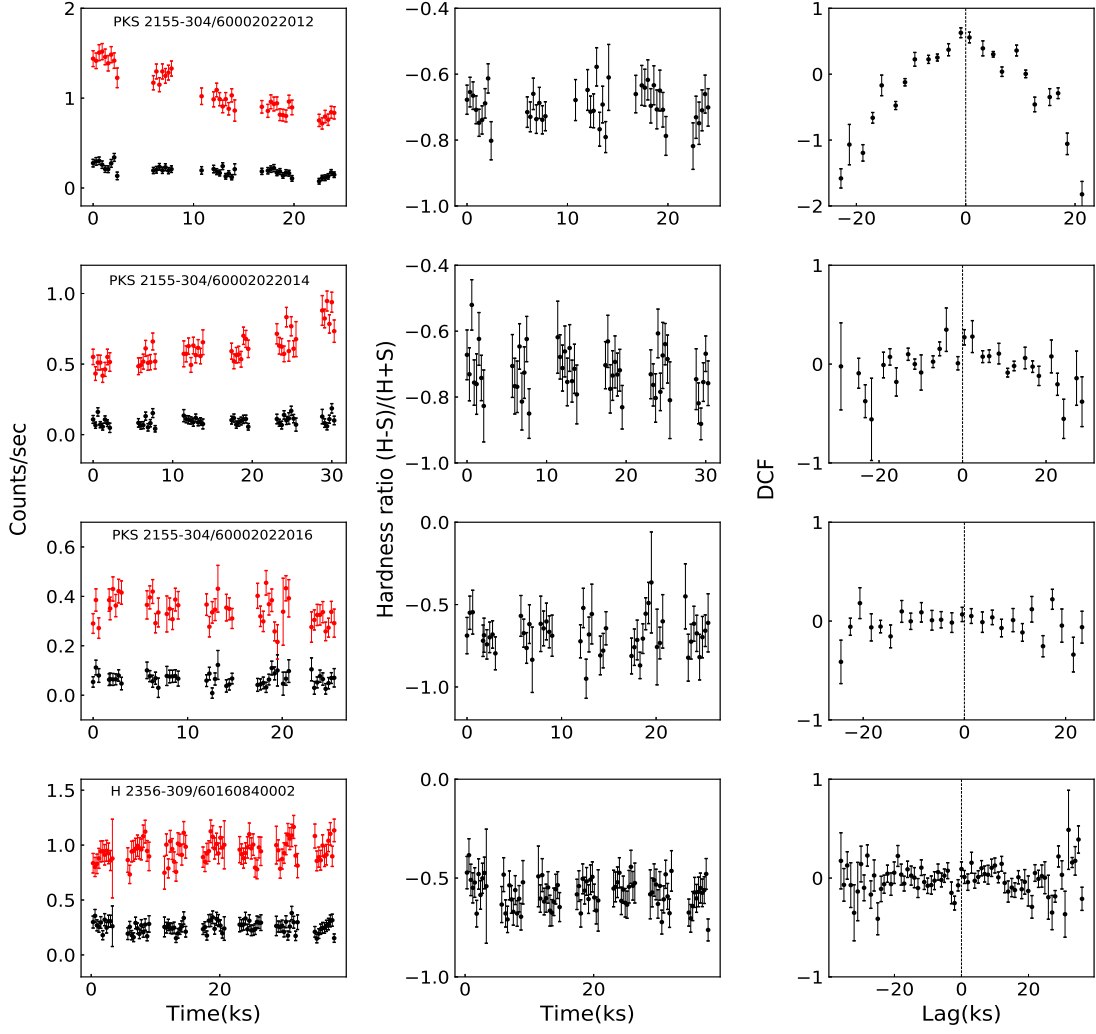


Figure 3.3h: As in Figure 3.3a, but for PKS 2155–304 and H 2356–309.

But nominally variations are seen in hard and soft bands on 2013 October 2 and 10, respectively. Unsurprisingly, the ACFs exhibit no hint of an IDV timescale.

The soft and hard LCs (left panel), HR plots (middle panel) and the DCF plot (right panel) between soft and hard band of TeV HBL 1ES 0229+200 are shown in Figure 3.3a. No detectable spectral changes are seen from the HR plots in any of the three observations. Naturally, due to the lack of significant variations, all the DCF plots are flat and consistent with zero throughout.

3.4.2 1ES 0347–121

The TeV HBL 1ES 0347–121, at $z = 0.188$ (Woo et al., 2005), was first detected in the Einstein Slew Survey (Elvis et al., 1992) and was later identified as a BL Lac object (Schachter et al., 1993). It was discovered at VHE by HESS (Aharonian et al., 2007b) with an integral flux (at $E > 250$ GeV) of $(3.9 \pm 1.1_{stat}) \times 10^{-12} \text{ cm}^{-2} \text{s}^{-1}$.

NuSTAR observed 1ES 0347–121 with a good exposure time of 32.93 ks on 2015 September 10. As seen from the 3–79 keV LC, shown in Figure 3.1a, the X-ray count rates are low and the data are noisy, so no significant IDV is seen. Hence, the corresponding ACF plot, shown in Figure 3.2a, is also noisy, providing no useful results.

The soft and hard LCs (left panel), HR plot (middle panel) and the DCF plot (right panel) between soft and hard band LCs of 1ES 0347–121 are shown in Figure 3.3a. The HR plot exhibits no significant spectral change. The DCF plot is flat, which would indicate no correlation between the two energy bands if significant variations were found, but since no variations are detectable such type of DCF is expected.

3.4.3 1ES 0414+009

1ES 0414+009 is a TeV HBL at $z = 0.287$ (Halpern et al., 1991). It was discovered in X-rays with High Energy Astronomy Observatory (HEAO A-1)(Ulmer et al., 1980) and was later classified as a BL Lac object by Ulmer et al. (1983). 1ES 0414+009 was observed above 200 GeV with VERITAS and the source flux was $(5.2 \pm 1.1_{stat} \pm 2.6_{sys}) \times 10^{-12} \text{ photons cm}^{-2} \text{ s}^{-1}$ (Aliu et al., 2012).

1ES 0414+009 was observed with *NuSTAR* with a good exposure time of 34.16 ks on 2015 November 25. The *NuSTAR* LC of 1ES 0414+009 is shown in Figure 3.1a. The data are both sparse and noisy, resulting in no detectable IDV which is consistent with the F_{var} value given in Table 3.4. Consequently, the ACF plot, shown in Figure 3.2a, does not indicate any hint of variability timescale.

The soft and hard LCs of 1ES 0414+009 are shown in the left panel of Figure 3.3a. The HR plot, plotted in the middle panel of that figure, shows no significant spectral variations and the DCF plot shown in the right panel of Figure 3.3a is unsurprisingly flat.

3. X-RAY FLUX AND SPECTRAL VARIABILITY OF TEV BLAZARS WITH *NUSTAR*

3.4.4 RGB J0710+591

The TeV HBL RGB J0710+591 is located at a redshift of $z = 0.125$ ([Giommi et al., 1991](#)) and was first detected by HEAO A-1 ([Wood et al., 1984](#)). It was detected at energies above 300 GeV by VERITAS with the integral flux recorded to be $(3.9 \pm 0.8) \times 10^{-12} \text{ cm}^{-2} \text{ s}^{-1}$ ([Acciari et al., 2010](#)).

NuSTAR observed the TeV blazar RGB J0710+591 on 2015 September 1 for 26.48 ks. Although there is a hint of variability as seen from the LC shown in Figure 3.1a. But the data are noisy, so no significant IDV are found, as shown by the F_{var} value. The ACF of RGB J0710+591, shown in Figure 3.2a, reveals no evidence of an IDV timescale.

Given that both the soft and hard LCs, shown in the left panel of Figure 3.3a, are noisy, the HR plot, shown in the middle panel of that figure, does not show any significant spectral variations and the DCF plot between the soft and hard band LCs, plotted in the right panel of Figure 3.3a, is steady within the noise.

3.4.5 1ES 1101–232

1ES 1101–232 is a TeV HBL at $z = 0.186$ ([Remillard et al., 1989](#)) and was discovered in the Einstein Slew Survey ([Perlman et al., 1996](#)). [Aharonian et al. \(2007d\)](#) was first detected VHE γ -ray emission from 1ES 1101–232 with integral flux (at $E > 200$ GeV) of $(4.5 \pm 1.2) \times 10^{12} \text{ erg cm}^{-2} \text{ s}^{-1}$.

1ES 1101–232 was observed with *NuSTAR* on 2016 January 12 for 50.79 ks. The 3–79 keV LC of 1ES 1101–232 shown in Figure 3.1a appears to show significant flux variations in the *NuSTAR* energy range. The value of F_{var} for the total energy range 3–79 keV given in Table 3.4 confirms the presence of IDV. The F_{var} values for the soft and hard bands, also listed in Table 3.4, confirm that the significant IDV variations are present in both these energy bands. Despite the presence of significant variability, the ACF plot shown in Figure 3.2a is almost flat, indicating no variability timescale.

The soft and hard LCs (left panel), HR (middle panel) and the DCF plot (right panel) between soft and hard band LCs for 1ES 1101–232 are plotted in Figure 3.3a. The HR plot shows no detectable spectral changes, nor is significant correlation seen from the DCF plot, despite the presence of significant variability. In

this case, these flat curves yield some evidence that the emission mechanism for both the bands is the same.

3.4.6 Mrk 421

The TeV blazar Markarian 421 (Mrk 421), is one of the nearest ($z = 0.031$) BL Lac objects and was the first extragalactic object observed at TeV energy (Punch et al., 1992). It is identified as an HBL because its synchrotron peak lies at soft X-rays. Mrk 421 is highly variable over the entire electromagnetic spectrum at all timescales and has been extensively monitored during its flaring states (e.g. Takahashi et al. (1994); Kerrick et al. (1995); Takahashi et al. (1995); Fan & Lin (1999); Gupta et al. (2004); Teräsranta et al. (2004, 2005); Costa et al. (2008); Pittori et al. (2008); Smith et al. (2008); Gaur et al. (2012); Lico et al. (2012); Blasi et al. (2013); Racero & de la Calle (2013); Abdo et al. (2014)). A major flare was detected with the flux reaching up to ~ 8.5 mCrab in the 2.0–10.0 keV energy range in the spring to summer of 2006 (Tramacere et al., 2009; Ushio et al., 2009). In 2010 January and February, strong X-ray flares were recorded, with the maximum flux detected to be 120 ± 10 mCrab and 164 ± 17 mCrab respectively, with the latter being the highest ever reported from the source (Isobe et al., 2015). In 2012 and 2013, Mrk 421 exhibited two flares (Hovatta et al., 2015) and the gamma-ray flare in 2012 was recorded without a simultaneous X-ray flare, a behavior known as an ‘orphan flare’ (Fraija et al., 2015). It has been studied in several multi-wavelength campaigns due to its variable nature at all wavelengths (e.g. Błażejowski et al., 2005; Fossati et al., 2008; Gupta et al., 2008a; Horan et al., 2009; Gaur et al., 2012; Aleksić et al., 2015; MAGIC Collaboration et al., 2016; Li et al., 2016). Recently, Sinha et al. (2016) performed a long-term study of Mrk 421 with the High Altitude Gamma Ray (HAGAR) telescope array at Hanle, India, and detected strong correlations between the gamma and radio wavelengths and between the optical and gamma wavebands, but found no correlation between gamma and X-ray emissions. They also found that the variability depends on energy, being maximum in VHE bands and in X-rays.

Mrk 421 was first detected with *NuSTAR* twice during July 2012 for the calibration of the telescope. It was then observed several times in January – April 2013 as part of an extensive multi-wavelength observational campaign that involved simultaneous or quasi-simultaneous data observed in the radio, optical, soft X-ray, hard X-ray, and γ -ray bands (Baloković et al., 2016). Baloković et al. (2016) and Kataoka & Stawarz (2016) reported the results of the first part of this study,

3. X-RAY FLUX AND SPECTRAL VARIABILITY OF TEV BLAZARS WITH *NUSTAR*

involving the low-flux state seen in January – March 2013. [Paliya et al. \(2015\)](#) presented the results of variability analysis and [Sinha et al. \(2015\)](#) reported results of the study of spectral variations during the strong flaring state in April 2013 using *NuSTAR* data.

The 3–79 keV LCs of Mrk 421 that we have re-reduced for our study and plotted in Figures 3.1a and 3.1b indicate that significant variations are seen during all the 22 observations. Our F_{var} values given in Table 3.4 confirm these variations and thus echo the results of [Paliya et al. \(2015\)](#) and [Baloković et al. \(2016\)](#) in this regard. The F_{var} values for soft and hard bands, also given in Table 3.4, indicate that the variability is stronger in the hard band than that in the soft band for 19 out of 22 observations. The full LC of Mrk 421 obtained from our analysis of the *NuSTAR* data is shown in Figure 3.4. Very strong flares were seen while Mrk 421 was observed nearly continuously during 2013 April 10 – 16 ([Paliya et al., 2015](#)). We have marked the unprecedented outburst during this period with a box in Figure 3.4 and plotted a zoomed version of that box as an inset to the figure. A double-peaked outburst can be clearly seen in which the first flare has a nearly a Gaussian shape with peak flux at \sim MJD 56395 while the second flare, occurring two days later, is even stronger, and displays a very sharp rise and decay. The LCs in soft and hard bands (left panel), HR plots (middle panel) and the DCF plots (right panel) of Mrk 421 are shown in Figures 3.3b, 3.3c, 3.3d, and 3.3e. The variations of HR with time show clear features of spectral variations that are stronger during flares. The spectra become harder with the increasing flux, indicating a general “harder when brighter” behavior of blazars. Similar X-ray variability behavior was already detected in *XMM-Newton* observations (e.g. [Brinkmann et al. \(2003\)](#); [Ravasio et al. \(2004\)](#)) and in *NuSTAR* observations (e.g. [Paliya et al. \(2015\)](#); [Baloković et al. \(2016\)](#)) of Mrk 421. As can be seen from the DCF plots, the soft and hard bands LCs are positively correlated with zero time lag, indicating that the emissions from these two bands come at the same time from the same emitting region.

The ACFs for the LCs of Mrk 421 are plotted in Figures 3.2a and 3.2b, and 8 of them exhibit structures indicative of timescales. The dates on which observations started for which these structures were noticed in the ACFs are 2013 January 2, 10 and 15, 2013 February 6, 2013, March 17, and 2013 April 2, 13 and 18, and the corresponding putative “variability timescales” which range from 2.5 to 32.8 ks, are given in Table 3.4. The other ACFs do not provide any variability timescales or are too noisy to get any useful information.

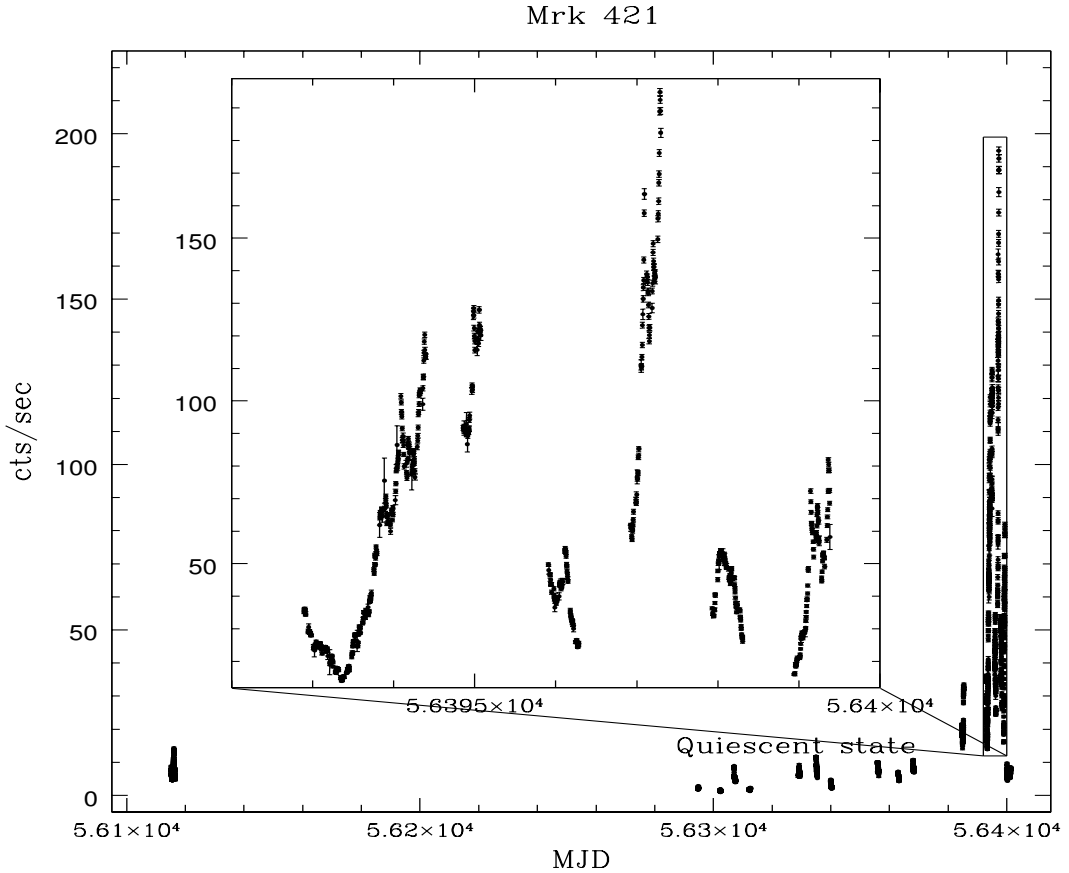


Figure 3.4: Short term variability of Mrk 421.

3.4.7 1ES 1218+304

1ES 1218+304 is an HBL at a redshift of $z = 0.182$ (Véron-Cetty & Véron, 2003). Sato et al. (2008) observed a flux over 2–10 keV range $\sim 2.0 \times 10^{-11}$ erg cm $^{-2}$ s $^{-1}$ and recently, an integrated flux of 3.33×10^{-11} erg cm $^{-2}$ s $^{-1}$ in the 0.3–10 keV range was found by Wierzcholska & Wagner (2016). The TeV flux ($E > 200$ GeV) of $(12.2 \pm 2.6) \times 10^{-12}$ cm $^{-2}$ s $^{-1}$ was observed from 1ES 1218+304 with VERITAS (Acciari et al., 2009b).

NuSTAR observed 1ES 1218+304 on 2015 November 23 with a good exposure time of 49.55 ks. The 3–79 keV LC and ACF plots of this TeV blazar are shown in Figure 3.1b and Figure 3.2b, respectively. As seen from the LC, 1ES 1218+304 shows clear intraday variations which are confirmed by the value of F_{var} given in Table 3.4. The variations are also clearly present in the soft band but not seen in the hard band. The ACF plot provides a possible IDV timescale of ~ 23.5 ks.

3. X-RAY FLUX AND SPECTRAL VARIABILITY OF TEV BLAZARS WITH *NUSTAR*

The soft and hard LCs of 1ES 1218+304 are shown in the left panel of Figure 3.3e. The Hardness ratio plot in the middle panel of that figure appears to show some variations but is quite noisy, providing no useful results. The DCF plot in the right panel of Figure 3.3e shows no correlations, as expected from the lack of detectable variability in the hard band.

3.4.8 Mrk 501

Markarian 501 (Mrk 501), located at a redshift of $z = 0.034$, was the second extra-galactic object observed at TeV energies. It was first observed at energy $E > 300$ GeV by the Whipple Observatory (Quinn et al., 1996). It went into a surprisingly high state in 1997 with the flux recorded up to 10 Crab at energies >1 TeV and it exhibited strong VHE variability (Catanese et al., 1997; Samuelson et al., 1998; Aharonian et al., 1997, 1999a,b). The highest VHE flux ($F \sim 8.3 \times 10^{-10} \text{ cm}^{-2} \text{ s}^{-1}$ at energies >250 GeV) ever was reported on 16 April 1997 (Djannati-Atai et al., 1999). In July 2005 fast VHE flux variations were observed from Mrk 501 with a flux doubling time of ~ 2 minutes (Albert et al., 2007). Neronov et al. (2012) detected an orphan VHE gamma-ray flare in 2009 that was not accompanied by an X-ray flare. Recently, HESS observed major flaring activity in June 2014 when the flux reached over 1 Crab and rapid flux variability was observed at VHE ($\sim 2\text{--}20$ TeV) (Chakraborty et al., 2015).

NuSTAR observed Mrk 501 on four occasions between 2013 April 13 and 2013 July 13 as part of an extensive multi-wavelength program. Data was accumulated from radio to γ -ray bands, with the last two observations taken as part of a target of opportunity program because of elevated states observed by other telescopes (Furniss et al., 2015). The LCs of Mrk 501 shown in Figure 3.1b clearly exhibit significant flux variations on IDV timescales during the last three nights of observations. The substantial values of F_{var} listed in Table 3.4 confirm these IDV detections for those observations. The values of F_{var} in the soft and hard bands given in Table 3.4 suggest greater variations in the hard band.

The soft and hard LCs are plotted in the left panels of Figure 3.3f. As seen from the HR plots in the middle panels of that figure, no significant spectral variations were seen during for first observation, while for the rest three observations the spectra become harder with increasing brightness and softer with decreasing brightness. Such spectral behaviour was also found in other X-ray observations (e.g. Pian et al. (1998); Aliu et al. (2016)). The DCF plots between soft and hard band

LCs shown in the right panels of Figure 3.3f indicate a positive correlation with zero lag between the two bands, except for the first observation, during which no significant variability is detected. Hence the ACF plot given in Figure 3.2b for the first observation is essentially noisy. While the second and third observations provide clear ACFs but do not indicate any hint of a variability timescale. However, the ACF plot of the last observation does indicate a possible timescale of ~ 8.0 ks.

3.4.9 1ES 1959+650

The TeV blazar 1ES 1959+650 is a BL Lac object at $z = 0.48$ (Perlman et al., 1996). This blazar was first observed at X-rays with the *Einstein* IPC Slew Survey (Elvis et al., 1992) and was further detected with *ROSAT* in 1996 and with *BeppeSAX* in 1997 (Beckmann et al., 2002), as well as with *RXTE-ARGOS*, *XMM-Newton* and *Swift* (Giebels et al., 2002; Tagliaferri et al., 2003; Massaro et al., 2008).

NuSTAR observed 1ES 1959+650 with good exposure times of 19.61 ks and 20.34 ks on 2014 September 17 and 22, respectively. The *NuSTAR* LCs and ACFs of 1ES 1959+650 are shown in Figures 3.1c and 3.2c, respectively. The flux increased dramatically over the span of 30 ks during the first observation. However, during the second measurements, the count rates were both lower and steadier. The ACF plot for the observation on 2014 September 17 does not indicate a timescale, while the observation on 2014 September 22 produces a noisy ACF and hence provides no useful information.

The soft and hard band LCs (left panels), HR plots (middle panels) and the DCF plots (right panels) for this blazar are plotted in Figure 3.3f. The HR plots reveal no spectral variations. The DCF plot for the observation on 2014 September 17 shows a correlation between the soft and hard bands with zero lag, while no such correlation is seen for the observation on 2014 September 22 naturally due to the lack of variability.

3.4.10 PKS 2155–304

The TeV blazar PKS 2155–304, at $z = 0.116$ (Falomo et al., 1993; Farina et al., 2016), is the brightest BL Lac object in UV–TeV energy range in the southern

3. X-RAY FLUX AND SPECTRAL VARIABILITY OF TEV BLAZARS WITH *NUSTAR*

hemisphere. It was first identified as a TeV blazar by the Durham MK6 telescopes (Chadwick et al., 1999). VHE flux variability on timescales of minutes was reported by Aharonian et al. (2007c). It has been observed at all wavelengths and flux variability on diverse timescales has been found by several authors (e.g. Urry et al., 1993; Gaur et al., 2010; Gupta, 2011; Zhang et al., 2014; Sandrinelli et al., 2016; Bhagwan et al., 2016). A possible ~ 4.6 hr quasi-periodic oscillation (QPO) in an X-ray LC was claimed by Lachowicz et al. (2009) using *XMM-Newton* data.

PKS 2155–304 was observed with *NuSTAR* on nine occasions between 2012 July 8 and 2013 September 28; the exposures ranged from 10.53 ks to 45.06 ks. All 3–79 keV LCs and their ACFs are shown in Figures 3.1c and 3.2c, respectively. A visual inspection of the LCs indicates hints of IDV on most of the dates. The values of F_{var} and their errors in 3–79 keV range given in Table 3.4 confirm the IDV detection on 7 out of the 9 observations. The values of F_{var} in soft and hard bands are also given in Table 3.4. Variability timescales of 29.6 and 57.4 ks are indicated by the ACF plots for observations on 2012 July 8 and 2013 April 23, respectively. The other ACF plots are noisy or do not indicate any variability timescale.

The soft and hard band LCs (left panel), HR plots (middle panel) and the DCF plots (right panel) are shown in Figure 3.3g and 3.3h. The HR plots are noisy, indicating no useful information. The DCFs for observations on 2012 July 8, 2013 July 16, and 2013 August 26 indicate zero lag correlations between the bands, while no significant correlations are found for other observations.

3.4.11 H 2356–309

The TeV HBL H 2356–309, located at $z = 0.165$ (Falomo, 1991), was discovered at X-rays by the Uhuru satellite (Forman et al., 1978) and subsequently, by HEAO A-1 (Wood et al., 1984). The X-ray (upto ~ 50 keV) spectrum of H 2356–309, during BeppoSAX observations, was found to be a broken power-law with a synchrotron peak at 1.8 ± 0.4 keV (Costamante et al., 2001). It was observed by HESS with an integral flux (at $E > 240$ GeV) of $(3.06 \pm 0.26_{stat} \pm 0.61_{syst}) \times 10^{-12}$ cm $^{-2}$ s $^{-1}$ (H.E.S.S. Collaboration et al., 2010).

NuSTAR observed H 2356–309 on 2016 May 18 for a good time exposure of 21.90 ks. As seen from the LC in Figure 3.1c the source shows a hint of variability. However, the data are both sparser and noisier, and the value of F_{var} is consistent

with no detectable IDV. Consequently, the ACF plotted in Figure 3.2c shows no IDV timescale.

The soft and hard LCs of H 2356–309 are plotted in the left panel of Figure 3.3h. The HR plot shown in the middle panel of that figure reveals no significant spectral change in the *NuSTAR* range. The DCF plot shown in the right panel of Figure 3.3h provides no useful information.

3.5 Discussion

3.5.1 X-ray Flux Variability

TeV Blazars monitored for sufficient times are known to exhibit strong flux variability with large amplitudes at all observable frequencies. Flux variations are understood to originate predominantly from the Doppler-boosted relativistic jets ([Marscher, 2014](#); [Calafut & Wiita, 2015](#)). However, the IDV and the STV for blazars in very low states can be produced by the instabilities or hot spots on the accretion disk (e.g. [Mangalam & Wiita, 1993](#); [Chakrabarti & Wiita, 1993](#)).

In this study of X-ray variability of TeV blazars using *NuSTAR*, we found the shortest hard X-ray variability timescales of 2.5 ks, 23.5, 8.0 and 29.6 ks for Mrk 421, 1ES 1218+304, Mrk 501, and PKS 2155–304, respectively. Such fast X-ray variations have been detected earlier in these sources (e.g. [Catanese & Sambruna, 2000](#); [Kataoka et al., 2000](#); [Cui, 2004](#)). The TeV variability timescales of a few minutes, as observed in PKS 2155–304 ([Aharonian et al., 2007c](#)) and Mrk 501 ([Albert et al., 2007](#)) are even lesser than the light crossing time of the Schwarzschild radius of the supermassive ($M \sim 10^6 - 10^9 M_{\text{sun}}$) black holes, which indicate that the emitting region is very compact. However, the physical requirement that the TeV emission will escape such a compact emitting region without being absorbed with the synchrotron photons via pair creation implies that the Lorentz factor (Γ) of the region must be $\gtrsim 50$ (e.g. [Gopal-Krishna et al., 2006](#); [Begelman et al., 2008](#)). But much lower values of Γ have been reported in these blazars from the study of slow apparent motions of their radio knots (e.g. [Piner & Edwards, 2004](#); [Giroletti et al., 2004](#)).

This apparent contradiction can be avoided by using models that include ratio and TeV emission regions with different properties. For example, the “needle” model,

3. X-RAY FLUX AND SPECTRAL VARIABILITY OF TEV BLAZARS WITH *NUSTAR*

proposed by Ghisellini & Tavecchio (2008), which can explain the origin of “orphan” flares (TeV flares without any contemporaneous X-ray flare) through the localized magneto-centrifugal acceleration of electron beams making small pitch angles from the magnetic field lines. However, in 2013 April a very fast (~ 14 minutes) X-ray variability is seen in the 3–79 keV LCs of Mrk 421 (Paliya et al., 2015), which is accompanied by the VHE $\gamma - ray$ variations (Cortina & Holder, 2013). So the “needle” model can not explain the 2013 April flare of Mrk 421. Those outbursts can, however, be interpreted through the magnetic reconnections using the “jets-in-a-jet” model given by Giannios et al. (2009). This model interprets fast TeV variability along with rapid variations at the X-ray frequencies as due to the relativistic outflow of material from the multiple magnetic reconnection regions within the jet through synchrotron-self-Compton.

3.5.2 Constraints on Physical Parameters using X-ray Variability Timescale

Assuming that the dominant origin of hard X-ray emission in TeV HBLs is the synchrotron emission, we can estimate certain parameters in a fashion that is independent of the details of the acceleration models. The synchrotron cooling timescale of an electron with energy $E = \gamma m_e c^2$ in the observer’s frame is given by (Zhang et al., 2002)

$$t_{cool}(\gamma) \simeq 7.74 \times 10^8 \frac{(1+z)}{\delta} B^{-2} \gamma^{-1} \text{s}, \quad (3.13)$$

where δ is the bulk Doppler factor, γ is the electron Lorentz factor and B is the magnetic field strength in Gauss (G).

For a given electron Lorentz factor and the magnetic field strength the synchrotron frequency is, (e.g. Paliya et al., 2015),

$$\nu \equiv \nu_{19} \times 10^{19} \text{Hz} \simeq 4.2 \times 10^6 \frac{\delta}{1+z} B \gamma^2, \quad (3.14)$$

where $0.08 < \nu_{19} < 2$ for X-rays in the *NuSTAR* energy range. Combining these two equations and applying the physical requirement that the synchrotron cooling timescale has to be smaller than or equal to the observed minimum variability timescale, we get for Mrk 421 (with minimum $t_{var} = 2500$ s and $z = 0.031$),

$$B \geq 0.35 \delta^{-1/3} \nu_{19}^{-1/3} \text{G}. \quad (3.15)$$

Table 3.6: Different model parameters for *NuSTAR* TeV HBLs

Blazar	t_{var} (s)	δ	B (G)	γ	R (cm)
Mrk 421	2500	25	≥ 0.12	$\leq 9.0 \times 10^5$	$\leq 1.8 \times 10^{15}$
1ES 1218+304	23510	20	≥ 0.03	$\leq 2.2 \times 10^6$	$\leq 1.2 \times 10^{16}$
Mrk 501	8000	15	≥ 0.07	$\leq 1.5 \times 10^6$	$\leq 3.5 \times 10^{15}$
PKS 2155–304	29600	30	≥ 0.02	$\leq 2.0 \times 10^6$	$\leq 2.4 \times 10^{16}$

We note that this expression of magnetic field strength has different dependences on δ and ν_{19} than does the Eq. 5 in [Paliya et al. \(2015\)](#). Assuming $\nu_{19} = 1$ and $\delta = 25$ (e.g., [Baloković et al., 2016](#)), we get,

$$B \geq 0.12G. \quad (3.16)$$

Using Equation 3.14, the electron Lorentz factor can be constrained to

$$\gamma \leq 9 \times 10^5. \quad (3.17)$$

We can also constrain the characteristic size of the emitting region to

$$R \leq ct_{var}\delta/(1+z) \leq 1.8 \times 10^{15} cm. \quad (3.18)$$

Similarly, we can constrain these parameters for 1ES 1218+304, Mrk 501 and PKS 2155–304, where we have also found reasonable variability timescales from *NuSTAR* data, assuming $\nu_{19} = 1$ and using typical values for δ (e.g. [Kataoka et al., 2000](#); [Sato et al., 2008](#); [Furniss et al., 2015](#)). These are given in Table 3.6.

3.5.3 Correlation Between X-ray Emissions in Soft and Hard Energy Bands

We investigated for any possible correlation between X-ray emissions in the soft (3–10 keV) and hard (10–79 keV) energy bands for each TeV blazar using the DCF. We found positive correlations with zero time lag for Mrk 421 (in all 22 observations), for Mrk 501 (in 3 out of 4), for 1ES 1959+650 (in 1 out of 2) and for PKS 2155–304 (in 3 out of 9). These positive correlations indicate that the soft and hard X-ray emissions from these TeV HBLs are produced by the same populations of electrons. However, the DCF plots for 1ES 0229+200, 1ES 0347–121, 1ES 0414+009, RGB J0710+591, 1ES 1101–232, 1ES 1218+304 and H 2356–309 are almost flat, which indicate either of two possibilities in case of

3. X-RAY FLUX AND SPECTRAL VARIABILITY OF TEV BLAZARS WITH *NUSTAR*

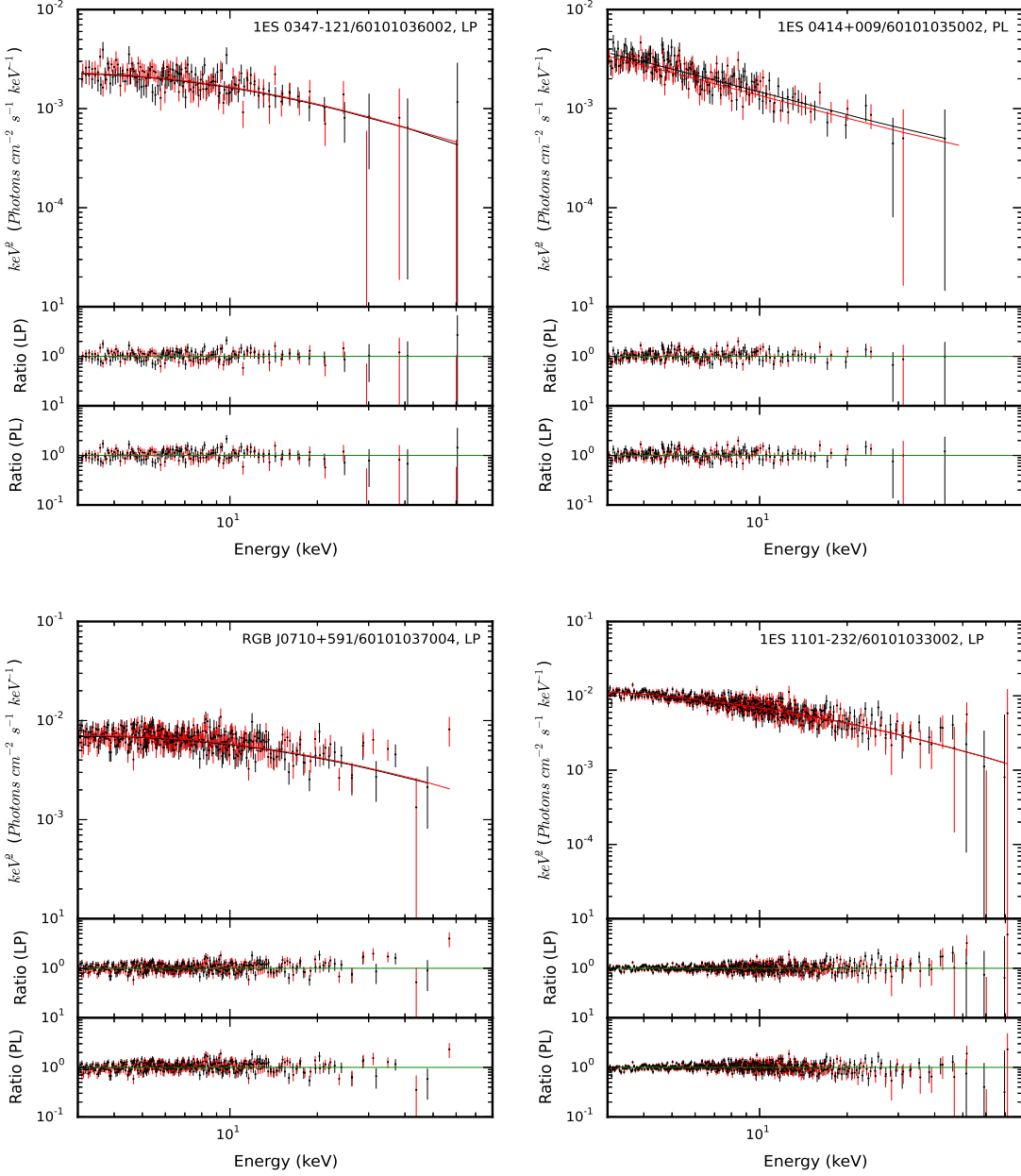


Figure 3.5a: Model-fitted *NuSTAR* spectra (black points are for FPMA and red points are for FPMB) of TeV HBLs 1ES 0347–121, 1ES 0414+009, RGB J0710+591, and 1ES 1101–232 in the upper panels and the data-to-model ratios for both the models tested in the bottom two panels. The blazar name, observation ID, and the best fitting model (LP or PL) are given in each plot.

these TeV blazars. The first possibility is that the soft and hard band X-ray emissions are actually uncorrelated, which could indicate that different electron populations are responsible for the production of X-ray emissions in these two bands. The second and more likely interpretation for the absence of correlations is that the data are too noisy, particularly in the hard X-ray LCs, to reveal any actual probable correlations between these two energy bands for these sources.

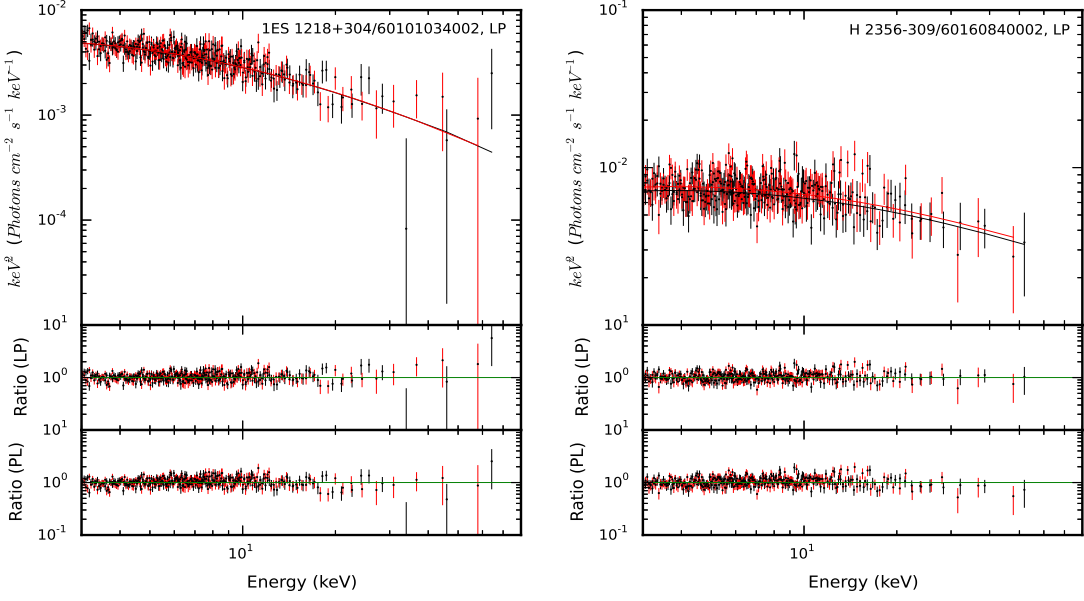


Figure 3.5b: As in Figure 3.5a, but for 1ES 1218+304 and H 2356–309.

3.5.4 X-ray Spectra

We performed the HR analyses to search for spectral changes in the *NuSTAR* energy range for each TeV HBLs. It has been found in several studies that for TeV HBLs the HR usually increases with increasing count rates, a behavior known as “harder when brighter” (e.g. Brinkmann et al., 2003; Ravasio et al., 2004). In our study, we found the “harder when brighter” behavior only in case of Mrk 421 and Mrk 501. While for rest nine TeV HBLs the HR plots show no significant variations, indicating that during these observations we could not find any variability in the X-ray spectra of these TeV HBLs (Zhang, 2008). This negative result could easily arise due to the low X-ray count rates for these HBLs.

We also performed spectral fits using *XSPEC* to investigate the shape of the *NuSTAR* spectra, shown in Figures 3.5a and 3.5b, of six TeV HBLs; 1ES 0347–121, 1ES 0414+009, RGB J0710+591, 1ES 1101–232, 1ES 1218+304 and H 2356–309 that were not studied earlier. We first used the simple PL model, which has two free parameters; a photon index (Γ) and the normalization. As it has been claimed in several studies that the X-ray spectra of HBLs are usually curved and well represented by the LP model (e.g. Massaro et al., 2004; Tramacere et al., 2007), we also tried to fit the *NuSTAR* spectra with the LP model. The LP model has the photon index (α) at fixed energy (E_{pivot}), the curvature (β) and the normalization as its three free parameters. In case of the LP model, the photon index varies as the logarithm of the energy.

3. X-RAY FLUX AND SPECTRAL VARIABILITY OF TEV BLAZARS WITH *NUSTAR*

To compare the PL and LP model fits to *NuSTAR* spectra, we performed F -tests. The null hypothesis is that the simpler model, PL in our case, provides the better fit. We found that the PL model provides a better fit over the LP model only for 1ES 0414+009, while for the other five HBLs the LP model provides a better fit, as can be seen from the high values of F-statistics and the corresponding probabilities ($> 99\%$), given in Table 3.5. The *NuSTAR* spectra of five TeV HBLs 1ES 0347–121, RGB J0710+591, 1ES 1101–232, 1ES 1218+304 and H 2356–30 are described well by the curved LP models with $\alpha \simeq 2.23 – 2.67$ and the spectral curvature β lying in the range 0.27–0.43. However, the *NuSTAR* spectra of 1ES 0414+009 is better represented by a steep PL model with photon index $\simeq 2.77$. The model-fitted *NuSTAR* spectra together with the data-to-model ratio for these six TeV HBLs are plotted in Figures 3.5a and 3.5b.

The spectral shape of X-ray emissions of TeV HBLs provides information about the particles acceleration mechanism and the distribution of the emitting particles. The curved X-ray spectra of BL Lac objects can be interpreted in terms of energy-dependent particle acceleration and the subsequent radiative cooling (Massaro et al., 2004). Thus, this study of the shape of X-ray spectra of TeV HBLs can be used to understand the particle acceleration in these BL Lac objects.

3.6 Conclusions

In this chapter, we examined the 46 X-ray LCs of the eleven TeV HBLs that have been observed with *NuSTAR* for intraday flux and spectral variability. We also searched for possible variability timescales using the discrete autocorrelation analyses. We found significant IDV in the LCs of 1ES 1101–232 (in 1 of 1 LC); Mrk 421 (in all 22 of 22 LCs); 1ES 1218+304 (in 1 of 1 LC); Mrk 501 (in 3 of 4 LCs); 1ES 1959+650 (in 1 of 2 LCs) and PKS 2155–304 (in 7 of 9 LCs).

Using ACFs, we found evidences for variability timescales ranging from 2.5 to 32.8 ks in eight 3–79 keV LCs of Mrk 421, a timescale of 23.5 ks in one LC of 1ES 1218+304, a timescale of 8.0 ks in one LC of Mrk 501, and timescales of 29.6 and 57.4 ks in two LCs of PKS 2155–304. No timescale of variability is clearly seen in rest 34 LCs. Using the minimum observed variability timescales, we constrained the values of the magnetic field strength (B), electron Lorentz factor (γ) and the characteristic size (R) of emitting regions for Mrk 421, 1ES 1218+304, Mrk 501, and PKS 2155–304, given in Table 3.6.

We employed an HR analysis to perform a preliminary study of the X-ray spectral variability of these eleven TeV HBLs. We found that the 3–79 keV spectra become harder with increasing count rates for Mrk 421 and Mrk 501. Using DCF analysis, we searched for a correlation between the soft (3–10 keV) and hard (10–79 keV) band LCs. We found positive correlations with zero time lag for Mrk 421 (in all 22 observations), for Mrk 501 (in 3 out of 4), for 1ES 1959+650 (in 1 out of 2) and for PKS 2155–304 (in 7 out of 9), indicating that the X-ray emissions in the two energy bands from these TeV HBLs are produced by the same electron populations.

We also investigated the shape of the X-ray spectra of six TeV HBLs by applying the PL and LP models. The *NuSTAR* spectra of 1ES 0414+009 can be fitted well with a PL model, while the spectra of the rest five TeV HBLs 1ES 0347–121, RGB J0710+591, 1ES 1101–232, 1ES 1218+304 and H 2356–309 are curved and are better represented by LP model.

Chapter 4

Optical Flux and Spectral Variability of TeV Blazars

4.1 Introduction

In the previous chapter, we studied X-ray (3–79 keV) flux and spectral variability of TeV blazars on IDV timescales using *NuSTAR* satellite. In order to compare the variability properties of TeV blazars at X-ray and optical frequencies, we performed optical photometric observations of the TeV blazars using ground-based telescopes. At optical wavelengths, the first clear IDV was detected in the LCs of BL Lacertae by Miller et al. (1989). Since then the optical variability on diverse timescales in the LCs of blazars has been reported in several studies (e.g., Carini, 1990; Heidt & Wagner, 1996; Fan et al., 2001; Xie et al., 2002; Stalin et al., 2005; Gupta et al., 2008b; Gaur et al., 2012a; Bachev et al., 2012; Gaur et al., 2012b; Agarwal & Gupta, 2015; Agarwal et al., 2016; Gupta et al., 2016). It has been found that at optical wavelengths HBLs are less variable than LBLs and also their variability amplitudes are much smaller than that of LBLs (Heidt & Wagner, 1998). Flux variations at optical frequencies are generally accompanied by color variations. In general, BL Lac objects follow a bluer-when-brighter (BWB) trend while a redder-when-brighter (RWB) trend is found in FSRQs (e.g., Fan & Lin, 2000; Gu et al., 2006; Wu et al., 2012; Wierzcholska et al., 2015).

¹A part of the Work presented in this chapter has been published in Pandey et al. (2019), ApJ, 871, 192

4. OPTICAL FLUX AND SPECTRAL VARIABILITY OF TEV BLAZARS

In the present chapter, we report our results of optical variability studies of a sample of five TeV HBLs (1ES 0229+200, 1ES 0414+009, 1ES 0806+524, 1ES 1553+113, and 1ES 2344+514) using two Indian optical telescopes during 2016–2018. We examined the optical LCs of these TeV HBLs for intraday variations using the two most powerful statistical tests: the power-enhanced F -test and the nested analysis of variance (ANOVA) test. We observed the blazars 1ES 0229+200, 1ES 0414+009, and 1ES 2344+514 for 2 – 5 hr in optical R band to search for IDV. For the blazars 1ES 0806+524, and 1ES 1553+113 we have quasi-simultaneous observations in V and R bands for 2 – 5 hr which gave us the opportunity to also study their color variations. One set of observations in B , V , R , and I bands were also performed for each blazar to study their day to day variations at multiple optical wavelengths.

The outline of the chapter is as follows. We briefly describe the observations and data processing in Section 4.2 and discuss the techniques used to search for IDV flux and color variations in Section 4.3. Section 4.4 presents the results of our optical photometric study. A detailed discussion and our conclusions are given in Section 4.5.

Table 4.1: Right Ascension, Declination and Redshift of the observed TeV Blazars.

Blazar Name	RA (α_{2000})	Dec (δ_{2000})	Redshift (z)
1ES 0229+200	02 ^h 32 ^m 53 ^s	+20°16'21"	0.140
1ES 0414+009	04 ^h 16 ^m 53 ^s	+01°05'20"	0.287
1ES 0806+524	08 ^h 09 ^m 49 ^s	+52°18'58"	0.138
1ES 1553+113	15 ^h 55 ^m 43 ^s	+11°11'24"	0.500
1ES 2344+514	23 ^h 47 ^m 04 ^s	+51°42'18"	0.044

4.2 Observations and Data Reduction

The optical photometric observations of five TeV HBLs, listed in Table 4.1, were carried out in Johnson BV and Cousins RI filters between 2016 April 6 and 2018 December 29 using 1.3 m DFOT and 1.04 m ST, the details of telescopes and instruments used are given in Table 2.1. The complete observation log of these TeV blazars is given in Table 4.2.

The preprocessing (bias subtraction, flat-fielding, and cosmic-ray correction) of raw data is done using the standard routines of IRAF software. The cleaned data is, then, processed using the DAOPHOT II software. The method of optical

4.2 Observations and Data Reduction

Table 4.2: Observation log of optical photometric observations of TeV Blazars.

Observation date dd-mm-yyyy	Telescope	Data points B, V, R,I	Observation date dd-mm-yyyy	Telescope	Data points B, V, R,I
	1ES 0229+200		09–02–2018	B	1,25,25,1
24–10–2016	A	1, 1,40,1	21–02–2018	A	1,30,30,1
25–10–2016	A	1, 1,32,1	15–12–2018	A	1,30,30,1
26–10–2016	A	1, 1,30,1	16–12–2018	A	1,41,41,1
24–11–2016	A	1, 1,41,1	28–12–2018	A	0,34,34,1
25–11–2016	A	1, 1,50,1	29–12–2018	A	1,33,33,1
30–12–2016	A	1, 1, 1,1		1ES 1553+113	
18–01–2017	A	1, 1, 1,1	06–04–2016	A	1,28,28,1
19–01–2017	A	1, 1, 1,1	08–04–2016	B	0,20,20,1
11–10–2017	B	1, 1, 1,1	09–04–2016	B	0, 8, 8,1
15–11–2017	B	1, 1, 1,1	10–04–2016	B	0,16,16,1
13–12–2017	B	1, 1, 1,1	11–04–2016	B	0,20,20,1
09–01–2018	B	1, 1, 1,1	12–04–2016	B	0,21,21,1
10–01–2018	B	0, 1, 1,1	13–04–2016	B	0,18,18,1
21–02–2018	A	0, 1, 1,1	16–04–2016	A	1,19,19,1
10–10–2018	A	1, 1,42,1		1ES 2344+514	
15–10–2018	A	1, 1, 1,1	24–10–2016	A	1, 1, 1,1
15–12–2018	A	1, 1, 1,1	25–10–2016	A	1, 1,59,1
16–12–2018	A	1, 1, 1,1	26–10–2016	A	1, 1,70,1
28–12–2018	A	0, 1,34,1	08–11–2016	B	0, 1,41,1
29–12–2018	A	1, 1,47,1	09–11–2016	B	0, 0,34,1
	1ES 0414+009		24–11–2016	A	1, 1,70,1
30–12–2016	A	1, 1,35,1	25–11–2016	A	1, 1,60,1
18–01–2017	A	1, 2, 2,1	29–12–2016	A	1, 1,36,1
19–01–2017	A	1, 1,32,1	30–12–2016	A	1, 1, 1,1
13–12–2017	B	0, 1, 1,0	18–01–2017	A	1, 1, 1,1
21–02–2018	A	1, 1, 1,1	19–01–2017	A	1, 1, 1,1
01–11–2018	B	1, 1, 1,1	10–10–2018	A	1, 0,95,1
02–11–2018	B	1, 1, 1,1	11–10–2018	A	1, 1, 1,1
15–12–2018	A	1, 1,56,1	15–10–2018	A	1, 1,70,1
16–12–2018	A	1, 1,65,1	31–10–2018	B	1, 1, 1,1
28–12–2018	A	0, 1,30,1	01–11–2018	B	1, 1, 1,1
29–12–2018	A	1, 1,43,1	02–11–2018	B	1, 1, 1,1
	1ES 0806+524		15–12–2018	A	1, 1,60,1
30–12–2016	A	1,37,37,1	16–12–2018	A	1, 1,60,1
19–01–2017	A	1,27,27,1	28–12–2018	A	0, 1, 1,1
10–01–2018	B	1,20,20,1	29–12–2018	A	1, 1, 1,1
08–02–2018	B	1,25,25,1			

A : 1.30 m (f/4) Devasthal Fast Optical Telescope (DFOT)

B : 1.04 m (f/13) Sampuranand Telescope (ST)

4. OPTICAL FLUX AND SPECTRAL VARIABILITY OF TEV BLAZARS

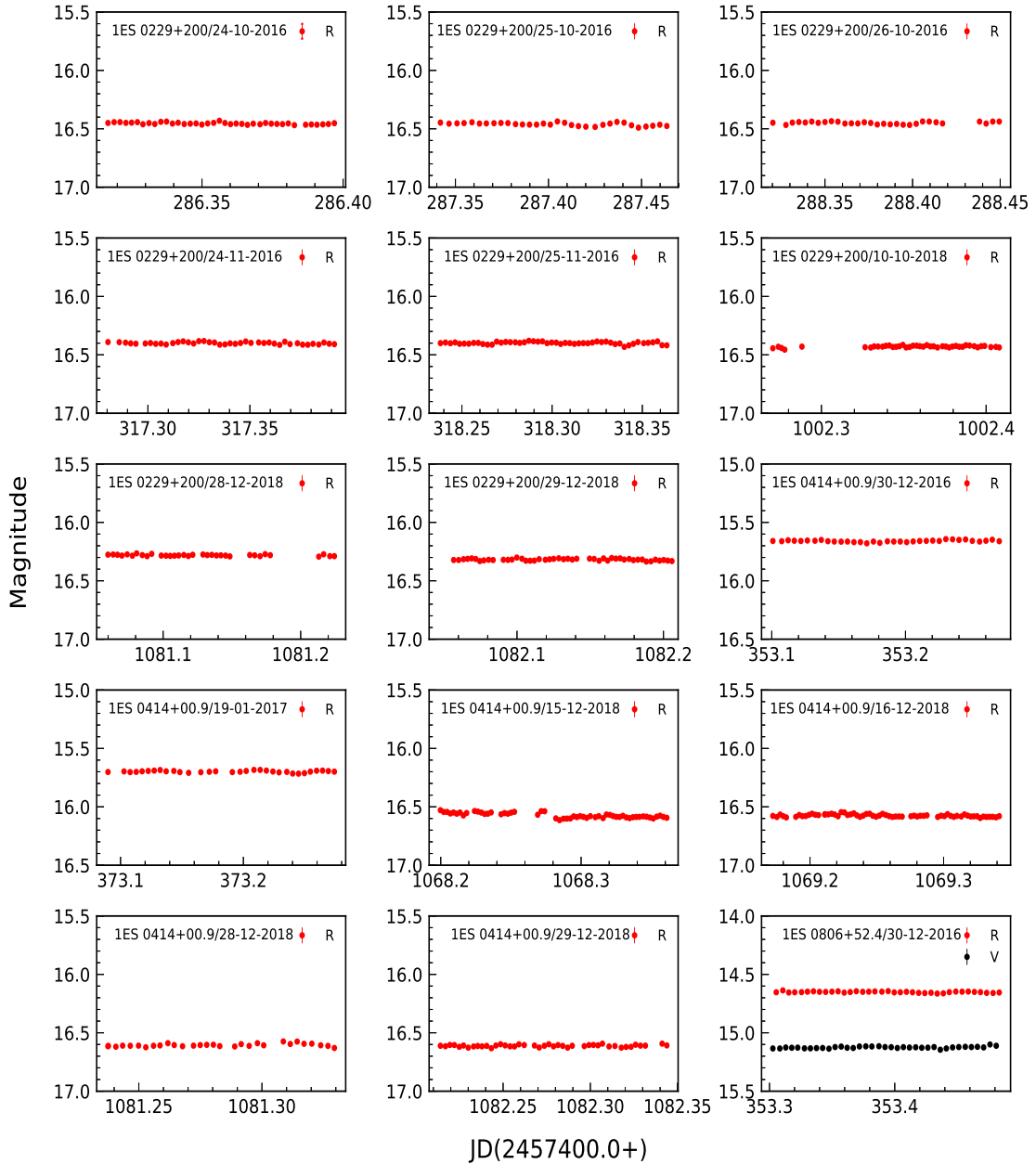


Figure 4.1a: Optical LCs of TeV HBLs 1ES 0229+200, 1ES 0414+009 and 1ES 0806+524. The blazar name and the observation date are given in each plot.

photometric data processing is explained in detail in Section 2.2.2. We selected two comparison stars, taken from the finding charts² of these blazars, to check their mutual non-variability. Finally, one comparison star with magnitude and color closer to that of the blazar is selected to get the calibrated magnitude of the blazar.

²<https://www.lsw.uni-heidelberg.de/projects/extragalactic/charts/>

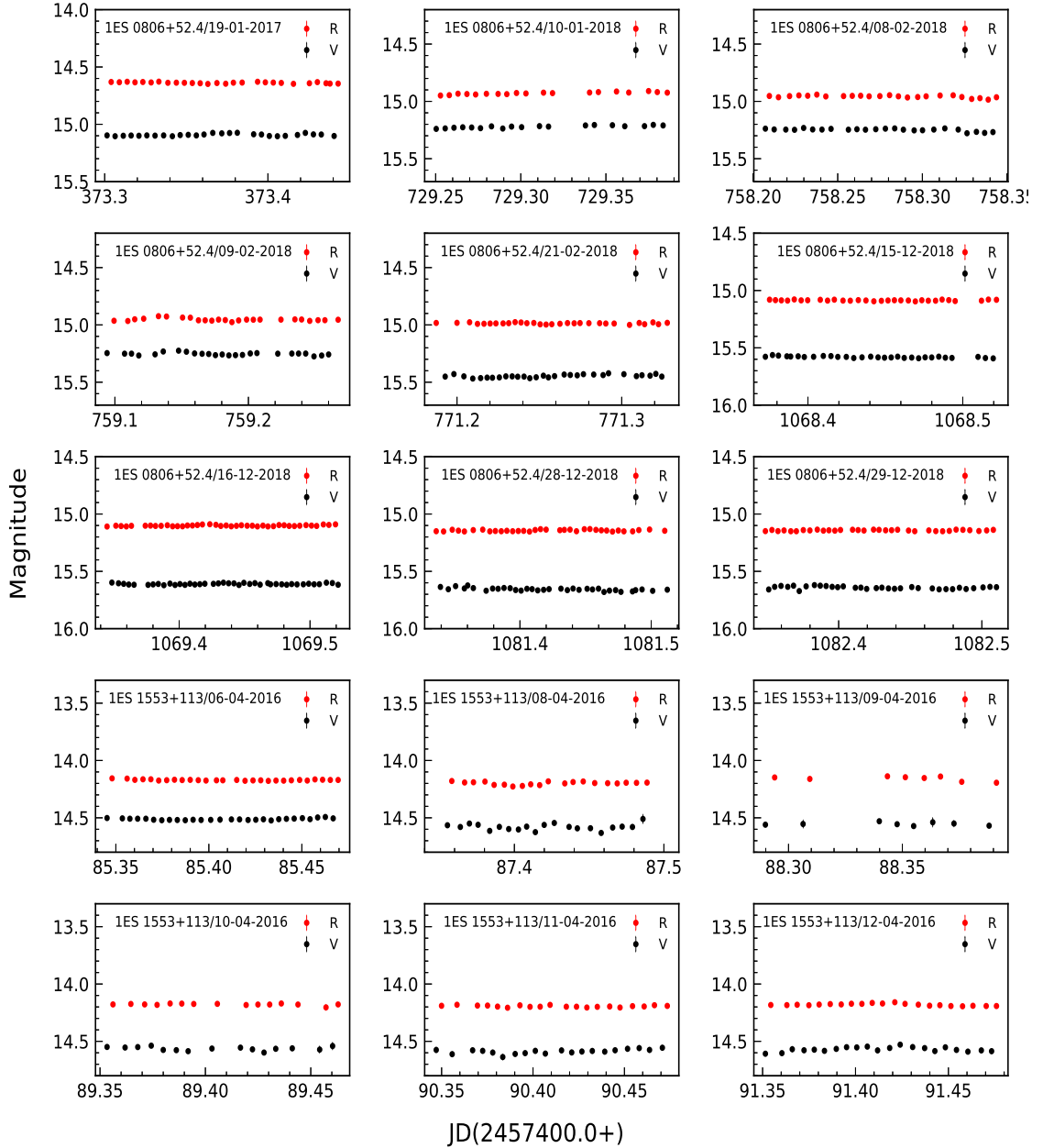


Figure 4.1b: Optical LCs of TeV HBLs 1ES 0806+524 and 1ES 1553+113. The blazar name and the observation date are given in each plot.

4. OPTICAL FLUX AND SPECTRAL VARIABILITY OF TEV BLAZARS

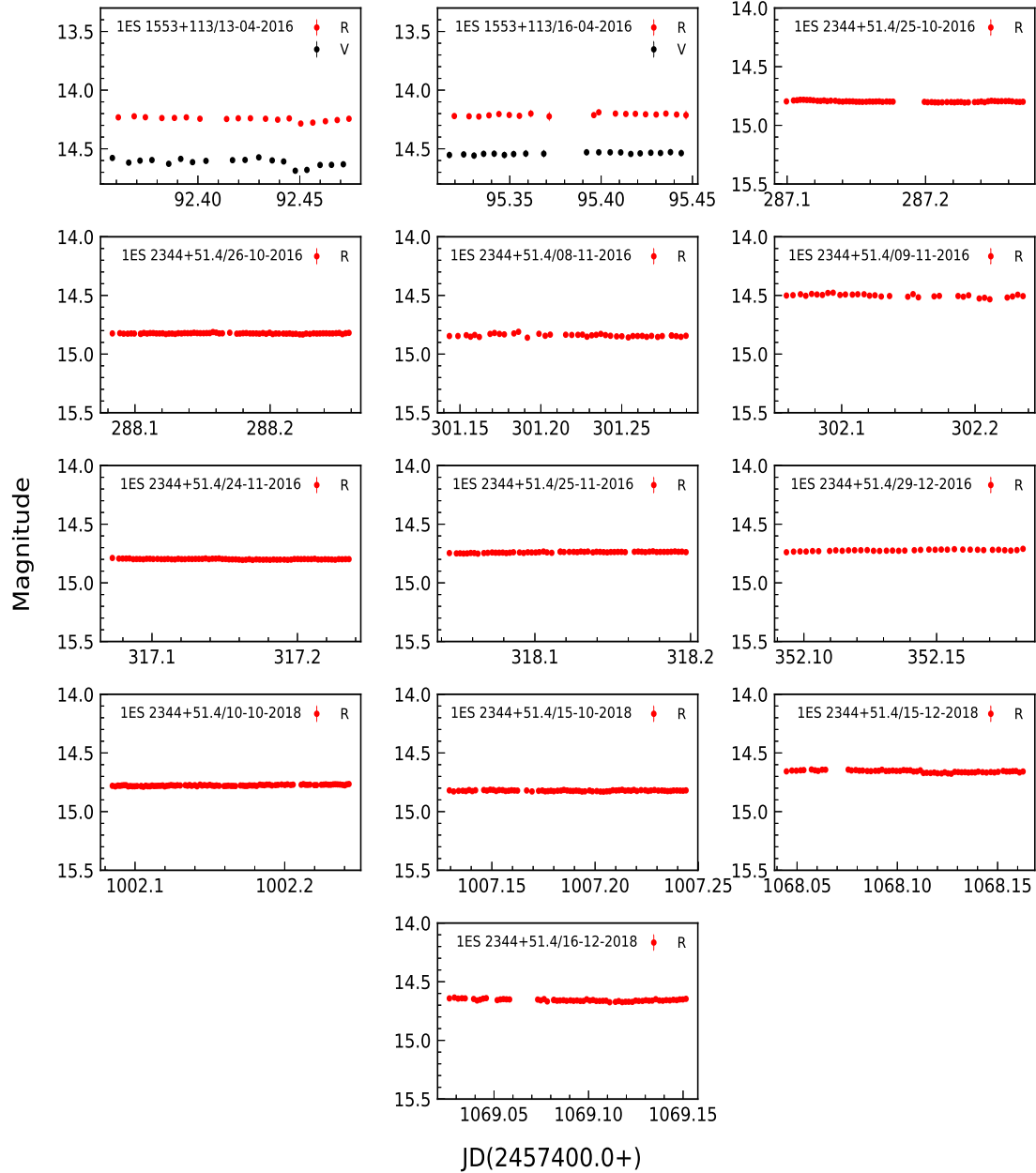


Figure 4.1c: Optical LCs of TeV HBLs 1ES 1553+113 and 1ES 2344+514. The blazar name and the observation date are given in each plot.

4.3 Analysis Techniques

We have examined the differential light curves (DLCs) of the TeV HBLs for IDV using the power-enhanced F -test and the nested ANOVA test, which have been argued to be more powerful and reliable than the widely used statistical tests such as C -test, χ^2 -test and the standard F -test (de Diego, 2014; de Diego et al., 2015). The basic principle of both the probes is to include several comparison stars in the analysis to increase the power of the probe. These two latest statistical tests are explained in the following subsections.

4.3.1 Power-enhanced F -test

The power-enhanced F -test compares the variance of the DLC of blazar to the combined variance of the DLCs of multiple comparison stars. To minimize the errors, we use the brightest comparison star as our reference star to generate DLCs. This test has been used for detecting microvariability in the blazar light curves in several recent studies (e.g., Gaur et al., 2015a; Polednikova et al., 2016; Kshama et al., 2017). The power-enhanced F -statistic is defined as (de Diego, 2014):

$$F_{enh} = \frac{s_{blz}^2}{s_c^2}, \quad (4.1)$$

where

$$s_c^2 = \frac{1}{(\sum_{j=1}^k N_j) - k} \sum_{j=1}^k \sum_{i=1}^{N_j} s_{j,i}^2, \quad (4.2)$$

and s_{blz}^2 is the variance of the DLC of blazar and s_c^2 is the combined variance of the DLCs of several comparison stars; N_i is the number of observations of the j th comparison star and k denote the total number of comparison stars. The scaled square deviation, $s_{j,i}^2$, for the j th star is computed as

$$s_{j,i}^2 = \omega_j (m_{j,i} - \bar{m}_j)^2, \quad (4.3)$$

where ω_j is a scaling factor (ratio of the averaged square error of the blazar DLC to the averaged squared error of the comparison star DLC (Joshi et al., 2011)) used to scale up the variance of j th comparison star to the level of the blazar, $m_{j,i}$ and \bar{m}_j are the differential magnitude and the mean magnitude of the comparison star DLC, respectively.

4. OPTICAL FLUX AND SPECTRAL VARIABILITY OF TEV BLAZARS

Since the number of observations for the blazar and the comparison stars are same (N), the number of degrees of freedom in the numerator in the F - statistics is $\nu_1 = N - 1$ and that in the denominator is $\nu_2 = k(N - 1)$. We, then, compare the F_{enh} value, estimated using Equation 4.1, with the critical value (F_c) at $\alpha = 0.01$ (99% confidence level) to search for IDV in the LCs. A light curve is declared as variable (V) if $F_{enh} \geq F_c$, otherwise it is non-variable (NV).

4.3.2 Nested ANOVA

The ANOVA family tests compare the dispersion of means between the groups of observations. In nested ANOVA test, which is an updated two-stage ANOVA test, we can use all the comparison stars as reference stars to generate DLCs of the blazar, so we will have one more star in the analysis in comparison to the power-enhanced F -test where we have to take the brightest star as reference star and rest as the comparison stars. The functional procedure of the nested ANOVA test is given below:

If y_{ijk} is the differential magnitude of blazar extracted using the reference star $k = 1, 2, \dots, n$, within the image $j = 1, 2, \dots, b$ of the group $i = 1, 2, \dots, a$ then we can express y_{ijk} as (e.g., [de Diego et al., 2015](#))

$$y_{ijk} = \mu + \gamma_i + \omega_{j(i)} + \epsilon_{ijk}, \quad (4.4)$$

where μ is the mean of the entire blazar differential light curve, γ_i is the deviation from the mean of the i th group, $\omega_{j(i)}$ is the deviation of the j th image nested under the i th group from the mean of the i th group and ϵ_{ijk} is the measurement error.

One can write the total sum of squares (SS) as (e.g., [de Diego et al., 2015](#))

$$\begin{aligned} \sum_{i=1}^a \sum_{j=1}^b \sum_{k=1}^n (y_{ijk} - \bar{y})^2 &= bn \sum_{i=1}^a (\bar{y}_i - \bar{y})^2 \\ &\quad + n \sum_{i=1}^a \sum_{j=1}^b (\bar{y}_{ij} - \bar{y}_i)^2 \\ &\quad + \sum_{i=1}^a \sum_{j=1}^b \sum_{k=1}^n (y_{ijk} - \bar{y}_{ij})^2 \end{aligned} \quad (4.5)$$

where \bar{y} is the overall mean of the blazar light curve, $\bar{y}_i = (\sum_{j=1}^b \sum_{k=1}^n y_{ijk})/bn$ and $\bar{y}_{ij} = \sum_{k=1}^n y_{ijk}/n$. Equation (5) can be symbolically written as

$$SS_{Total} = SS_{Group} + SS_{O(G)} + SS_{Error}. \quad (4.6)$$

The numbers of degrees of freedom are $abn - 1$ for SS_{Total} , $a - 1$ for SS_{Group} , $a(b - 1)$ for $SS_{O(G)}$ (which is the sum of squares due to nested images in the groups) and $ab(n - 1)$ for SS_{Error} . When we divide a sum of squares (SS) by its degrees of freedom, it gives mean square (MS), and the ratio of the two mean squares follows an F distribution. In this nested ANOVA test, we compare the variances of means between the groups to the variances of means within the groups to search for variability in the differential light curve of the source. So, the F -statistic is

$$F = \frac{MS_{Group}}{MS_{O(G)}} = \frac{SS_{Group}/(a - 1)}{SS_{O(G)}/a(b - 1)} \quad (4.7)$$

with $a - 1$ and $a(b - 1)$ degrees of freedom.

In our case, each group has five observations ($b = 5$) for each blazar. A light curve is taken as variable (V) if the F -statistic, calculated from Equation 4.7, \geq the critical value (F_c) at $\alpha = 0.01$, otherwise non-variable (NV).

The results of the F_{enh} -tests and nested-ANOVA tests are given in Table 4.3. In it, a light curve is considered as variable (V) only if significant variations were found by both the tests, otherwise, we conservatively declare it non-variable (NV).

4.3.3 Intraday Variability Amplitude

We have calculated the amplitude (Amp) of IDV in percent using the calibrated light curves of the blazars as follows (Heidt & Wagner, 1996).

$$Amp = 100 \times \sqrt{(A_{max} - A_{min})^2 - 2\sigma^2}, \quad (4.8)$$

where A_{max} and A_{min} denote the maximum and minimum magnitudes, respectively, of the blazar and σ is the mean measurement error.

4. OPTICAL FLUX AND SPECTRAL VARIABILITY OF TEV BLAZARS

4.4 Results

4.4.1 Flux Variability

4.4.1.1 1ES 0229+200

1ES 0229+200 was first detected in X-rays in the *Einstein* satellite's IPC (Elvis et al., 1992) and later classified as a BL Lac object, because of its featureless optical spectrum Schachter et al. (1993). It is now listed as a HBL on the basis of its X-ray to radio flux ratio (Giommi et al., 1995). The blazar 1ES 0229+200 is hosted by an elliptical galaxy at a redshift of $z = 0.1396$ (Woo et al., 2005). It was observed on 184 nights during 2007–2012 by Wierzcholska et al. (2015). They found very slight variation of ~ 0.2 mag in its brightness and very steep optical continuum with $\alpha_{BR} > 3.7$.

We monitored the blazar 1ES 0229+200 for a total of 20 nights from 2016 October 24 to 2018 December 29. During 8 of those nights, we observed the TeV HBL 1ES 0229+200 continuously in R band for 2–4 hr to investigate variability properties on IDV timescales. The IDV LCs of 1ES 0229+200 are plotted in Figure 4.1a.

Using the power-enhanced F -test and nested ANOVA test we examined these LCs for IDV, results are given in Table 4.3. We found no significant variations on IDV timescales on any of those nights.

The ~ 2 yr LCs in B and R bands for 1ES 0229+200 are shown in the upper panel of Figure 4.2a. Clear variations in both bands can be seen during the entire monitoring period. The TeV HBL 1ES 0229+200 was found in the brightest state of $R_{mag} = 16.176$ on 2017 November 15 while the faintest magnitude observed was $R_{mag} = 16.540$ on 2017 January 18. The mean magnitudes in B and R filters were 17.447 and 16.395, respectively.

4.4.1.2 1ES 0414+009

The blazar 1ES 0414+009 was initially discovered as an X-ray source associated with a cluster of galaxies (Ulmer et al., 1980) and later classified as a BL Lac object (Ulmer et al., 1983). The redshift of 1ES 0414+009 is $z = 0.287$ (Halpern et al., 1991), derived from the weak steller absorption lines. McHardy et al. (1992) reported $R = 16.64$ and $V = 17.21$ from observations during 1986 and 1987. 1ES

0414+009 was monitored from 1996 October – 1997 February by [Raiteri et al. \(1998\)](#) with R –mag ranges from 16.18 to 16.40. [Kapanadze \(2009\)](#) observed this BL Lac during 1997 October – 2007 February on 56 nights. No IDV was found and the R brightness varied from 15.86 to 16.92 during this period. The brightness variation of ≤ 1 mag and spectral index $\alpha_{BR} \sim 0.7 – 1.3$ were reported from observations on 285 nights in 2007-2012 by [Wierzcholska et al. \(2015\)](#).

We observed the TeV HBL 1ES 0414+009 in B , V , R , and I bands on 11 nights during 2016 December 30 to 2018 December 29. We monitored the blazar in R band for 2.2–4.5 hr on 6 of those nights to study variations on IDV timescales. The R band IDV LCs of 1ES 0414+009 are plotted in Figure 4.1a.

We examined the IDV LCs of the blazar 1ES 0414+009 for variability on intraday timescales and found no strong evidence of IDV in any of the LCs. The results of the statistical tests are given in Table 4.3.

The ~ 2 yr LCs of 1ES 0414+009 in V , R , and I bands, shown in the Figure 4.2b, clearly indicate variations at all the three optical bands. During our observing period, the average magnitudes of 1ES 0414+009 in V , R , and I filters were 16.621, 16.395, and 15.712, respectively. We observed the brightest magnitude of $R_{mag} = 15.633$ on 2017 January 18 while the faintest magnitude recorded was $R_{mag} = 16.632$ on 2018 December 29.

4.4.1.3 1ES 0806+524

1ES 0806+524 was classified as a BL Lac object on the basis of its featureless optical spectra ([Schachter et al., 1993](#)). It was first detected at VHE ($E > 300$ GeV) γ -ray in 2008 by VERITAS ([Acciari et al., 2009a](#)). [Kapanadze \(2009\)](#) observed this blazar from 2002 to 2004 and found an overall variation of $\Delta R = 0.90$ with a maximum R-band magnitude of $R = 14.72$, but no intra-day variations were detected. [Gopal-Krishna et al. \(2011\)](#) monitored this blazar on 4 nights but didn't find IDV on any night. The quasi-simultaneous multicolor observations of 1ES 0806+524 were performed from 2005 December to 2011 February by [Man et al. \(2014\)](#) and they found strong BWB trend on long timescales, but no variation on IDV timescales.

We performed quasi-simultaneous observations of the TeV HBL 1ES 0806+524 in V and R bands for 10 nights during 2016 December 30 to 2018 December 29. The IDV LCs of the blazar 1ES 0806+524 are plotted in Figures 4.1a and 4.1b.

4. OPTICAL FLUX AND SPECTRAL VARIABILITY OF TEV BLAZARS

We statistically examined the LCs for IDV using the power-enhanced F -test and nested ANOVA test. The results of these statistical tests are given in Table 4.3. Significant IDV was found in both V and R bands only on 2018 January 10, while no significant IDV was detected at any band on rest of the nights. We found the variability amplitudes of 3.46% and 3.88% in V and R bands, respectively.

The 2 yr LCs of the TeV HBL 1ES 0806+524 in V , R , and I bands are shown in the upper panel of Figure 4.2c. Clear variations can be seen at all three optical bands. The average magnitudes recorded were 15.409, 14.940, and 14.628 in V , R , and I bands, respectively. During our monitoring period the brightest state of the blazar 1ES 0806+524 was observed on 2017 January 19 with $R_{mag} = 14.628$ while the faintest state was recorded on 2018 December 28 with $R_{mag} = 15.153$.

4.4.1.4 PG 1553+113

PG 1553+113 (1ES 1553+113) was first detected as a BL Lac object in the Palomar–Green survey of ultraviolet-excess objects (Green et al., 1986). It is identified as a BL Lac object due to its featureless optical spectrum (Miller & Green, 1983) and significant ($\Delta m \sim 1.9$ mag) optical variations (Miller et al., 1988). It is a HBL (Falomo & Treves, 1990) at a red-shift of $z \sim 0.5$ (Danforth et al., 2010; Abramowski et al., 2015). The ratio of X-ray to radio flux ($\log(F_{2keV}/F_{5GHz})$) of TeV blazar PG 1553+113 ranges from -4.37 to -3.88 (Osterman et al., 2006), indicating that it is an extreme HBL (Rector et al., 2003). Its optical spectral index was reported to be nearly constant ($\alpha \sim -1^3$) during 1986–1991 with a maximum variation of 0.24 by Falomo et al. (1994). It was detected in the bright state with average $R_{mag} \sim 13.3$ during 2010 March–August by Gaur et al. (2012b). Recently, Gupta et al. (2016) detected PG 1553+113 with $m_R \sim 13.81 - 14.40$ and $m_V \sim 14.17 - 14.71$ in a multi-band optical study of TeV blazars.

We observed the TeV blazar PG 1553+113 quasi-simultaneously in V and R bands for a total of 8 nights from 2016 April 6–16. Visual inspection of the calibrated V and R band IDV LCs of PG 1553+113, plotted in the Figures 4.1b and 4.1c, indicates IDV on a couple of nights.

We used the two statistical tests discussed in Sections 4.3.1 and 4.3.2 to examine the V and R band LCs for IDV. The results of these tests are given in Table 4.3. We found significant IDV in both V and R band LCs of PG 1553+113 only on April 13, while no significant IDV was detected at any band on April 6, 9, 10,

³Using the convention, $F_\nu \propto \nu^\alpha$

11, and 16. We also detected significant variations in R band LCs on April 8 and 12, although no significant variability in the V band LCs on those nights was observed. However, notice that the errors in V band LCs are roughly twice as large, and therefore reduce the chance of detecting any small fluctuations that might be present. We also found that the variability amplitude was smallest (3.44%) in R band on April 12, while the largest (11.23%) variation was detected in V band on April 13.

The STV LCs of PG 1553+113 in V , R and I bands, plotted in the upper panel of Figure 4.2d, clearly indicate STV variations at all three optical wavelengths. To make the variability pattern visible, the V and I band LCs are shifted by -0.2 and $+0.2$ magnitudes, respectively. During our observing period, the source was found in the brightest state of $R_{mag} = 14.138$ on April 9, while the faintest magnitude observed was $R_{mag} = 14.285$ on April 13. The mean magnitudes were 14.563, 14.193, and 13.713 in V , R , and I bands, respectively.

4.4.1.5 1ES 2344+514

1ES 2344+514 was identified as a BL Lac object at a redshift of $z = 0.044$ ([Perlman et al., 1996](#)). It was discovered as a TeV source with the Whipple Observatory γ -ray telescope, making it the third BL Lac object, after Mrk 421 and Mrk 501, to be detected at VHE ([Catanese et al., 1998](#)). At X-ray, rapid variability on a timescale of ~ 5000 s has been reported by [Giommi et al. \(2000\)](#). [Miller et al. \(1999\)](#) reported positive detection of microvariability in the optical LCs of 1ES 2344+514. [Xie et al. \(2002\)](#) and [Fan et al. \(2004\)](#), separately, observed the blazar in 2000, but didn't find any significant IDV. A considerable microvariability with the variability amplitude $\Delta R = 0.69 \pm 0.16$ on a timescale of $\Delta t = 4738$ was detected on 2005 December 28 by [Ma et al. \(2010\)](#). [Gaur et al. \(2012a\)](#) monitored the TeV BL Lac 1ES 2344+514 on 19 nights from 2009 August to 2010 July, but found no variation on IDV and STV timescales.

We performed the optical photometric observations of the TeV blazar 1ES 2344+514 on 21 nights from 2016 October 24 to 2018 December 29. We observed the blazar in R band for $2.1 - 4.6$ hr on 11 out of those nights to examine flux variations on IDV timescales. Visual inspection of the IDV LCs of 1ES 2344+514, plotted in Figure 4.1c, indicates no IDV on any of those nights.

To statistically examine the LCs for IDV, we performed the power-enhanced F -test and nested ANOVA test. The results of these tests are given in Table 4.3. We

4. OPTICAL FLUX AND SPECTRAL VARIABILITY OF TEV BLAZARS

found a hint of IDV only on 2018 October 10, but the variability amplitude is only 2.26 % which is below 3σ level. Therefore, no significant IDV was found on any of the IDV LCs of 1ES 2344+514.

The LCs of the TeV HBL 1ES 2344+514 in V , R , and I bands for our entire monitoring period are shown in Figure 4.2e, which show clear variations in all three bands. The average magnitudes in V , R , and I bands were 15.294, 14.752, and 13.985, respectively. During our monitoring period the source was recorded in the brightest state on 2016 November 9 with $R_{mag} = 14.477$, while in the faintest state on 2017 January 18 with $R_{mag} = 14.876$.

Table 4.3: Results of IDV analyses of TeV Blazars

Blazar Name	Observation date	Band	Power-enhanced F -test			Nested ANOVA			Status	Amplitude %
			DoF(ν_1, ν_2)	F_{enh}	F_c	DoF(ν_1, ν_2)	F	F_c		
1ES 0229+200	24-10-2016	R	39,195	0.40	1.71	7, 32	1.59	3.26	NV	-
	25-10-2016	R	31,155	2.04	1.81	5, 24	3.54	3.90	NV	-
	26-10-2016	R	29,145	1.24	1.84	5, 24	4.21	3.90	NV	-
	24-11-2016	R	40,200	0.30	1.69	7, 32	8.82	3.26	NV	-
	25-11-2016	R	49,245	1.28	1.62	9, 40	4.90	2.89	NV	-
	10-10-2018	R	41,205	0.89	1.68	7, 32	2.48	3.26	NV	-
	28-12-2018	R	33,165	0.32	1.78	5, 24	1.71	3.90	NV	-
	29-12-2018	R	46,230	1.26	1.64	8, 36	3.54	3.05	NV	-
1ES 0414+009	30-12-2016	R	34, 34	0.71	2.26	6, 28	11.19	3.53	NV	-
	19-01-2017	R	31, 31	0.21	2.35	5, 24	0.95	3.90	NV	-
	15-12-2018	R	55, 55	0.20	1.89	10, 44	6.55	2.75	NV	-
	16-12-2018	R	64, 64	0.30	1.80	12, 52	5.88	2.55	NV	-
	28-12-2018	R	29, 29	0.48	2.42	5, 24	3.59	3.90	NV	-
	29-12-2018	R	42, 42	0.23	2.08	7, 32	0.96	3.26	NV	-
1ES 0806+524	30-12-2016	V	36,108	0.66	1.81	6, 28	3.83	3.53	NV	-
		R	36,108	0.50	1.81	6, 28	2.21	3.53	NV	-
		V-R	36,108	0.61	1.81	6, 28	1.96	3.53	NV	-
	19-01-2017	V	26, 78	0.47	2.00	4, 20	1.91	4.43	NV	-
		R	26, 78	0.41	2.00	4, 20	1.32	4.43	NV	-
		V-R	26, 78	0.80	2.00	4, 20	2.44	4.43	NV	-
	10-01-2018	V	19, 38	2.81	2.42	3, 16	14.27	5.29	V	3.46
		R	19, 38	3.08	2.42	3, 16	27.56	5.29	V	3.88
		V-R	19, 38	0.44	2.42	3, 16	0.37	5.29	NV	-
	08-02-2018	V	24, 48	0.85	2.20	4, 20	14.89	4.43	NV	-
		R	24, 48	0.70	2.20	4, 20	13.09	4.43	NV	-
		V-R	24, 48	0.67	2.20	4, 20	1.10	4.43	NV	-
	09-02-2018	V	24, 48	0.84	2.20	4, 20	3.11	4.43	NV	-
		R	24, 48	0.71	2.20	4, 20	0.98	4.43	NV	-
		V-R	24, 48	0.96	2.20	4, 20	0.35	4.43	NV	-
	21-02-2018	V	29, 87	0.59	1.94	5, 24	1.58	3.90	NV	-
		R	29, 87	0.62	1.94	5, 24	1.99	3.90	NV	-
		V-R	29, 87	1.33	1.94	5, 24	1.49	3.90	NV	-
	15-12-2018	V	29, 87	0.57	1.94	5, 24	3.00	3.90	NV	-
		R	29, 87	0.54	1.94	5, 24	4.97	3.90	NV	-
		V-R	29, 87	1.31	1.94	5, 24	0.55	3.90	NV	-
	16-12-2018	V	40,120	0.56	1.76	7, 32	1.98	3.26	NV	-
		R	40,120	0.49	1.76	7, 32	2.44	3.26	NV	-
		V-R	40,120	0.88	1.76	7, 32	0.58	3.26	NV	-
	28-12-2018	V	33, 99	1.20	1.86	5, 24	5.11	3.90	NV	-
		R	33, 99	1.04	1.86	5, 24	7.23	3.90	NV	-
		V-R	33, 99	0.88	1.86	5, 24	2.27	3.90	NV	-
	29-12-2018	V	32, 96	0.77	1.88	5, 24	0.99	3.90	NV	-
		R	32, 96	0.22	1.88	5, 24	0.49	3.90	NV	-
		V-R	32, 96	0.68	1.88	5, 24	1.27	3.90	NV	-

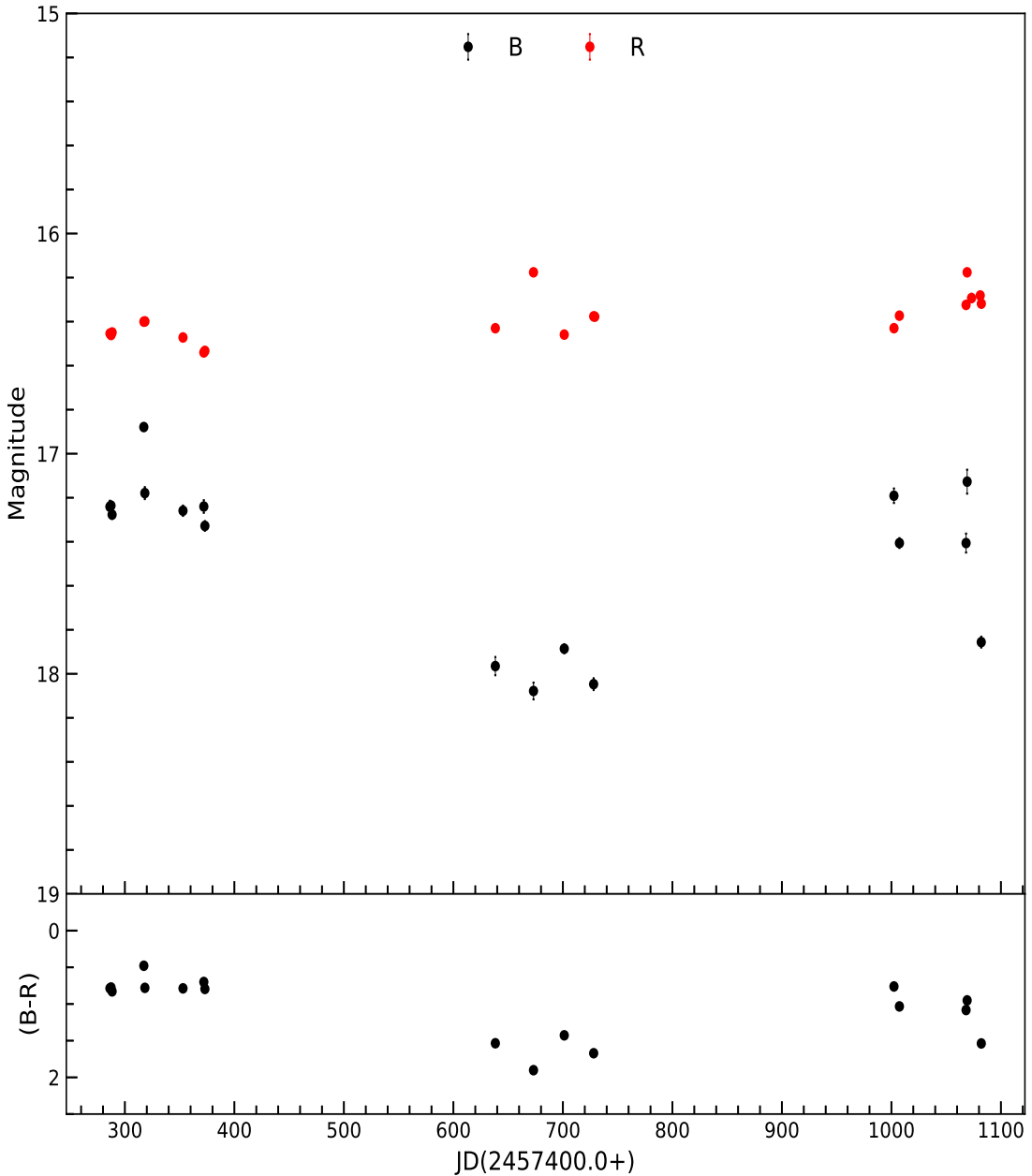


Figure 4.2a: LTV optical ($B - R$) LCs of 1ES 0229+200 in the upper panel and the color ($B - R$) variation on LTV timescales in the bottom panel.

4.4.2 Spectral Variability

In blazars, spectral changes are often seen with the optical flux variations. To study optical spectral variations in TeV blazars, we performed quasi-simultaneous observations in V and R bands for two TeV blazars: 1ES 0806+524 and PG 1553+113. To investigate spectral variability of these blazars on IDV timescales, we plotted the color ($V - R$) indices (CIs) with respect to time (color–time) and with respect to R band magnitude (color–magnitude). We have taken each pair

4. OPTICAL FLUX AND SPECTRAL VARIABILITY OF TEV BLAZARS

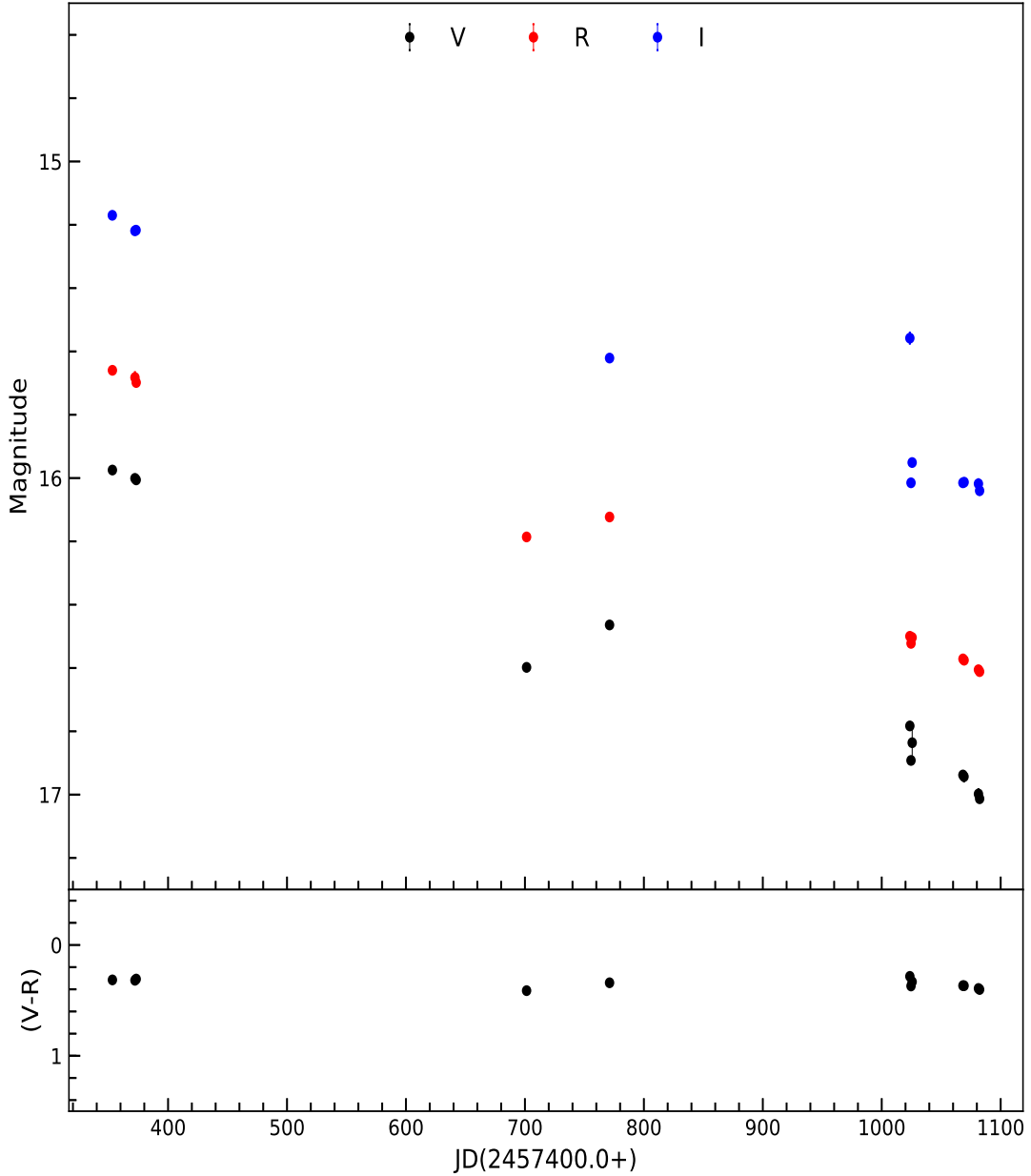


Figure 4.2b: LTV optical (VRI) LCs of 1ES 0414+009 in the upper panel and the color ($V - R$) variation on LTV timescales in the bottom panel.

of alternate V and R band images to get the color ($V - R$) considering the time for the color to be the mean of the times for V and R band observations. We fitted each color–magnitude plot by a straight line of the form $CI = mR + c$ to examine the color behavior of these blazars with respect to R magnitude. The results of the fits to color– magnitude plots are given in Table 4.4. The temporal $B - R$ color variation for 1ES 0229+200 on LTV timescale, plotted in the lower panel of Figure 4.2a, indicates a maximum variation of 1.423, while the temporal variations of $V - R$ color indices on STV/LTV timescales for 1ES 0414+009, 1ES

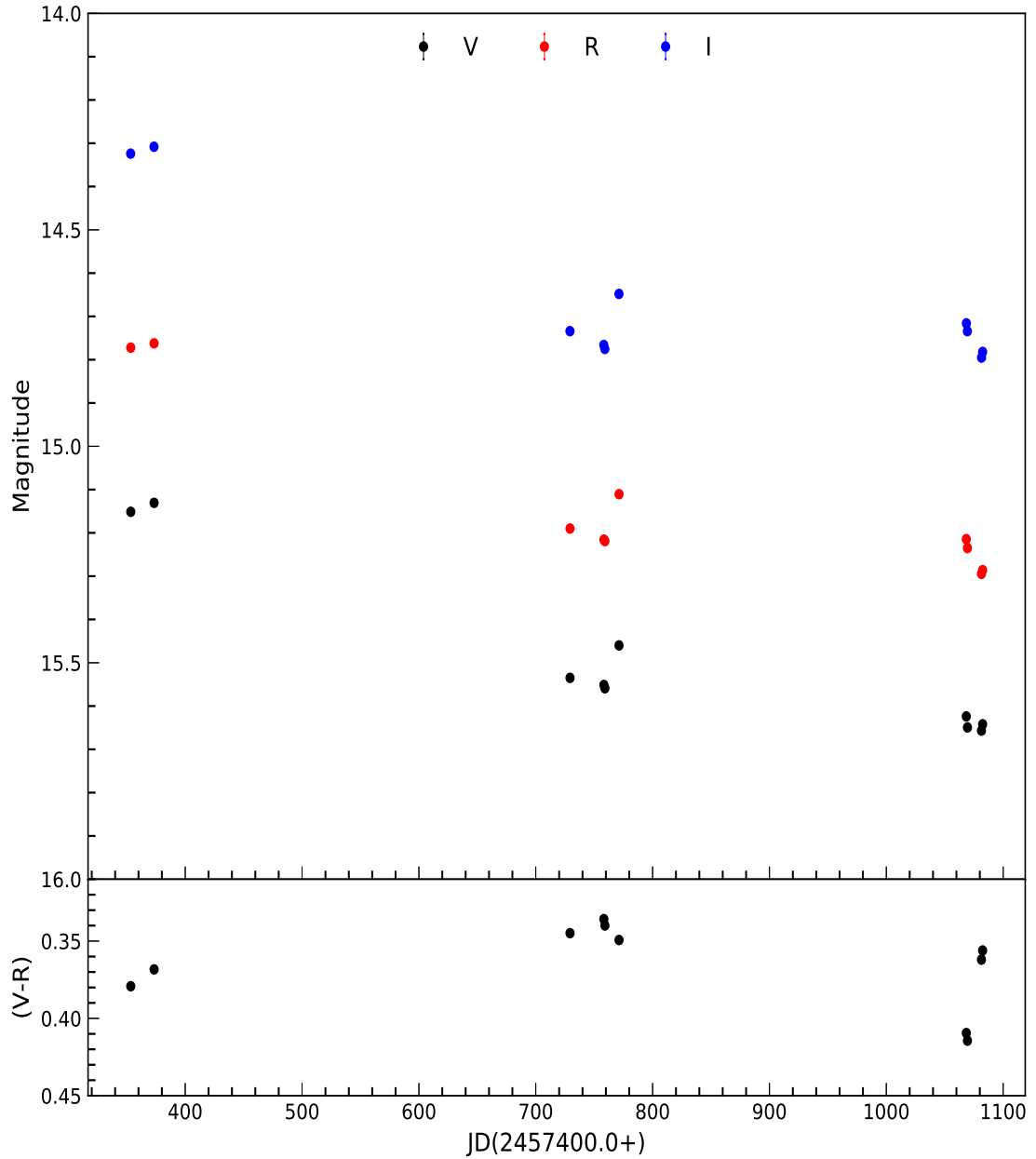


Figure 4.2c: LTV optical (*VRI*) LCs of 1ES 0806+524 in the upper panel and the color ($V - R$) variation on LTV timescales in the bottom panel.

0806+524, PG 1553+113, and 1ES 2344+514, plotted in lower panels of Figures 4.2b, 4.2c, 4.2d, and 4.2e, respectively, indicate maximum color variations of 0.129, 0.221, 0.065, and 0.135, respectively. The IDV spectral variability results for TeV blazars 1ES 0806+524 and PG 1553+113 are discussed below.

4. OPTICAL FLUX AND SPECTRAL VARIABILITY OF TEV BLAZARS

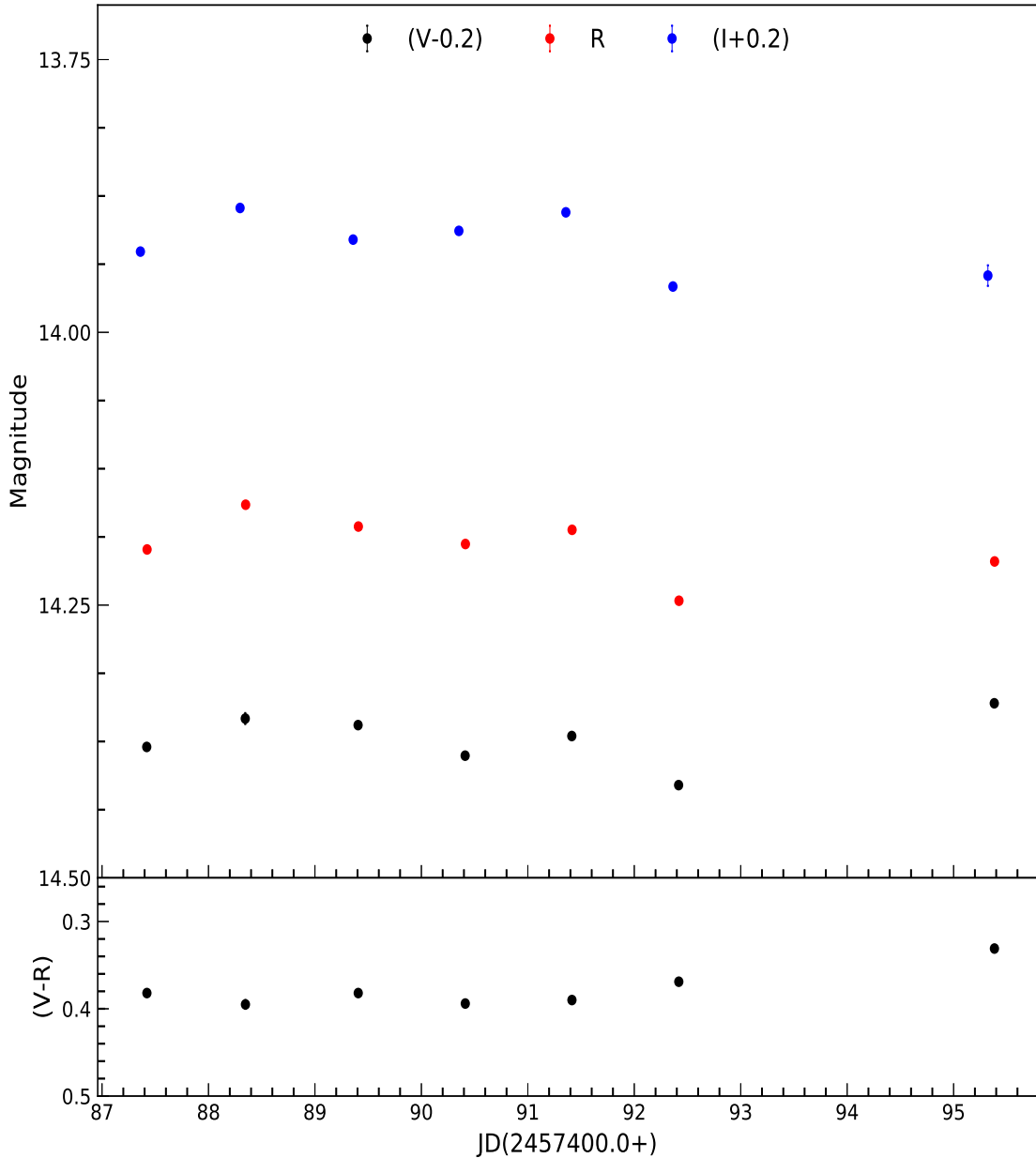


Figure 4.2d: STV optical (VRI) LCs of 1ES 1553+113 in the upper panel and the color ($V - R$) variation on STV timescales in the bottom panel.

4.4.2.1 1ES 0806+524

No significant temporal $V - R$ color variation was observed for the TeV blazar 1ES 0806+524 on any night, as shown in Table 4.3. The color–time plots for the blazar 1ES 0806+524 are plotted in Figure 4.3a. Also, we detected no significant strong correlation between $V - R$ color and R magnitude which is consistent with the non-detection of IDV or the detection of low amplitude IDV in the LCs of

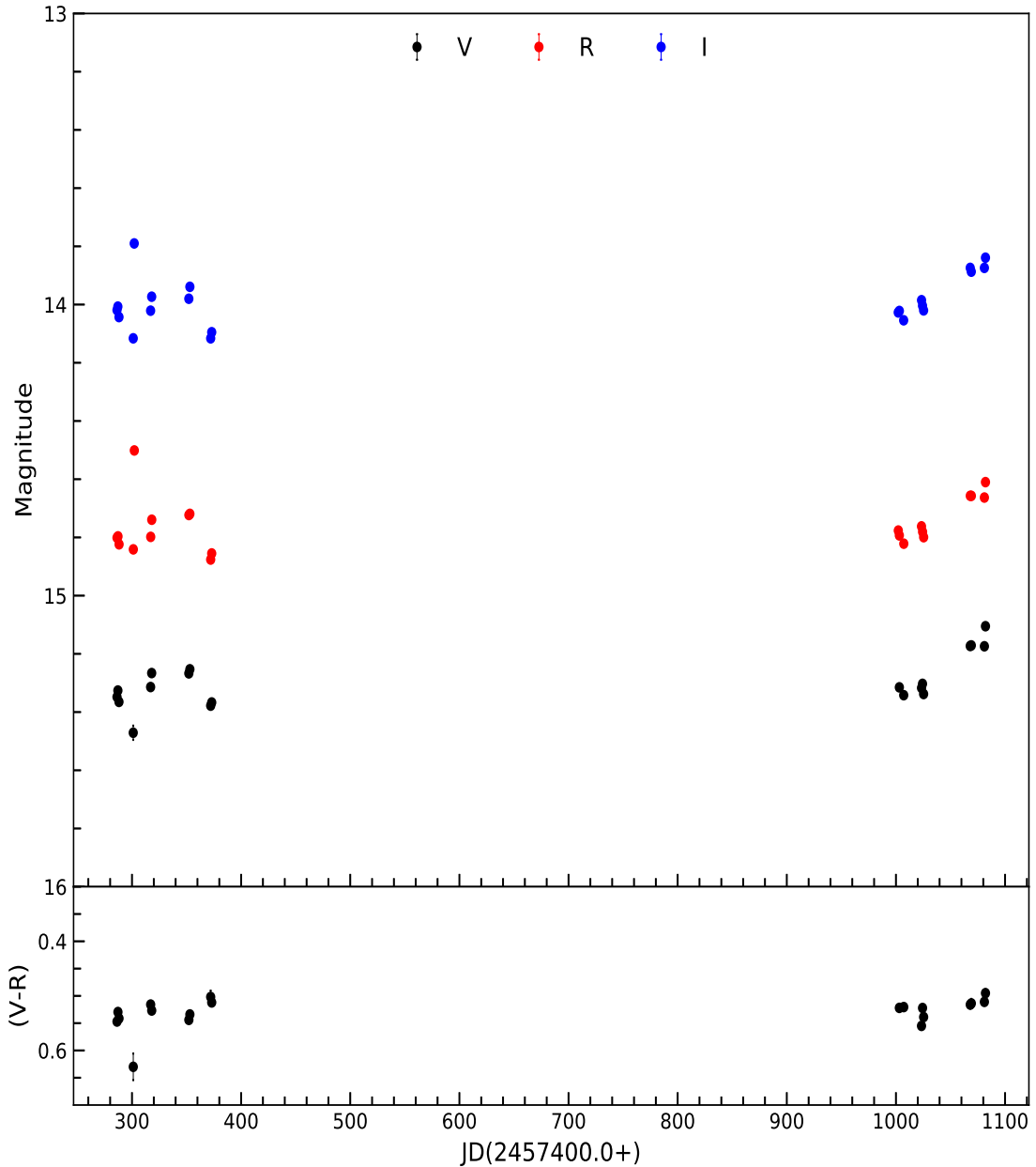


Figure 4.2e: LTV optical (VRI) LCs of 1ES 2344+514 in the upper panel and the color ($V - R$) variation on LTV timescales in the bottom panel.

1ES 0806+524. The color-magnitude plots for the TeV blazar 1ES 0806+524 are plotted in Figure 4.4a.

4. OPTICAL FLUX AND SPECTRAL VARIABILITY OF TEV BLAZARS

Table 4.3: continued.

Blazar Name	Observation date	Band	<i>Power-enhanced F-test</i>			<i>Nested ANOVA</i>			Status	Amplitude
			dd-mm-yyyy	DoF(ν_1, ν_2)	F_{enh}	F_c	DoF(ν_1, ν_2)	F	F_c	
PG 1553+113	06-04-2016	V	27, 54	1.33	2.11	6, 21	7.14	3.81	NV	-
		R	27, 54	1.34	2.11	6, 21	10.27	3.81	NV	-
		V-R	27, 54	1.11	2.11	6, 21	1.99	3.81	NV	-
		V	19, 38	2.07	2.42	4, 15	1.17	4.89	NV	-
		R	19, 38	4.32	2.42	4, 15	15.02	4.89	V	4.76
	08-04-2016	V-R	19, 38	1.46	2.42	4, 15	1.60	4.89	NV	-
		V	7, 14	0.24	4.28	1, 6	3.23	13.75	NV	-
		R	7, 14	7.17	4.28	1, 6	1.11	13.75	NV	-
	09-04-2016	V-R	7, 14	0.44	4.28	1, 6	7.58	13.75	NV	-
		V	15, 30	1.05	2.70	3, 12	1.34	5.95	NV	-
		R	15, 30	1.09	2.70	3, 12	0.43	5.95	NV	-
	10-04-2016	V-R	15, 30	1.36	2.70	3, 12	1.42	5.95	NV	-
		V	19, 38	0.84	2.42	4, 15	2.67	4.89	NV	-
		R	19, 38	2.09	2.42	4, 15	2.40	4.89	NV	-
	11-04-2016	V-R	19, 38	1.05	2.42	4, 15	2.64	4.89	NV	-
		V	20, 40	0.85	2.37	4, 15	7.22	4.89	NV	-
		R	20, 40	4.31	2.37	4, 15	14.53	4.89	V	3.44
	12-04-2016	V-R	20, 40	0.70	2.37	4, 15	6.34	4.89	NV	-
		V	17, 34	3.57	2.54	3, 12	7.25	5.95	V	11.23
		R	17, 34	7.45	2.54	3, 12	6.55	5.95	V	6.17
	13-04-2016	V-R	17, 34	1.70	2.54	3, 12	5.32	5.95	NV	-
		V	18, 36	0.29	2.48	3, 12	0.73	5.95	NV	-
		R	18, 36	0.22	2.48	3, 12	0.58	5.95	NV	-
	14-04-2016	V-R	18, 36	0.10	2.48	3, 12	0.28	5.95	NV	-
		V	58, 58	1.60	1.86	10, 44	19.55	2.75	NV	-
		R	69, 69	0.74	1.76	13, 56	3.41	2.47	NV	-
1ES 2344+514	08-11-2016	R	40, 40	0.15	2.11	7, 32	7.10	3.26	NV	-
		R	33, 33	0.50	2.29	5, 24	1.39	3.90	NV	-
		R	69, 69	1.53	1.76	13, 56	8.49	2.47	NV	-
	24-11-2016	R	59, 59	1.35	1.85	11, 48	13.47	2.64	NV	-
		R	35, 35	1.84	2.23	6, 28	8.02	3.53	NV	-
		R	94, 94	2.12	1.62	18, 76	8.86	2.18	V	2.26
	10-10-2018	R	69, 69	1.33	1.76	13, 56	1.82	2.47	NV	-
		R	59, 59	1.68	1.85	11, 48	7.68	2.64	NV	-
		R	59, 59	1.25	1.85	11, 48	5.43	2.64	NV	-

4.4.2.2 PG 1553+113

We observed no significant temporal variation in $V - R$ color for PG 1553+113, as shown in Table 4.3, which can also be clearly seen from the color–time plots, plotted in Figure 4.3b. We found no significant correlation between $V - R$ color and R magnitude on any observing night, which is consistent with the non-detection of IDV or the detection of only low amplitude IDV in the LCs. Even on April 13, when we observed variability in both V and R band LCs, the value of correlation coefficient is $r = 0.426$ with a substantial null hypothesis probability, $p = 0.078$, indicating no clear variation in $V - R$ color with magnitude. The IDV color–magnitude plots for the TeV HBL PG 1553+113 are plotted in Figure 4.4b.

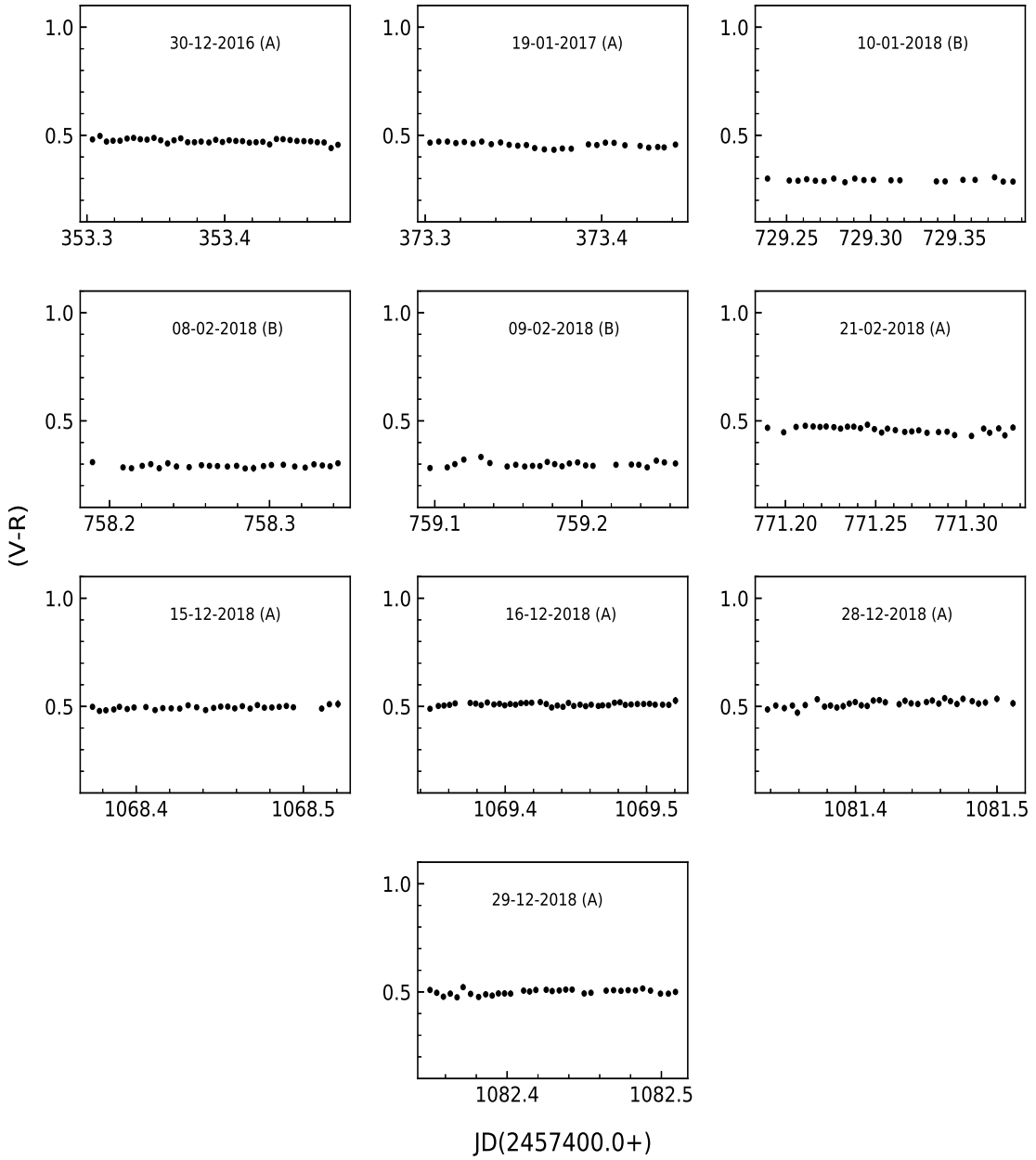


Figure 4.3a: IDV color-time plots for 1ES 0806+524. The observation date and the telescope code are given in each plot.

4.4.3 Spectral Energy Distributions (SEDs)

Since the optical (synchrotron) spectra of blazars are well described by a single power law ($F_\nu \propto \nu^{-\alpha}$, where α is the optical spectral index), we extracted the optical SEDs of four of the TeV blazars namely 1ES 0414+009, 1ES 0806+524, PG 1553+113, and 1ES 2344+514 (for which we have calibrated magnitudes in all the three optical V , R and I bands) to study optical spectral changes in more detail. For this, we have de-reddened the magnitudes in V , R and I bands using

4. OPTICAL FLUX AND SPECTRAL VARIABILITY OF TEV BLAZARS

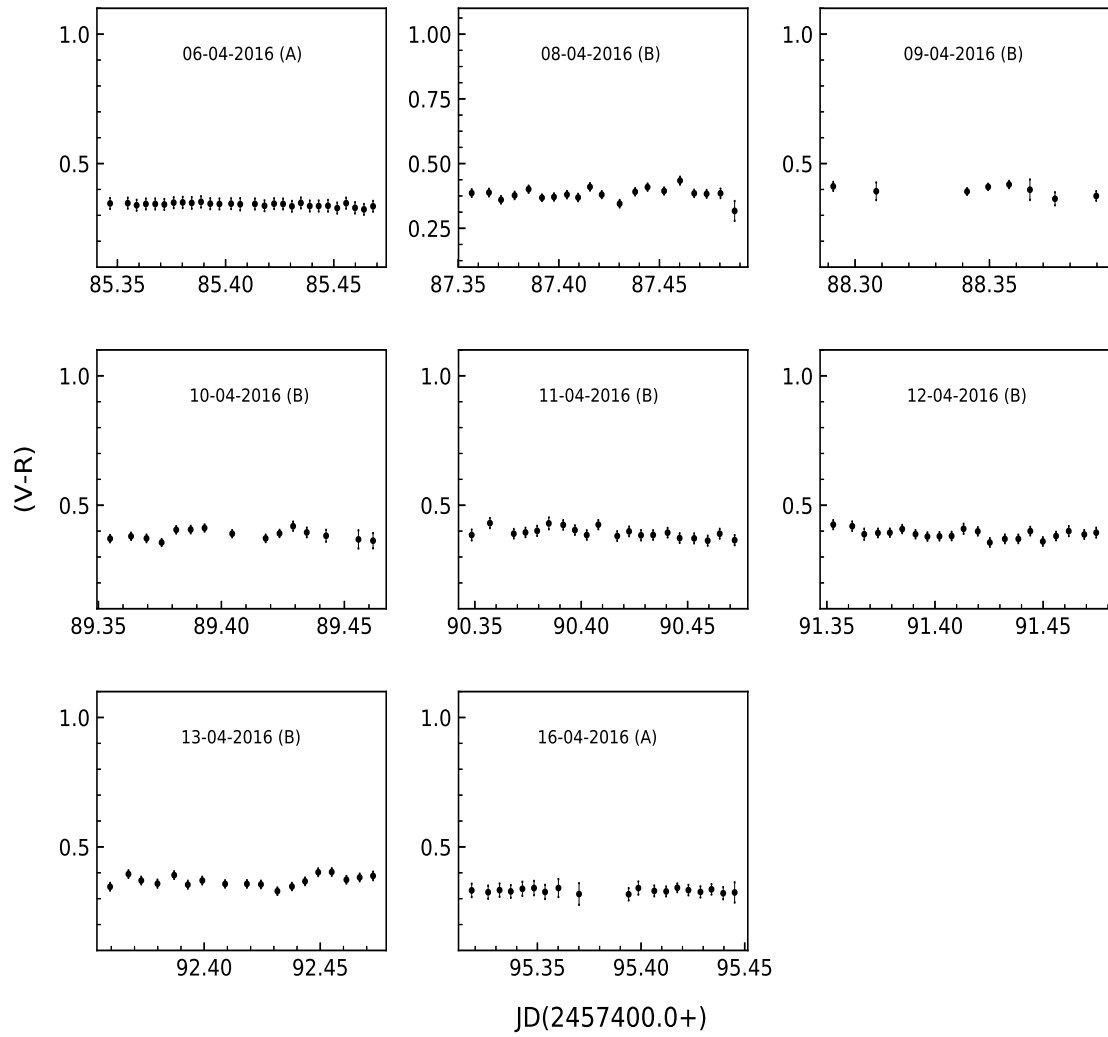


Figure 4.3b: IDV color-time plots for PG 1553+113. The observation date and the telescope code are given in each plot.

the Galactic extinction coefficients, given in Table 4.5, taken from the NASA Extragalactic Database (NED⁴) and then converted them into F_ν . The optical SEDs of these blazars, in the form of $\log(F_\nu) - \log(\nu)$, are fitted with a single power law, in the form of a straight line ($\log(F_\nu) = -\alpha \log(\nu) + C$) to get the nightly optical spectral index for each of the TeV blazars. The results of the fits are given in Table 4.6. Variation of the optical spectral index with time for these blazars are shown in Figure 4.6.

⁴<https://ned.ipac.caltech.edu/>

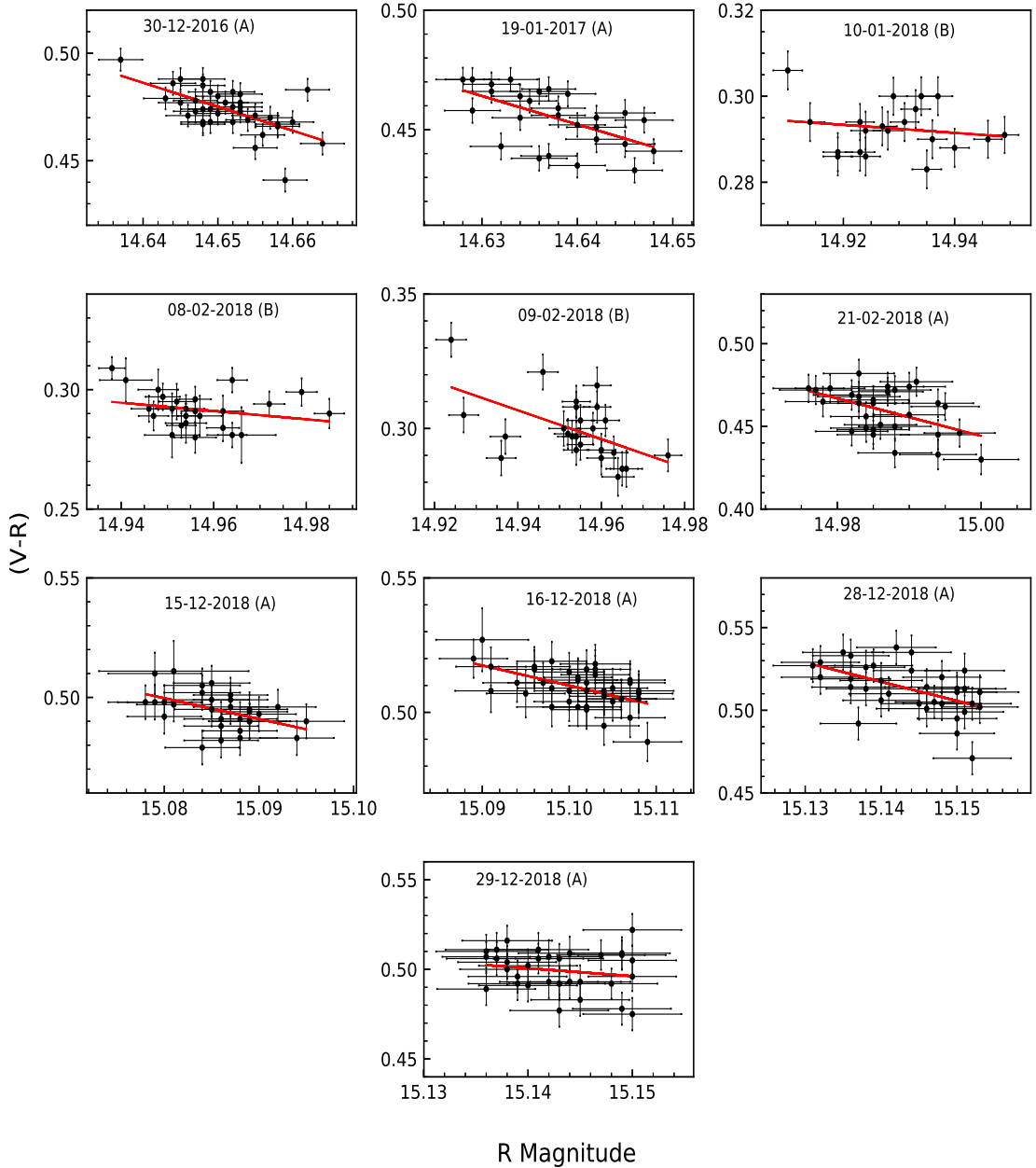


Figure 4.4a: IDV color-magnitude plots for 1ES 0806+524. The observation date and the telescope code are given in each plot.

4.4.3.1 1ES 0414+009

The optical SED of TeV blazar 1ES 0414+009 is plotted in Figure 4.5a. The value of optical spectral index ranges from 0.437–0.918, given in Table 4.6, with a maximum variation of 0.481. The mean spectral index during our monitoring period is 0.673 ± 0.024 .

4. OPTICAL FLUX AND SPECTRAL VARIABILITY OF TEV BLAZARS

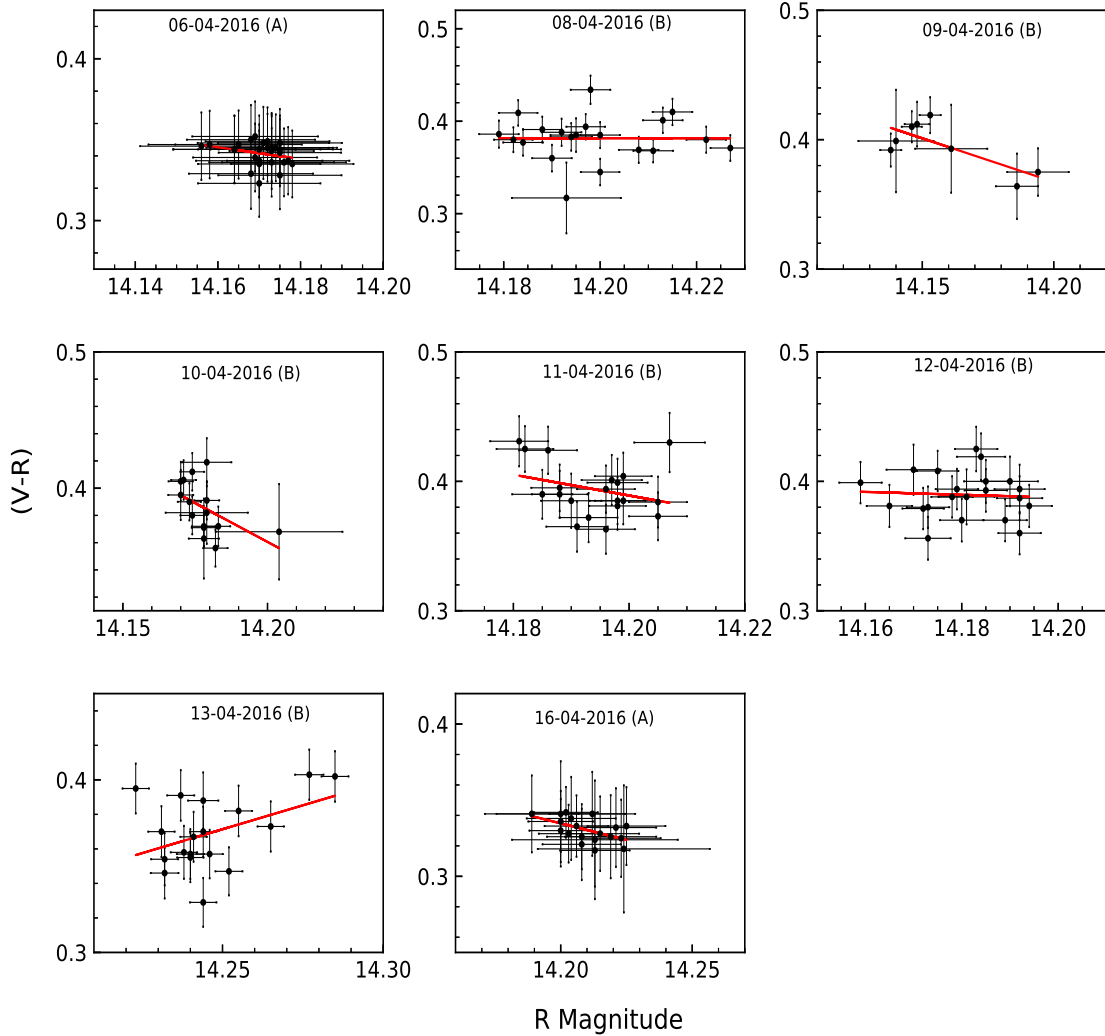


Figure 4.4b: IDV color-magnitude plots for PG 1553+113. The observation date and the telescope code are given in each plot.

4.4.3.2 1ES 0806+524

The SED of 1ES 0806+524 is shown in Figure 4.5b. The small values of correlation coefficient (r_2), given in Table 4.6, indicate that the SED of 1ES 0806+524 is not fitted well by the power law on 2018 January 10, and February 8–9. On remaining days the value of correlation coefficient (r_2) is relatively large but the errors in the spectral index are very high, as shown in Figure 4.6.

4.4.3.3 PG 1553+113

Optical (*VRI*) SED of PG 1553+113 is plotted in Figure 4.5c. The value of spectral index ranges from 0.688–0.896, listed in Table 4.6. The mean value of

Table 4.4: Linear fits to color-magnitude plots of TeV HBLs 1ES 0806+524 and PG 1553+113

Blazar Name	Observation date dd-mm-yyyy	m_1^a	c_1^a	r_1^a	p_1^a
1ES 0806+524	30-12-2016	-1.113 ± 0.240	16.781	-0.617	4.692e-05
	19-01-2017	-1.188 ± 0.332	17.846	-0.582	1.436e-03
	10-01-2018	-0.093 ± 0.135	1.683	-0.160	5.003e-01
	08-02-2018	-0.174 ± 0.143	2.888	-0.245	2.381e-01
	09-02-2018	-0.536 ± 0.176	8.319	-0.536	5.745e-03
	21-02-2018	-1.135 ± 0.396	17.469	-0.476	7.791e-03
	15-12-2018	-0.868 ± 0.303	13.587	-0.477	7.756e-03
	16-12-2018	-0.750 ± 0.184	11.838	-0.548	2.115e-04
	28-12-2018	-1.161 ± 0.325	18.092	-0.534	1.134e-03
	29-12-2018	-0.440 ± 0.429	7.165	-0.181	3.128e-01
	PG 1553+113	-0.366 ± 0.253	5.521	-0.273	1.600e-01
PG 1553+113	06-04-2016	-0.003 ± 0.427	0.427	-0.002	9.941e-01
	09-04-2016	-0.674 ± 0.241	9.938	-0.752	3.152e-02
	10-04-2016	-1.140 ± 0.556	16.544	-0.495	6.095e-02
	11-04-2016	-0.805 ± 0.611	11.817	-0.296	2.043e-01
	12-04-2016	-0.111 ± 0.425	1.959	-0.060	7.974e-01
	13-04-2016	0.554 ± 0.295	-7.529	0.426	7.828e-02
	16-04-2016	-0.435 ± 0.163	6.507	-0.544	1.608e-02

^a m_1 = slope and c_1 = intercept of CI against R-mag; r_1 = Correlation coefficient; p_1 = null hypothesis probability

spectral index during our observations is 0.829 ± 0.017 and the maximum variation is 0.21, as shown in Figure 4.6. These results are close to those found by [Falomo et al. \(1994\)](#).

4.4.3.4 1ES 2344+514

The optical SED of TeV HBL 1ES 2344+514 is shown in Figure 4.5c. The values of optical spectral index varies from 1.354 to 1.557, given in Table 4.6 and the maximum variation is 0.203, shown in Figure 4.6. The mean value of spectral index during our monitoring period is 1.446 ± 0.023 .

Table 4.5: Galactic extinction coefficients for the TeV blazars.

Blazar Name	A_V	A_R	A_I
1ES 0414+009	0.352	0.278	0.193
1ES 0806+524	0.123	0.097	0.068
1ES 1553+113	0.580	0.458	0.318
1ES 2344+514	0.142	0.113	0.078

4. OPTICAL FLUX AND SPECTRAL VARIABILITY OF TEV BLAZARS

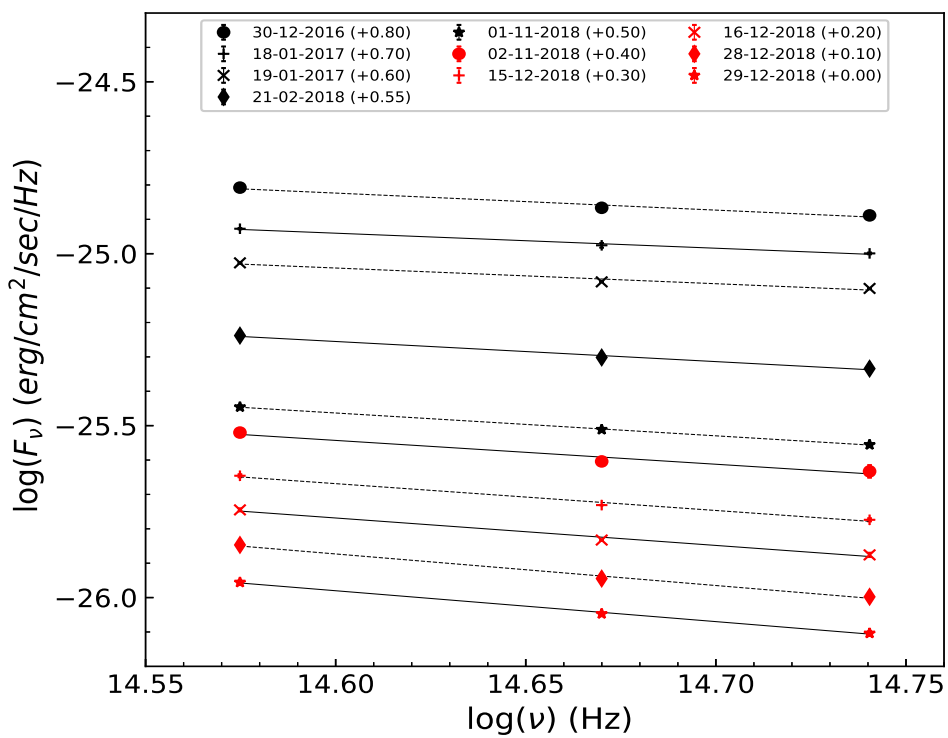


Figure 4.5a: SED of 1ES 0414+009 in V, R, and I bands.

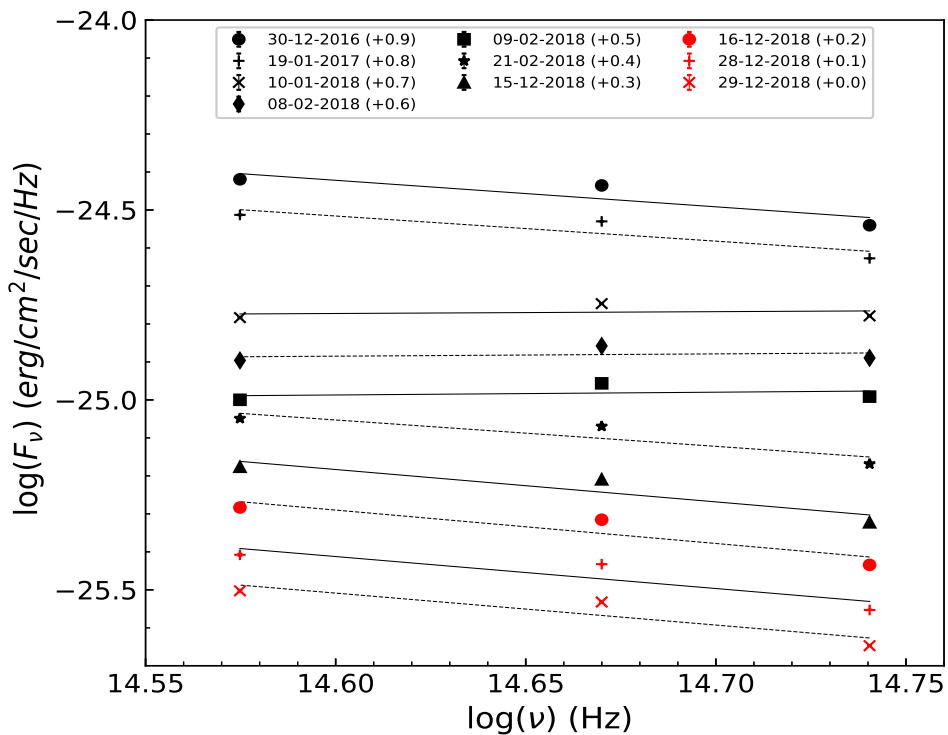


Figure 4.5b: SED of 1ES 0806+524 in V, R, and I bands.

Table 4.6: Straight line fits to optical SEDs of TeV blazars

Blazar name	Observation date dd-mm-yyyy	α^a	C^a	r_2^a	p_2^a
1ES 0414+009	30-12-2016	0.495 ± 0.085	-17.393	-0.986	1.082e-01
	18-01-2017	0.437 ± 0.048	-18.358	-0.994	7.034e-02
	19-01-2017	0.457 ± 0.087	-18.173	-0.982	1.197e-01
	21-02-2018	0.585 ± 0.058	-16.560	-0.995	6.294e-02
	01-11-2018	0.664 ± 0.019	-15.769	-1.000	1.774e-02
	02-11-2018	0.693 ± 0.132	-15.424	-0.982	1.196e-01
	15-12-2018	0.780 ± 0.081	-14.273	-0.995	6.584e-02
	16-12-2018	0.798 ± 0.087	-14.119	-0.994	6.927e-02
	28-12-2018	0.918 ± 0.077	-12.473	-0.997	5.319e-02
	29-12-2018	0.898 ± 0.044	-12.869	-0.999	3.095e-02
	30-12-2016	0.698 ± 0.369	-14.227	-0.884	3.097e-01
	19-01-2017	0.662 ± 0.337	-14.853	-0.891	2.995e-01
1ES 0806+524	10-01-2018	-0.048 ± 0.236	-25.474	0.200	8.720e-01
	08-02-2018	-0.060 ± 0.238	-25.766	0.246	8.420e-01
	09-02-2018	-0.073 ± 0.267	-26.054	0.264	8.298e-01
	21-02-2018	0.694 ± 0.333	-14.918	-0.902	2.845e-01
	15-12-2018	0.853 ± 0.352	-12.737	-0.924	2.495e-01
	16-12-2018	0.879 ± 0.378	-12.453	-0.919	2.586e-01
	28-12-2018	0.842 ± 0.406	-13.122	-0.901	2.863e-01
	29-12-2018	0.841 ± 0.371	-13.226	-0.915	2.643e-01
	06-04-2016	0.801 ± 0.038	-13.033	-0.999	3.026e-02
	08-04-2016	0.832 ± 0.053	-12.643	-0.998	4.086e-02
	09-04-2016	0.863 ± 0.076	-12.229	-0.996	5.618e-02
	10-04-2016	0.809 ± 0.066	-13.079	-0.997	5.165e-02
PG 1553+113	11-04-2016	0.896 ± 0.056	-11.855	-0.998	3.938e-02
	12-04-2016	0.895 ± 0.045	-11.912	-0.999	3.219e-02
	13-04-2016	0.842 ± 0.016	-12.743	-1.000	1.183e-02
	16-04-2016	0.688 ± 0.015	-15.052	-1.000	1.356e-02
	24-10-2016	1.512 ± 0.072	-1.270	-0.999	3.021e-02
	25-10-2016	1.491 ± 0.108	-1.672	-0.997	4.624e-02
	26-10-2016	1.495 ± 0.079	-1.716	-0.999	3.380e-02
	08-11-2016	1.557 ± 0.127	-0.935	-0.997	5.196e-02
	24-11-2016	1.428 ± 0.116	-2.884	-0.997	5.154e-02
	25-11-2016	1.426 ± 0.085	-3.002	-0.998	3.810e-02
	29-12-2016	1.407 ± 0.031	-3.383	-1.000	1.385e-02
	30-12-2016	1.477 ± 0.090	-2.443	-0.998	3.879e-02
1ES 2344+514	18-01-2017	1.354 ± 0.117	-4.412	-0.996	5.510e-02
	19-01-2017	1.376 ± 0.102	-4.170	-0.997	4.688e-02
	11-10-2018	1.427 ± 0.099	-3.506	-0.998	4.392e-02
	15-10-2018	1.415 ± 0.097	-3.797	-0.998	4.352e-02
	31-10-2018	1.517 ± 0.053	-2.373	-0.999	2.230e-02
	01-11-2018	1.442 ± 0.105	-3.579	-0.997	4.626e-02
	02-11-2018	1.486 ± 0.082	-3.045	-0.998	3.495e-02
	15-12-2018	1.443 ± 0.122	-3.706	-0.996	5.380e-02
	16-12-2018	1.406 ± 0.111	-4.354	-0.997	5.007e-02
	28-12-2018	1.447 ± 0.137	-3.853	-0.996	6.021e-02
	29-12-2018	1.365 ± 0.142	-5.131	-0.995	6.576e-02

^a α = spectral index and C = intercept of $\log(F_\nu)$ against $\log(\nu)$; r_2 = Correlation coefficient; p_2 = null hypothesis probability

4. OPTICAL FLUX AND SPECTRAL VARIABILITY OF TEV BLAZARS

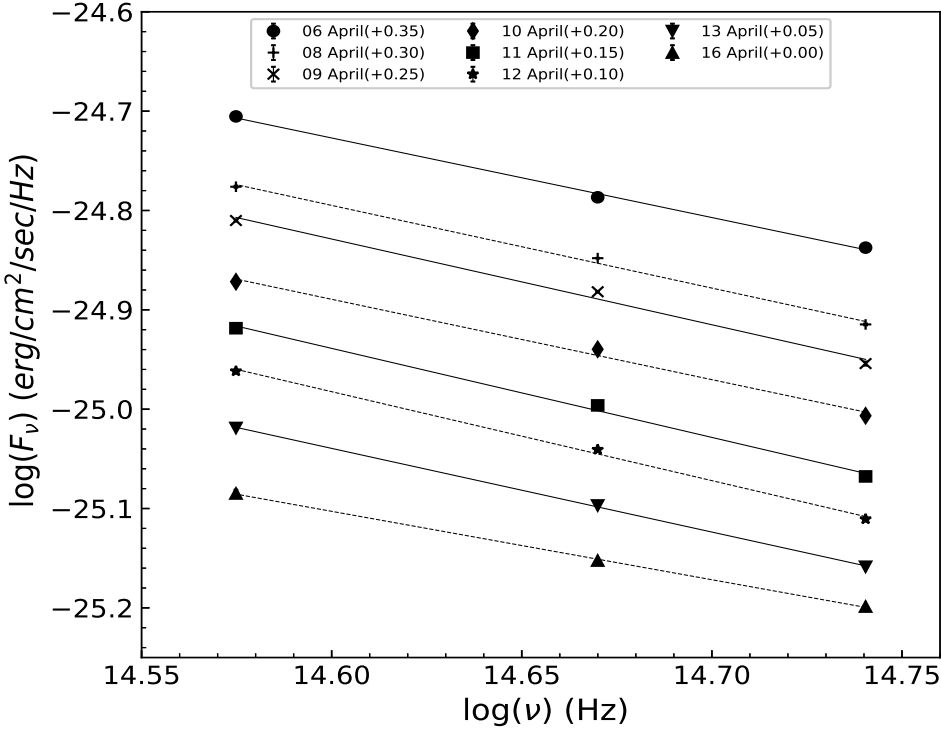


Figure 4.5c: SED of PG 1553+113 in V, R, and I bands.

4.5 Discussion and Conlcusions

Flux variability studies on diverse timescales constitute a powerful method to understand the radiation mechanisms of blazars. They also provide information about the size, location and dynamics of the emitting regions (e.g., Ciprini et al., 2003). In blazars, the Doppler-boosted non-thermal radiation coming from the relativistic jet generally overwhelm the thermal emission from the accretion disk, so the relativistic jet based models are most likely used to explain the variability on any measurable timescale. However, when the blazars are in very low states, the instabilities in, or hotspots on, the accretion disks can explain the variability in the LCs (e.g., Mangalam & Wiita, 1993; Chakrabarti & Wiita, 1993). Most of the LTV in the LCs of blazars can reasonably be explained by the shock-in-jet models (e.g., Agarwal & Gupta, 2015). When a shock, assumed to emanate from the base of the jet, moves outward along the jet, the electrons at the shock front get accelerated to high energies (Marscher & Gear, 1985). These high energy electrons are then cooled down via synchrotron emissions while leaving the shock front. The variations in the Doppler boosting factor, which can arise from the helical structures within the jet or the wiggles in the jet direction, can also contribute to the variability in the LCs of blazars (e.g., Camenzind & Krockenberger, 1992;

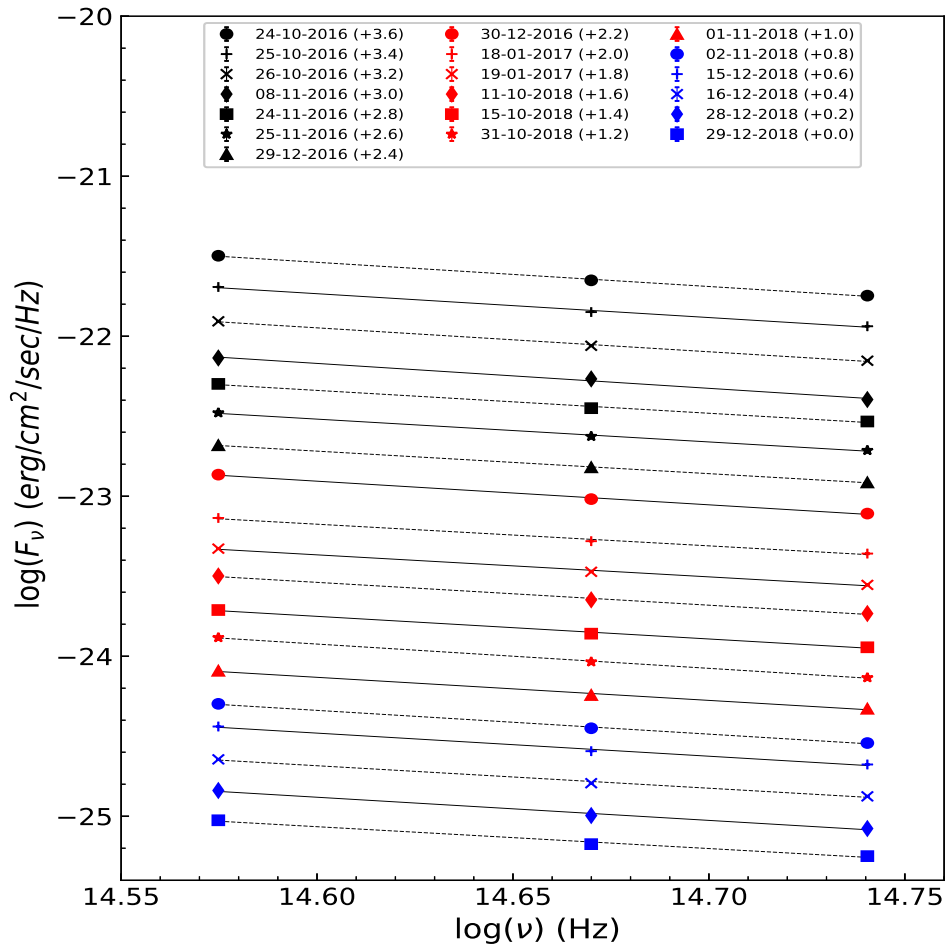


Figure 4.5d: SED of 1ES 2344+514 in V, R, and I bands.

Gopal-Krishna & Wiita, 1992; Villata & Raiteri, 1999). For the flux variations on the shorter timescales and smaller physical scales observed in this study of TeV HBLs, turbulence in relativistic plasma, either crossing a standing shock in the jet which in turn accelerates the electrons to very high energies (Marscher, 2014) or otherwise generating fluctuations (e.g., Calafut & Wiita, 2015; Pollack et al., 2016), may dominate.

The color or spectral behavior of blazars can be used to better understand the underlying radiation mechanisms. Generally, two different color behaviors have been detected in blazars which are: bluer-when-brighter (BWB) and redder-when-brighter (RWB). However, in some cases, researchers have also found no clear trend (e.g., Böttcher et al., 2009; Poon et al., 2009). A BWB trend indicates that the source becomes harder when its brightness increases or softer when its brightness decreases, while an RWB trend means the opposite behavior. The BWB trend is often observed in BL Lac objects, while the FSRQs generally follow an RWB

4. OPTICAL FLUX AND SPECTRAL VARIABILITY OF TEV BLAZARS

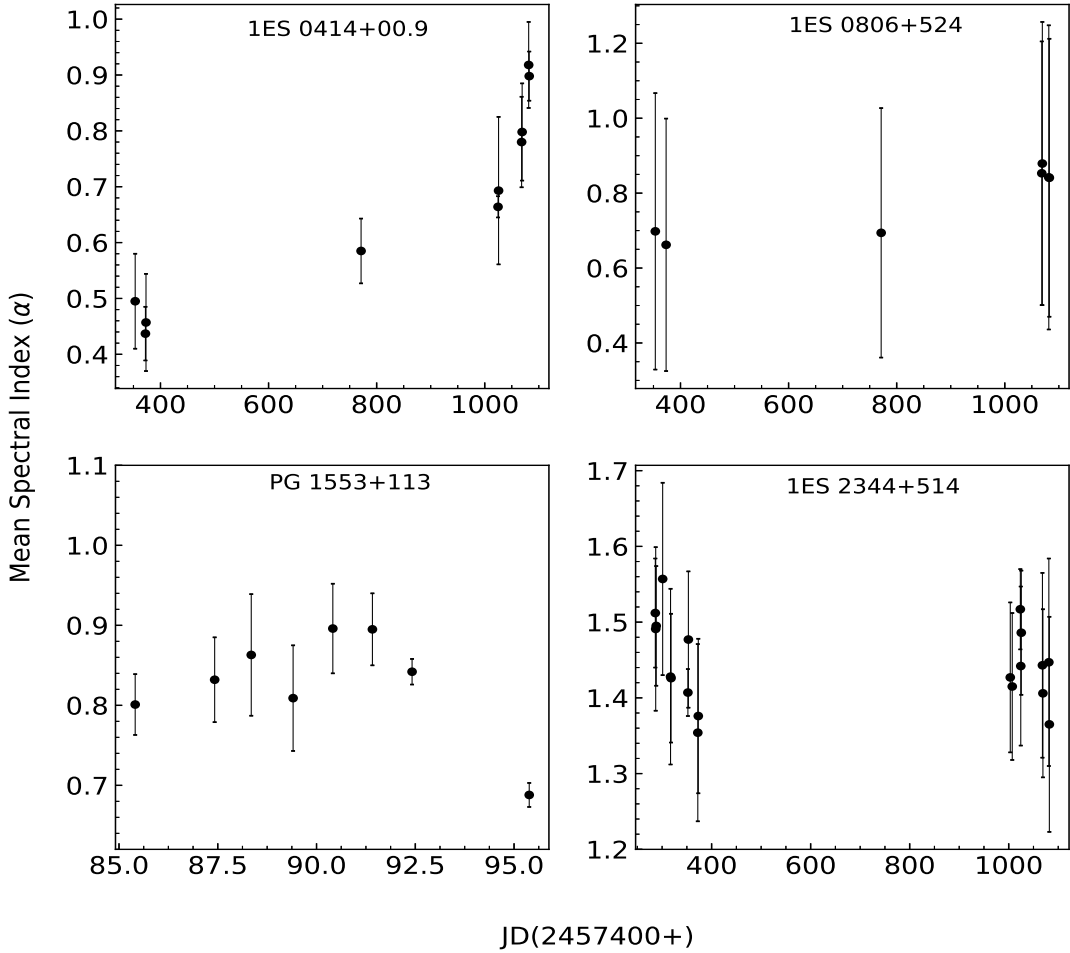


Figure 4.6: Variation in mean optical spectral index with time for TeV blazars. The name of the blazar is given in each plot.

trend (e.g., [Gaur et al., 2012b, 2015a](#)). Nonetheless, it has been observed that the same source may follow different color behaviors depending on its variation modes or timescales (e.g., [Raiteri et al., 2003; Wu et al., 2011](#)).

The commonly observed BWB trend can be interpreted in several different ways that require a great deal of data on many sources to distinguish between them. It may indicate that the overall optical emission is due to the two components, one of which is variable (α_{var}) having a flatter slope than the other stable ($\alpha_{const} > \alpha_{var}$) component ([Fiorucci et al., 2004](#)). One component synchrotron model could also explain the BWB behavior, in which the injection of fresh electrons causes an increase in the flux ([Kirk et al., 1998; Mastichiadis & Kirk, 2002](#)). The energy distribution of the fresh electrons is harder than that of the cooled ones. Another possible explanation of BWB behavior could be the variations in Doppler factor on a “convex” spectrum due to the precession of the jet ([Villata et al., 2004](#)). The

RWB trend usually found in FSRQs can emerge due to the presence of a quasi-thermal emission component from the accretion disk which is less variable and can “contaminate” the non-thermal emission from the jet in the optical and UV regions (e.g. [Wu et al., 2011](#)).

It has been found in several studies that the amplitude of optical IDV in the LCs of HBLs is statistically significantly smaller than that in the LCs of LBL ([Heidt & Wagner, 1998](#); [Romero et al., 1999](#); [Gopal-Krishna et al., 2011](#), e.g.). Our IDV analysis results are in line with this conclusion as we observed significant IDV in only four out of 43 R band LCs and in only two out of 18 V band LCs. The difference in the optical IDV behaviors of HBLs and LBLs could be due to the stronger magnetic field present in the HBLs ([Sambruna et al., 1996](#)) that might prevent the development of features like density inhomogeneities, bends and turbulent eddies in the bases of the jets ([Romero et al., 1999](#)). In particular, it has been argued that an axial magnetic field B can prevent the formation of instabilities if its value is greater than the critical value B_c given by ([Romero, 1995](#))

$$B_c = [4\pi n_e m_e c^2 (\gamma^2 - 1)]^{1/2} \gamma^{-1}, \quad (4.9)$$

where n_e is the local electron density, m_e is the rest mass of an electron, and γ is the bulk Lorentz factor of the flow. In HBLs, $B > B_c$ would prevent the development of small-scale structures that can be responsible for the microvariations in the optical light curves when they interact with the relativistic shocks.

We also noticed that the amplitude of variability decreases with increasing brightness for the TeV blazar PG 1553+113. On 2016 April 8, 12, and 13 the variability amplitudes of the blazar PG 1553+113 were 4.76%, 3.44%, and 6.17%, respectively, while its mean magnitudes were 14.199, 14.181, and 14.246, respectively. This can be interpreted as the irregularities in a turbulent jet decrease with increasing source flux. An increase in the flux gives rise to a more uniform flow which in turns reduces the variability amplitude ([Marscher, 2014](#)).

Usually, the variability amplitude of blazars is larger at higher frequencies, as was seen in PG 1553+113 on 2016 April 13 for which both were detectable, which suggests that the blazar spectrum gets steeper with decreasing brightness and flatter with increasing brightness (e.g., [Massaro et al., 1998](#); [Agarwal & Gupta, 2015](#)). However, on some occasions the variability amplitude of blazars at lower frequencies was found comparable to or even larger than that at higher frequencies (e.g., [Ghosh et al., 2000](#); [Gaur et al., 2015a](#)). We detected slightly lower variability

4. OPTICAL FLUX AND SPECTRAL VARIABILITY OF TEV BLAZARS

amplitude in V band LC than in R band LC on 2018 January 10 in blazar 1ES 0806+524.

In the present study of the five TeV HBLs performed during 2016–2018 with two optical telescopes in India, we found significant IDV flux variations in both V and R bands on one night for 1ES 0806+524 and in the R band on three nights and in the V band only on one of those nights for PG 1553+113. No significant IDV was found on any night in TeV HBLs 1ES 0229+200, 1ES 0414+009, and 1ES 2344+514. The photometry was carried out quasi-simultaneously in V and R bands in 1ES 0806+524 and PG 1553+113, while continuous R band observations were taken for rest three blazars. The blazars did not show large-amplitude variations during our monitoring period. We detected no strong IDV variations in color with time nor with brightness during our observations. We found mean optical power-law spectral index of 0.673 ± 0.024 , 0.83 ± 0.02 , and 1.446 ± 0.023 for TeV HBLs 1ES 0414+009, PG 1553+113, and 1ES 2344+514, respectively. On STV/LTV timescales, flux variations were seen at all observed optical wavelengths and the colors were also found variable for these TeV blazars.

Chapter 5

Summary, Conclusions and Future Plans

5.1 Summary

In this work, we tried to explore the nature, size, and location of the emitting region as well as the radiation mechanisms of the TeV blazars with the help of their variability properties using the hard X-ray (3–79 keV) data and the optical data. The results of our study are summarized in the following subsections:

5.1.1 Hard X-ray Studies of TeV Blazars

We examined the archival 46 *NuSTAR* LCs of eleven TeV blazars, listed in Table 3.1, for intraday flux and spectral variability. Using the discrete autocorrelation function, we searched for the possible variability timescales in these LCs. We split the *NuSTAR* LCs in soft (3–10 keV) and hard (10–79) energy bands and searched for a correlation between them. We also investigated the hard X-ray spectral shape of six of those TeV blazars. The results of the hard X-ray study of TeV blazars are summarized below:

- We have found strong evidence for intraday variations for: 1ES 1101–232, in 1 of 1 LC; Mrk 421, in all 22 of 22 LCs; 1ES 1218+304, in 1 of 1 LC; Mrk 501, in 3 of 4 LCs; 1ES 1959+650, in 1 of 2 LCs; and in PKS 2155–304, in 7 of 9 LCs.

5. SUMMARY, CONCLUSIONS AND FUTURE PLANS

- We found evidence for variability timescales ranging from 2.5 to 57.4 ks in 12 LCs, while no variability timescale was clearly seen in the remaining 34 LCs.
- We constrained the values of the magnetic field strength (B), electron Lorentz factor (γ) and the characteristic size (R) of emitting regions for Mrk 421, 1ES 1218+304, Mrk 501, and PKS 2155–304, given in Table 3.6, using their observed minimum variability timescales.
- We found that the *NuSTAR* spectra of Mrk 421 and Mrk 501 become harder with increasing count rates.
- We observed positive correlations with zero time lag between the soft (3–10 keV) and hard (10–79 keV) band LCs for Mrk 421 (in all 22 observations), for Mrk 501 (in 3 out of 4), for 1ES 1959+650 (in 1 out of 2) and for PKS 2155–304 (in 7 out of 9).
- We found that the hard X-ray (3–79 keV) spectra of five TeV HBLs 1ES 0347–121, RGB J0710+591, 1ES 1101–232, 1ES 1218+304 and H 2356–309 are curved and are fitted well by log parabolic model, while the simple power law provides the better fit for the *NuSTAR* spectra of 1ES 0414+009.

5.1.2 Optical Studies of TeV Blazars

We performed the optical photometric observations of five TeV HBLs; 1ES 0229+200, 1ES 0414+009, 1ES 0806+524, 1ES 1553+113, and 1ES 2344+514 during 2016–2018 using two Indian telescopes. We searched for flux and color variations in the LCs of these TeV HBLs using the power-enhanced F -test and the nested ANOVA test. The results of the optical study of TeV blazars are summarized below:

- Significant intraday flux variations were detected in both V and R band LCs only on 2018 January 10 for 1ES 0806+524 and on 2016 April 13 for 1ES 1553+113. In addition, we found significant IDV only in R band LCs of 1ES 1553+113 on 2016 April 8, and 12, while no IDV was detected in V band LCs on those nights.
- No significant IDV was observed on any night for TeV HBLs 1ES 0229+200, 1ES 0414+009, and 1ES 2344+514.

- We found no temporal $V - R$ color variation on IDV timescale for these TeV blazars.
- We also did not find any variation in $V - R$ color with R band magnitude on IDV timescale.
- We found flux and color variations on STV/LTV timescales in all five TeV blazars.
- We recorded a mean optical spectral index of 0.673, 0.830, and 1.446 for TeV blazars 1ES 0414+009, PG 1553+113, and 1ES 2344+514, respectively.

5.2 Conclusions

From the results of our hard X-ray and optical variability studies of TeV blazars, we conclude that:

- On IDV timescale, TeV blazars exhibit flux variations with large variability amplitudes in 3–79 keV X-ray bands.
- The variability amplitudes are, in general, larger at hard (10–79 keV) energy bands than at soft (3–10 keV) energy bands.
- TeV blazars can show flux variations at very short timescales in X-ray bands. We found shortest variability timescale of 2.5 ks in X-ray LC of Mrk 421 that indicates that X-ray emissions are coming from very compact ($\sim 10^{15}$ cm) regions.
- The 3–79 keV X-ray spectra of TeV blazars become harder with increasing brightness.
- The soft (3–10 keV) and hard (10–79 keV) X-ray emissions from TeV blazars are produced by the same populations of electrons.
- The 3–79 keV X-ray spectra of TeV blazars are generally curved and are better represented by log parabolic model.
- At optical wavelengths, TeV HBLs are less variable and their variability amplitudes are very small that can be explained by the turbulence in the relativistic plasma.

5. SUMMARY, CONCLUSIONS AND FUTURE PLANS

- On STV/LTV timescales, TeV HBLs show flux and color variations that can reasonably be explained by the shock-in-jet models.
- We did not find the bluer-when-brighter trend for our TeV HBLs. But we still need more optical observations of other TeV HBLs to come to any conclusion.
- The optical variability amplitude usually decreases with increasing brightness for the TeV HBLs. But again we need more observations of TeV HBLs to conclude any result.

5.3 Future Plans

We have studied the flux and spectral variability properties of TeV blazars at hard X-ray and optical wavebands to understand their structure and emission mechanisms. To get more understanding of the physics of this extreme subclass of blazars long term simultaneous multiband observations covering the entire electromagnetic spectrum are needed. A large number of space-based observatories e.g., *Fermi*, *NuSTAR*, *XMM*-Newton, *Chandra*, *Swift* etc., are available that provide coverage from UV to γ -rays. There are several ground-based optical and radio telescopes that give us a chance to study the behavior of these source at these wavebands. India's first multiwavelength satellite AstroSAT can perform simultaneous observations in UV to hard X-ray bands. Using the data from all these observing facilities, we can perform the following studies,

- We can generate broadband (radio to γ -ray) SEDs of TeV blazars and fit them with different emission models to understand radiation processes at different frequencies.
- We can examine the X-ray spectra of a large sample of TeV blazars to get information about their acceleration mechanisms.
- We can cross-correlate the low energy (radio/optical/UV) fluxes with the high energy (X-ray/ γ -ray) fluxes of TeV blazars to understand whether the high energy emission is due to synchrotron self Compton (SSC) or external Compton (EC).
- We didn't get any color variation in observed TeV blazars during our monitoring period. To get a conclusion, we can increase our blazar sample and observe these blazars for a longer period.

References

- Abdo, A. A., et al. 2014, ApJ, 782, 110
- Abdo, A. A., et al. 2010, ApJ, 716, 30
- Abramowski, A., et al. 2015, ApJ, 802, 65
- Acciari, V., et al. 2009a, ApJ, 690, L126
- Acciari, V. A., et al. 2010, ApJ, 715, L49
- Acciari, V. A., et al. 2009b, ApJ, 695, 1370
- Agarwal, A., & Gupta, A. C. 2015, MNRAS, 450, 541
- Agarwal, A., et al. 2016, MNRAS, 455, 680
- Aharonian, F., et al. 2007a, A&A, 475, L9
- Aharonian, F., et al. 2007b, A&A, 473, L25
- Aharonian, F., et al. 1997, A&A, 327, L5
- Aharonian, F., Akhperjanian, A. G., Bazer-Bachi, A. R., Behera, B., Beilicke, M., & Benbow, W. 2007c, ApJ, 664, L71
- Aharonian, F., et al. 2007d, A&A, 470, 475
- Aharonian, F. A., Akhperjanian, A. G., Barrio, J. A., Bernlöhr, K., & Bojahr, H. 1999a, A&A, 349, 11
- Aharonian, F. A., et al. 1999b, A&A, 342, 69
- Albert, J., et al. 2007, ApJ, 669, 862
- Aleksić, J., et al. 2015, A&A, 576, A126
- Aliu, E., et al. 2016, A&A, 594, A76

REFERENCES

- Aliu, E., et al. 2014, ApJ, 782, 13
- Aliu, E., et al. 2012, ApJ, 755, 118
- Antonucci, R. 1993, ARA&A, 31, 473
- Bachev, R., Semkov, E., Strigachev, A., Gupta, A. C., Gaur, H., Mihov, B., Boeva, S., & Slavcheva-Mihova, L. 2012, MNRAS, 424, 2625
- Baloković, M., et al. 2016, ApJ, 819, 156
- Beckmann, V., & Shrader, C. R. 2012, Active Galactic Nuclei
- Beckmann, V., Wolter, A., Celotti, A., Costamante, L., Ghisellini, G., Maccacaro, T., & Tagliaferri, G. 2002, A&A, 383, 410
- Begelman, M. C., Blandford, R. D., & Rees, M. J. 1980, Nature, 287, 307
- Begelman, M. C., Fabian, A. C., & Rees, M. J. 2008, MNRAS, 384, L19
- Bhagwan, J., Gupta, A. C., Papadakis, I. E., & Wiita, P. J. 2016, New A, 44, 21
- Bhatta, G., Mohorian, M., & Bilinsky, I. 2018, A&A, 619, A93
- Blandford, R., & Eichler, D. 1987, Phys. Rep., 154, 1
- Blandford, R. D., & Rees, M. J. 1978, Phys. Scr, 17, 265
- Blasi, M. G., et al. 2013, A&A, 559, A75
- Błażejowski, M., et al. 2005, ApJ, 630, 130
- Böttcher, M., et al. 2009, ApJ, 694, 174
- Brinkmann, W., Papadakis, I. E., den Herder, J. W. A., & Haberl, F. 2003, A&A, 402, 929
- Calafut, V., & Wiita, P. J. 2015, Journal of Astrophysics and Astronomy, 36, 255
- Camenzind, M., & Krockenberger, M. 1992, A&A, 255, 59
- Carini, M. T. 1990, Ph.D. thesis, Georgia State University, Atlanta.
- Catanese, M., et al. 1998, ApJ, 501, 616
- Catanese, M., et al. 1997, ApJ, 487, L143
- Catanese, M., & Sambruna, R. M. 2000, ApJ, 534, L39

- Chadwick, P. M., et al. 1999, ApJ, 513, 161
- Chakrabarti, S. K., & Wiita, P. J. 1993, ApJ, 411, 602
- Chakraborty, N., et al. 2015, ArXiv e-prints
- Ciprini, S., Tosti, G., Raiteri, C. M., Villata, M., Ibrahimov, M. A., Nucciarelli, G., & Lanteri, L. 2003, A&A, 400, 487
- Cologna, G., Mohamed, M., Wagner, S. J., Wierzcholska, A., Romoli, C., for the H. E. S. S. Collaboration, & Kurtanidze, O. 2015, ArXiv e-prints
- Cortina, J., & Holder, J. 2013, The Astronomer's Telegram, 4976
- Costa, E., et al. 2008, The Astronomer's Telegram, 1574
- Costamante, L., et al. 2001, A&A, 371, 512
- Cui, W. 2004, ApJ, 605, 662
- Danforth, C. W., Keeney, B. A., Stocke, J. T., Shull, J. M., & Yao, Y. 2010, ApJ, 720, 976
- de Diego, J. A. 2014, AJ, 148, 93
- de Diego, J. A., Polednikova, J., Bongiovanni, A., Pérez García, A. M., De Leo, M. A., Verdugo, T., & Cepa, J. 2015, AJ, 150, 44
- Djannati-Atai , A., et al. 1999, A&A, 350, 17
- Donato, D., Sambruna, R. M., & Gliozzi, M. 2005, A&A, 433, 1163
- Edelson, R. A., & Krolik, J. H. 1988, ApJ, 333, 646
- Elvis, M., Plummer, D., Schachter, J., & Fabbiano, G. 1992, ApJS, 80, 257
- Falomo, R. 1991, AJ, 101, 821
- Falomo, R., Pesce, J. E., & Treves, A. 1993, ApJ, 411, L63
- Falomo, R., Scarpa, R., & Bersanelli, M. 1994, ApJS, 93, 125
- Falomo, R., & Treves, A. 1990, PASP, 102, 1120
- Fan, J.-H., Kurtanidze, O. M., Nikolashvili, M. G., Gupta, A. C., Zhang, J.-S., & Yuan, Y.-H. 2004, Chinese J. Astron. Astrophys., 4, 133
- Fan, J. H., & Lin, R. G. 1999, ApJS, 121, 131

REFERENCES

- Fan, J. H., & Lin, R. G. 2000, ApJ, 537, 101
- Fan, J. H., Qian, B. C., & Tao, J. 2001, A&A, 369, 758
- Fanaroff, B. L., & Riley, J. M. 1974, MNRAS, 167, 31P
- Farina, E. P., Fumagalli, M., Decarli, R., & Fanidakis, N. 2016, MNRAS, 455, 618
- Fiorucci, M., Ciprini, S., & Tosti, G. 2004, A&A, 419, 25
- Forman, W., Jones, C., Cominsky, L., Julien, P., Murray, S., Peters, G., Tananbaum, H., & Giacconi, R. 1978, ApJS, 38, 357
- Fossati, G., et al. 2008, ApJ, 677, 906
- Fraija, N., Cabrera, J. I., Benítez, E., & Hiriart, D. 2015, ArXiv e-prints
- Furniss, A., et al. 2015, ApJ, 812, 65
- Gaur, H., et al. 2015a, MNRAS, 452, 4263
- Gaur, H., et al. 2015b, A&A, 582, A103
- Gaur, H., Gupta, A. C., Lachowicz, P., & Wiita, P. J. 2010, ApJ, 718, 279
- Gaur, H., et al. 2012a, MNRAS, 420, 3147
- Gaur, H., et al. 2012b, MNRAS, 425, 3002
- Gaur, H., Gupta, A. C., & Wiita, P. J. 2012, AJ, 143, 23
- Ghisellini, G., ed. 2013, Lecture Notes in Physics, Berlin Springer Verlag, Vol. 873, Radiative Processes in High Energy Astrophysics
- Ghisellini, G., & Tavecchio, F. 2008, MNRAS, 386, L28
- Ghosh, K. K., Ramsey, B. D., Sadun, A. C., Soundararajaperumal, S., & Wang, J. 2000, ApJ, 537, 638
- Giannios, D., Uzdensky, D. A., & Begelman, M. C. 2009, MNRAS, 395, L29
- Giebels, B., et al. 2002, ApJ, 571, 763
- Giommi, P., Ansari, S. G., & Micol, A. 1995, A&AS, 109, 267
- Giommi, P., Capalbi, M., Fiocchi, M., Memola, E., Perri, M., Piranomonte, S., Rebecchi, S., & Massaro, E. 2002, in Blazar Astrophysics with BeppoSAX and Other Observatories, ed. P. Giommi, E. Massaro, & G. Palumbo, 63

- Giommi, P., Padovani, P., & Perlman, E. 2000, MNRAS, 317, 743
- Giommi, P., et al. 1991, ApJ, 378, 77
- Giroletti, M., et al. 2004, ApJ, 600, 127
- Gopal-Krishna, Goyal, A., Joshi, S., Karthick, C., Sagar, R., Wiita, P. J., Anupama, G. C., & Sahu, D. K. 2011, MNRAS, 416, 101
- Gopal-Krishna, & Wiita, P. J. 1992, A&A, 259, 109
- Gopal-Krishna, Wiita, P. J., & Dhurde, S. 2006, MNRAS, 369, 1287
- Green, R. F., Schmidt, M., & Liebert, J. 1986, ApJS, 61, 305
- Gu, M. F., Lee, C.-U., Pak, S., Yim, H. S., & Fletcher, A. B. 2006, A&A, 450, 39
- Gupta, A. C. 2011, Journal of Astrophysics and Astronomy, 32, 155
- Gupta, A. C., Acharya, B. S., Bose, D., Chitnis, V. R., & Fan, J.-H. 2008a, Chinese J. Astron. Astrophys., 8, 395
- Gupta, A. C., et al. 2016, MNRAS, 458, 1127
- Gupta, A. C., Banerjee, D. P. K., Ashok, N. M., & Joshi, U. C. 2004, A&A, 422, 505
- Gupta, A. C., Fan, J. H., Bai, J. M., & Wagner, S. J. 2008b, AJ, 135, 1384
- Halpern, J. P., Chen, V. S., Madejski, G. M., & Chanan, G. A. 1991, AJ, 101, 818
- Harrison, F. A., et al. 2013, ApJ, 770, 103
- Hazard, C., Mackey, M. B., & Shimmins, A. J. 1963, Nature, 197, 1037
- Heidt, J., & Wagner, S. J. 1996, A&A, 305, 42
- Heidt, J., & Wagner, S. J. 1998, A&A, 329, 853
- H.E.S.S. Collaboration, et al. 2010, A&A, 516, A56
- Horan, D., et al. 2009, ApJ, 695, 596
- Hovatta, T., et al. 2015, MNRAS, 448, 3121
- Hufnagel, B. R., & Bregman, J. N. 1992, ApJ, 386, 473
- Isobe, N., et al. 2015, ApJ, 798, 27

REFERENCES

- Joshi, R., Chand, H., Gupta, A. C., & Wiita, P. J. 2011, MNRAS, 412, 2717
- Kalberla, P. M. W., Burton, W. B., Hartmann, D., Arnal, E. M., Bajaja, E., Morras, R., & Pöppel, W. G. L. 2005, A&A, 440, 775
- Kapanadze, B. Z. 2009, MNRAS, 398, 832
- Kataoka, J., & Stawarz, L. 2016, ArXiv e-prints
- Kataoka, J., Takahashi, T., Makino, F., Inoue, S., Madejski, G. M., Tashiro, M., Urry, C. M., & Kubo, H. 2000, ApJ, 528, 243
- Kellermann, K. I., Sramek, R., Schmidt, M., Shaffer, D. B., & Green, R. 1989, AJ, 98, 1195
- Kerrick, A. D., et al. 1995, ApJ, 438, L59
- Kirk, J. G., Rieger, F. M., & Mastichiadis, A. 1998, A&A, 333, 452
- Kshama, S. K., Paliya, V. S., & Stalin, C. S. 2017, MNRAS, 466, 2679
- Lachowicz, P., Gupta, A. C., Gaur, H., & Wiita, P. J. 2009, A&A, 506, L17
- Li, H. Z., Jiang, Y. G., Guo, D. F., Chen, X., & Yi, T. F. 2016, PASP, 128, 074101
- Lico, R., et al. 2012, A&A, 545, A117
- Lister, M. L., et al. 2013, AJ, 146, 120
- Longair, M. S. 2011, High Energy Astrophysics
- Lynden-Bell, D. 1969, Nature, 223, 690
- Ma, L., Xie, G. Z., Yi, T. F., Zhou, S. B., Li, K. H., Zhang, X., & Dai, H. 2010, Ap&SS, 327, 35
- Madejski, G. M., et al. 2016, ApJ, 831, 142
- MAGIC Collaboration, et al. 2016, ArXiv e-prints
- Man, Z., Zhang, X., Wu, J., Zhou, X., & Yuan, Q. 2014, AJ, 148, 110
- Mangalam, A. V., & Wiita, P. J. 1993, ApJ, 406, 420
- Marcha, M. J. M., Browne, I. W. A., Impey, C. D., & Smith, P. S. 1996, MNRAS, 281, 425
- Marscher, A. 2016, Galaxies, 4, 37

- Marscher, A. P. 1996, in Astronomical Society of the Pacific Conference Series, Vol. 110, Blazar Continuum Variability, ed. H. R. Miller, J. R. Webb, & J. C. Noble, 248
- Marscher, A. P. 2014, *ApJ*, 780, 87
- Marscher, A. P., & Gear, W. K. 1985, *ApJ*, 298, 114
- Massaro, E., Nesci, R., Maesano, M., Montagni, F., & D'Alessio, F. 1998, *MNRAS*, 299, 47
- Massaro, E., Perri, M., Giommi, P., & Nesci, R. 2004, *A&A*, 413, 489
- Massaro, F., Tramacere, A., Cavaliere, A., Perri, M., & Giommi, P. 2008, *A&A*, 478, 395
- Mastichiadis, A., & Kirk, J. G. 2002, *PASA*, 19, 138
- McHardy, I. M., Luppino, G. A., George, I. M., Abraham, R. G., & Cooke, B. A. 1992, *MNRAS*, 256, 655
- Miller, H. R., Carini, M. T., Gaston, B. J., & Hutter, D. J. 1988, in *ESA Special Publication*, Vol. 281, *ESA Special Publication*
- Miller, H. R., Carini, M. T., & Goodrich, B. D. 1989, *Nature*, 337, 627
- Miller, H. R., Ferrara, E. C., Daya, A. B., Wilson, J. W., Fried, R. E., Noble, J. C., & Jang, M. 1999, in *Blazar Monitoring towards the Third Millennium*, ed. C. M. Raiteri, M. Villata, & L. O. Takalo, 20
- Miller, H. R., & Green, R. F. 1983, in *BAAS*, Vol. 15, *Bulletin of the American Astronomical Society*, 957
- Mücke, A., & Protheroe, R. J. 2001, *Astroparticle Physics*, 15, 121
- Mücke, A., Protheroe, R. J., Engel, R., Rachen, J. P., & Stanev, T. 2003, *Astroparticle Physics*, 18, 593
- Neronov, A., Semikoz, D., & Taylor, A. M. 2012, *A&A*, 541, A31
- Oda, M., Gorenstein, P., Gursky, H., Kellogg, E., Schreier, E., Tananbaum, H., & Giacconi, R. 1971, *ApJ*, 166, L1
- Osterman, M. A., et al. 2006, *AJ*, 132, 873
- Padovani, P. 2016, *A&A Rev.*, 24, 13

REFERENCES

- Padovani, P., & Giommi, P. 1995, MNRAS, 277, 1477
- Paliya, V. S., Böttcher, M., Diltz, C., Stalin, C. S., Sahayanathan, S., & Ravikumar, C. D. 2015, ApJ, 811, 143
- Pandey, A., Gupta, A. C., & Wiita, P. J. 2017, ApJ, 841, 123
- Pandey, A., Gupta, A. C., & Wiita, P. J. 2018, ApJ, 859, 49
- Pandey, A., Gupta, A. C., Wiita, P. J., & Tiwari, S. N. 2019, ApJ, 871, 192
- Perlman, E. S., et al. 1996, ApJS, 104, 251
- Peterson, B. M. 1997, An Introduction to Active Galactic Nuclei
- Pian, E., et al. 1998, ApJ, 492, L17
- Piner, B. G., & Edwards, P. G. 2004, ApJ, 600, 115
- Pittori, C., et al. 2008, The Astronomer's Telegram, 1583
- Polednikova, J., et al. 2016, MNRAS, 460, 3950
- Pollack, M., Pauls, D., & Wiita, P. J. 2016, ApJ, 820, 12
- Poon, H., Fan, J. H., & Fu, J. N. 2009, ApJS, 185, 511
- Punch, M., et al. 1992, Nature, 358, 477
- Quinn, J., et al. 1996, ApJ, 456, L83
- Racero, E., & de la Calle, I. 2013, in European Physical Journal Web of Conferences, Vol. 61, European Physical Journal Web of Conferences, 04020
- Raiteri, C. M., et al. 2017, Nature, 552, 374
- Raiteri, C. M., Villata, M., de Francesco, G., Lanteri, L., Cavallone, M., & Sobrito, G. 1998, A&AS, 132, 361
- Raiteri, C. M., et al. 2003, A&A, 402, 151
- Rakshit, S., Stalin, C. S., Chand, H., & Zhang, X.-G. 2017, ApJS, 229, 39
- Ravasio, M., Tagliaferri, G., Ghisellini, G., & Tavecchio, F. 2004, A&A, 424, 841
- Rector, T. A., Gabuzda, D. C., & Stocke, J. T. 2003, AJ, 125, 1060
- Rees, M. J. 1984, ARA&A, 22, 471

REFERENCES

- Remillard, R. A., Tuohy, I. R., Brissenden, R. J. V., Buckley, D. A. H., Schwartz, D. A., Feigelson, E. D., & Tapia, S. 1989, *ApJ*, 345, 140
- Romero, G. E. 1995, *Ap&SS*, 234, 49
- Romero, G. E., Cellone, S. A., & Combi, J. A. 1999, *A&AS*, 135, 477
- Rybicki, G. B., & Lightman, A. P. 1986, *Radiative Processes in Astrophysics* 400
- Salpeter, E. E. 1964, *ApJ*, 140, 796
- Sambruna, R. M., Maraschi, L., & Urry, C. M. 1996, *ApJ*, 463, 444
- Samuelson, F. W., et al. 1998, *ApJ*, 501, L17
- Sandrinelli, A., Covino, S., Dotti, M., & Treves, A. 2016, *AJ*, 151, 54
- Sato, R., Kataoka, J., Takahashi, T., Madejski, G. M., Rügamer, S., & Wagner, S. J. 2008, *ApJ*, 680, L9
- Schachter, J. F., et al. 1993, *ApJ*, 412, 541
- Schmidt, M. 1963, *Nature*, 197, 1040
- Seyfert, C. K. 1943, *ApJ*, 97, 28
- Sinha, A., Shukla, A., Misra, R., Chitnis, V. R., Rao, A. R., & Acharya, B. S. 2015, *A&A*, 580, A100
- Sinha, A., et al. 2016, *A&A*, 591, A83
- Smith, A. J., et al. 2008, International Cosmic Ray Conference, 3, 973
- Stalin, C. S., Gupta, A. C., Gopal-Krishna, Wiita, P. J., & Sagar, R. 2005, *MNRAS*, 356, 607
- Stetson, P. B. 1987, *PASP*, 99, 191
- Stetson, P. B. 1992, in *Astronomical Society of the Pacific Conference Series*, Vol. 25, *Astronomical Data Analysis Software and Systems I*, ed. D. M. Worrall, C. Biemesderfer, & J. Barnes, 297
- Stocke, J. T., Morris, S. L., Gioia, I. M., Maccacaro, T., Schild, R., Wolter, A., Fleming, T. A., & Henry, J. P. 1991, *ApJS*, 76, 813
- Tagliaferri, G., Ravasio, M., Ghisellini, G., Tavecchio, F., Giommi, P., Massaro, E., Nesci, R., & Tosti, G. 2003, *A&A*, 412, 711

REFERENCES

- Takahashi, T., et al. 1995, IAU Circ., 6167
- Takahashi, T., et al. 1994, IAU Circ., 5993
- Teräsranta, H., et al. 2004, A&A, 427, 769
- Teräsranta, H., Wiren, S., Koivisto, P., Saarinen, V., & Hovatta, T. 2005, A&A, 440, 409
- Tramacere, A., et al. 2007, A&A, 467, 501
- Tramacere, A., Giommi, P., Perri, M., Verrecchia, F., & Tosti, G. 2009, A&A, 501, 879
- Tramacere, A., Massaro, F., & Cavalieri, A. 2007, A&A, 466, 521
- Ulmer, M. P., Brown, R. L., Schwartz, D. A., Patterson, J., & Cruddace, R. G. 1983, ApJ, 270, L1
- Ulmer, M. P., et al. 1980, ApJ, 235, 351
- Urry, C. M. 1998, Advances in Space Research, 21, 89
- Urry, C. M., et al. 1993, ApJ, 411, 614
- Urry, C. M., & Padovani, P. 1995, PASP, 107, 803
- Ushio, M., et al. 2009, ApJ, 699, 1964
- Valtonen, M., & Pihajoki, P. 2013, A&A, 557, A28
- Vaughan, S., Edelson, R., Warwick, R. S., & Uttley, P. 2003, MNRAS, 345, 1271
- Véron-Cetty, M.-P., & Véron, P. 2003, A&A, 412, 399
- Villata, M., & Raiteri, C. M. 1999, A&A, 347, 30
- Villata, M., et al. 2004, A&A, 421, 103
- Wagner, S. J., & Witzel, A. 1995, ARA&A, 33, 163
- Wierzcholska, A., Ostrowski, M., Stawarz, Ł., Wagner, S., & Hauser, M. 2015, A&A, 573, A69
- Wierzcholska, A., & Wagner, S. J. 2016, MNRAS, 458, 56
- Woo, J.-H., Urry, C. M., van der Marel, R. P., Lira, P., & Maza, J. 2005, ApJ, 631, 762

REFERENCES

- Wood, K. S., et al. 1984, ApJS, 56, 507
- Wu, J., Böttcher, M., Zhou, X., He, X., Ma, J., & Jiang, Z. 2012, AJ, 143, 108
- Wu, J., Zhou, X., Ma, J., & Jiang, Z. 2011, MNRAS, 418, 1640
- Xie, G. Z., Zhou, S. B., Dai, B. Z., Liang, E. W., Li, K. H., Bai, J. M., Xing, S. Y., & Liu, W. W. 2002, MNRAS, 329, 689
- Zhang, B.-K., Zhao, X.-Y., Wang, C.-X., & Dai, B.-Z. 2014, Research in Astronomy and Astrophysics, 14, 933
- Zhang, Y. H. 2008, ApJ, 682, 789
- Zhang, Y. H., et al. 2002, ApJ, 572, 762
- Zhou, H., Wang, T., Yuan, W., Lu, H., Dong, X., Wang, J., & Lu, Y. 2006, ApJS, 166, 128

Appendix: Finding Charts and Comparison Stars

The finding charts and the list of comparison stars for the observed TeV blazars are given below. The source is shown in between two lines and the comparison stars are marked by letters or/and numbers. The finding charts and the standard magnitudes of comparison stars for 1ES 0229+200, 1ES 0414+009, 1ES 0806+524, and 1ES 2344+514 are taken from <https://www.lsw.uni-heidelberg.de/projects/extragalactic/charts/>, while those for 1ES 1553+113 are adapted from Raiteri, C. M. et al. 2015, MNRAS 454, 353–367.

A.1 1ES 0229+200

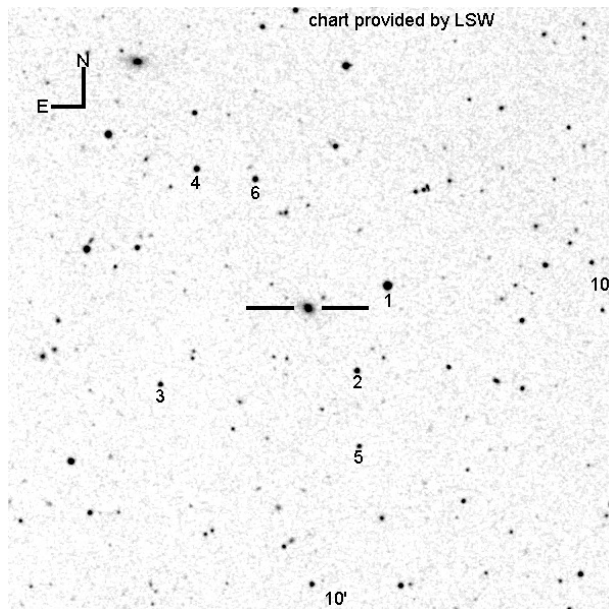


Figure 1: Finding chart for the TeV blazar 1ES 0229+200.

A. APPENDIX: FINDING CHARTS AND COMPARISON STARS

Table 1: List of comparison stars for 1ES 0229+200 and their standard magnitudes in B and R filters.

Star	B	R
1	14.7	13.7
2	16.9	16.3
3	17.4	16.6
4	16.7	15.7
5	19.4	17.4
6	17.7	16.0

A.2 1ES 0414+009

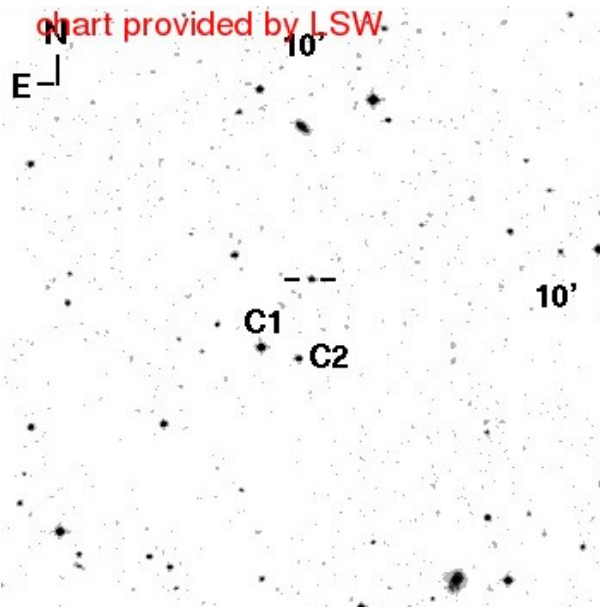


Figure 2: Finding chart for the TeV blazar 1ES 0414+009.

Table 2: List of comparison stars for 1ES 0414+009 and their standard magnitudes in V , R , and I filters.

Star	V	R	I
C1	13.95 (0.05)	13.56 (0.05)	13.15 (0.05)
C2	15.17 (0.07)	14.63 (0.07)	14.06 (0.07)

A.3 1ES 0806+524

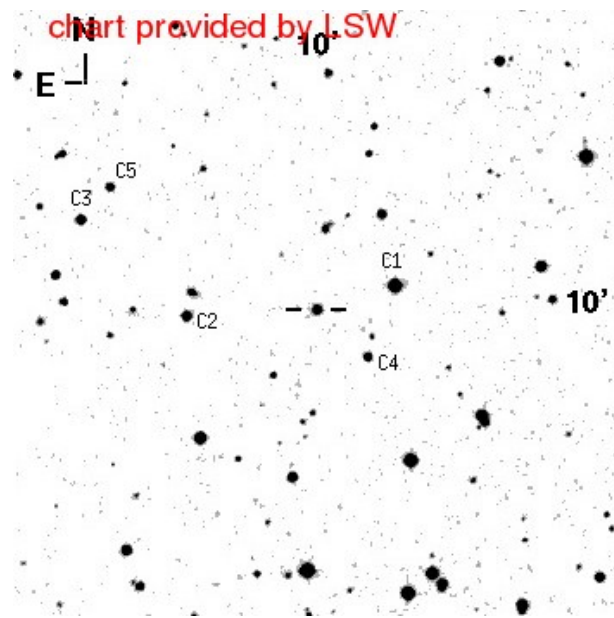


Figure 3: Finding chart for the TeV blazar 1ES 0806+524.

Table 3: List of comparison stars for 1ES 0806+524 and their standard magnitudes in V , R , and I filters.

Star	V	R	I
C1	13.04 (0.05)	12.56 (0.05)	12.14 (0.05)
C2	14.61 (0.05)	14.22 (0.04)	13.86 (0.04)
C3	14.77 (0.05)	14.39 (0.05)	14.04 (0.05)
C4	15.49 (0.06)	15.14 (0.06)	14.81 (0.06)
C5	15.62 (0.06)	15.32 (0.05)	14.99 (0.06)

A. APPENDIX: FINDING CHARTS AND COMPARISON STARS

A.4 1ES 1553+113

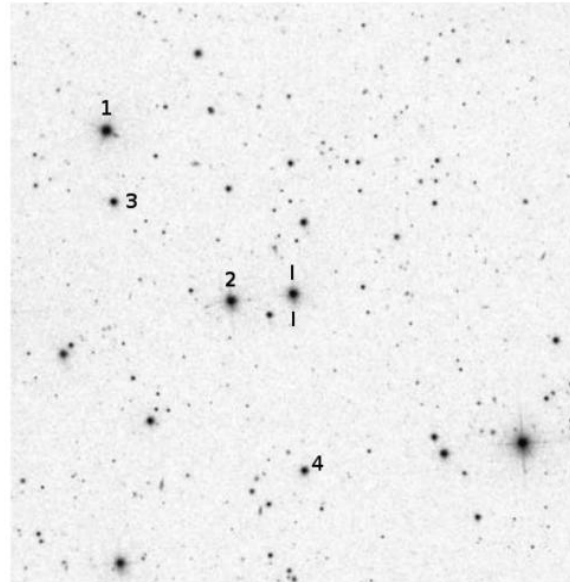


Figure 4: Finding chart for the TeV blazar 1ES 1553+113.

Table 4: List of comparison stars for 1ES 1553+113 and their standard magnitudes in V , R , and I filters.

Star	V	R	I
1	13.832 (0.027)	13.465 (0.032)	13.080 (0.056)
2	13.923 (0.022)	13.582 (0.029)	13.230 (0.055)
3	15.688 (0.017)	15.277 (0.026)	14.896 (0.051)
4	15.771 (0.019)	15.317 (0.029)	14.893 (0.056)

A.5 1ES 2344+514

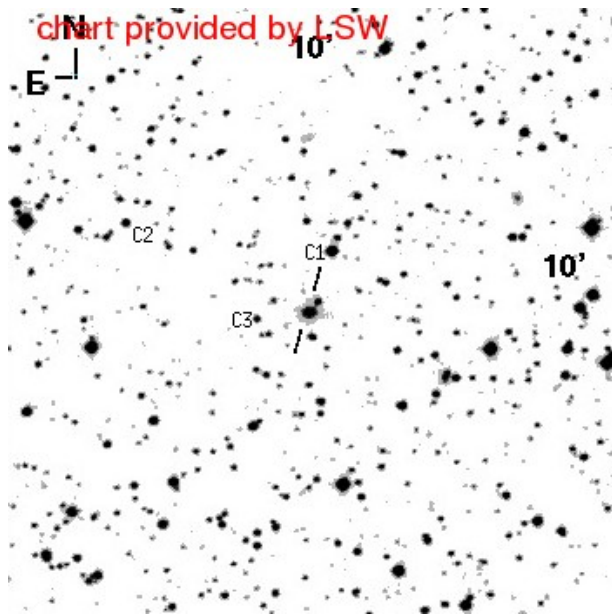


Figure 5: Finding chart for the TeV blazar 1ES 2344+514.

Table 5: List of comparison stars for 1ES 2344+514 and their standard magnitudes in V , R , and I filters.

Star	V	R	I
C1	12.61 (0.04)	12.25 (0.04)	11.90 (0.04)
C2	14.62 (0.06)	14.20 (0.05)	13.84 (0.04)
C3	15.89 (0.08)	15.40 (0.08)	14.89 (0.08)